THE UNIVERSITY OF CHICAGO

ELECTROSTATIC STABILIZATION AND SELF ASSEMBLY OF CHARGED COLLOIDAL NANOCRYSTALS

A DISSERTATION SUBMITTED TO
THE FACULTY OF THE DIVISION OF THE PHYSICAL SCIENCES
IN CANDIDACY FOR THE DEGREE OF
DOCTOR OF PHILOSOPHY

DEPARTMENT OF CHEMISTRY

BY

JOSHUA CHARLES PORTNER

CHICAGO, ILLINOIS

JUNE 2023

Table of Contents

List of Tables iv

List of Figures v

Acknowledgements viii

Abstract xi

1. Introduction 1

1.1. Colloidal synthesis and quantum confinement of semiconductor nanocrystals 1

1.2. Applications of semiconductor nanocrystals and the role of all-inorganic surface chemistry 2

1.3. Small angle X-ray scattering as a tool for nanocrystal size analysis and probe for colloidal stability 4

1.4. Self-assembly of nanocrystals into structures with long-range order and strong coupling 6

1.5. Chapter 1 bibliography 8

2. Synthesis and electrostatic stabilization of charged colloidal nanocrystals 11

2.1. Introduction 11

2.2. PbS nanocrystal synthesis and characterization 12

2.3. Surface chemistry characterization of MCC capped semiconductor nanocrystals 18

2.4. Structure factors of MCC capped nanocrystal solutions 24

2.5. Quantification of interparticle interactions through the second virial coefficient 31

2.6. Determination of charged PbS nanocrystal second virial coefficients by quantitative small angle X-ray scattering 33

2.7. Chapter 2 bibliography 42

3. Self-assembly of nanocrystals into strongly electronically coupled all-inorganic supercrystals 46

3.1. Introduction 46

3.2. Synthesis and reversible self-assembly of all-inorganic supercrystals from charged colloidal nanocrystals 48

3.3. Crystal structures of all-inorganic supercrystals 53

3.4. Charge accumulation around highly polarizable nanocrystals 59

3.5. Short-range interparticle attraction leads to triple-phase coexistence of colloidal NC gas, liquid, and solid phases 62

3.6. Kinetics of supercrystal nucleation 68

3.7. Crystallographic alignment across all-inorganic PbS supercrystals 75

3.8. Gallery of TEM images showcasing additional self-assembly of semiconductor nanocrystals 80

3.9. Experimental Methods 84

3.10. Chapter 3 bibliography 93

List of Tables

Table 2-1: Second virial coefficient results for PbS-Sn_2S_6 NCs in NMF by Zimm analysis. 38

Table 2-2: Second virial coefficient results for PbS-Sn_2S_6 NCs in NMF by low-q structure factor analysis of SAXS data. 41

Table 3-1: Unit cell parameters and d spacings measured from an fcc supercrystal assembled from 5.7 nm PbS NCs and PbS NC atomic lattices. 78

List of Figures

Figure 1-1: Quantum confinement of CdSe nanocrystals. 2

Figure 1-2: Nanocrystal surface ligand diversity. 3

Figure 1-3 Size analysis of SAXS for spherical particles. 5

Figure 1-4 Nanocrystal self-assembly overview. 7

Figure 2-1: Overview of PbS nanocrystal synthesis. 13

Figure 2-2: Comparison of PbS NCs synthesis using $(TMS)_2S$ vs thiourea precursors. 13

Figure 2-3: PbS synthesis temperature and solvent dependence. 14

Figure 2-4: Comparison of hot-injection and heat-up PbS NC synthesis. 15

Figure 2-5: Air stability of PbS NCs. 16

Figure 2-6: PbS nanocrystal size determination. 17

Figure 2-7: Nanocrystal ligand exchange into polar solvents. 19

Figure 2-8: Ligand dependent size broadening of PbS NCs by SAXS. 20

Figure 2-9: MCC ligand exchange of CdSe NCs into polar solvents. 21

Figure 2-10: Elemental analysis of nanocrystal MCC ligand grafting density. 22

Figure 2-11: Chemical identification of thiostannate in polar solvents. 23

Figure 2-12: Structure factor of charged PbS NC colloids. 25

Figure 2-13: Concentration dependence of MCC capped PbS structure factor. 26

Figure 2-14: Ionic strength dependent structure factor. 28

Figure 2-15: Solvent dependent PbS structure factor. 29

Figure 2-16: Solution structure factors from formamide family solvents. 30

Figure 2-17: Colloidal instability of PbS NCs in non-formamide solvents. 31

Figure 2-18: Nanocrystal molecular weight calculation. 35

Figure 2-19: Zimm analysis of PbS NC second virial coefficients. 37

Figure 2-20: Second virial coefficient results for PbS-Sn_2S_6 in NMF by low-q structure factor analysis. 39

Figure 3-1: Comparison of long-range order and strong coupling across nanocrystal assemblies. 48

Figure 3-2: Schematic of electrostatic self-assembly. 50

Figure 3-3: Compositional diversity of all-inorganic NC assemblies. 51

Figure 3-4: Flocculating salt valency controls NC long-range order. 52

Figure 3-5: Reversibility in NC self-assembly. 53

Figure 3-6: PbS and Au fcc supercrystal comparison. 54

Figure 3-7: Lattice contraction of PbS NC supercrystals. 55

Figure 3-8: Complex structure factors in Au NC supercrystals. 58

Figure 3-9: Supercrystal fcc/hcp phase coexistence. 59

Figure 3-10: NC material composition dependent self-assembly. 60

Figure 3-11: Charge accumulation at high dielectric NC surfaces. 61

Figure 3-12: Semiconductor NC charge density of elemental analysis. 62

Figure 3-13: Modeling interactions and phase equilibria of charge-stabilized colloidal nanocrystals. 63

Figure 3-14: Triple-phase coexistence and nucleation in charge-stabilized NC colloids. 65

Figure 3-15: NC dense liquid phase structure factor. 66

Figure 3-16: Visual inspection of Au supercrystal flocculation. 67

Figure 3-17: Phase separation of PbS NCs and triple-phase coexistence. 68

Figure 3-18: Phase diagram for PbS NCs in NMF/DMF. 69

Figure 3-19: One-step in situ nucleation kinetics. 71

Figure 3-20: Two-step in situ nucleation at constant screening length. 73

Figure 3-21: Two-step in situ nucleation at constant $\boldsymbol{\phi NC}$. 74

Figure 3-22: In situ monitoring of one step Au SC nucleation. 75

Figure 3-23: Atomic coherence in PbS supercrystals. 77

Figure 3-24: Unit cell reconstruction of atomically aligned PbS NCs 79

Figure 3-25: PbS NC orientations in atomically aligned supercrystals. 80

Figure 3-26: Rapid flocculation and assembly of PbS NCs. 81

Figure 3-27: Slow flocculation and assembly of PbS NCs. 82

Figure 3-28: Self-assembly of MCC capped PbSe NCs. 83

Figure 3-29: Flocculation of CdSe NCs from polar solvents. 84

Figure 3-30: Representative NC populations. 86

Acknowledgements

My journey through graduate school was by no means a solo one, and I have many people to thank for their support during my graduate work. I would like to start by thanking my research advisor, Prof. Dmitri Talapin, for his constant guidance and support throughout my PhD journey. I was able to learn and grow as both a scientist and person throughout the time spent in his lab, and I am grateful for his constant positivity and enthusiasm towards our research directions. I also want to thank my committee members Prof. John Anderson and Prof. Bozhi Tian for their support and guidance at various points throughout my graduate career.

Much of my work was the result of collaborations with scientists across the country, and I am thankful for all of their contributions to the research and to the many great personal relationships. Thank you to Prof. Naomi Ginsberg, James, Christian, and Vivian for your tireless support at beamtimes and for being wonderful collaborators to work with. Thank you to Prof. David Limmer and Avishek for helping to steer the ship trying to understand the theories and literature of self-assembly. I have had the pleasure of working with multiple beamline scientists that have supported my work with X-ray analysis and would like to thank Andrei Fluerasu, Chris Tassone, Xiaobing Zuo, and many other beamline scientists that have dedicated time to make beamtimes run smoothly.

At the University of Chicago, I am blessed to be surround by great facilities and managers that help them run smoothly. I would like to thank Dr. Alex Filatov for his help with X-ray analysis and always keeping the SAXS in good care, Dr. Justin Jureller for his help in training and maintenance of multiple MRSEC instruments, and Yimei Chen for her help with TEM experiments.

My coworkers in the Talapin lab have made my graduate experience all the better, and I had the pleasure to mentor one of the best undergraduate students a grad student could ask for, Alex Hinkle. Thank you for commitment to do excellent science and your great friendship. Thank you to Dr. Maggie Hudson, Dr. Eric Janke, Dr. Vishwas Srivastava, Dr. Jia-Ahn Pan, Dr. Justin Ondry, Dr. Igor Corpceanu, Aritrajit Gupta, Nivedina Sarma, and Ahhyun Jeong for your friendship and support, having people like you around made grad school all the more enjoyable. I would also like to thank Dr. Igor Fedin, Dr. Abhijit Hazarika, Dr. Patrick Cunningham, Dr. Yuanyuan Wang, and Dr. Vlad Kamysbayev for their advice and support throughout my graduate research. Thank you to everyone in the Talapin lab for your helpful conversations and assistance in the lab: Dr. Himchan Cho, Dr. Iryna Golovina, Dr. Xinzheng Lan, Dr. Matt Kurley, Dr. Chenkun Zhou, Dr. Jun Hyuk Chang, Dr. James Cassidy, Wooje Cho, Haoqi Wu, Di Wang, Zirui Zhou, Ruiming Lin, and Zehan Mi. I would also like to thank Tanya Shpigel and Dr. Andrew Nelson for their support throughout my time in the lab to make all of our lives easier.

I am also grateful for the support throughout my teaching opportunities at UChicago, I am grateful for the experience I was able to gain that only a tight-knit lab environment a senior level lab class can provide. Thank you to Prof. Jiwoong Park for supporting me throughout my time at UChicago, and to Dr. Zbigniew Gasyna for your assistance in managing the many complexities of the lab course. I would also like to thank the Chemistry departmental staff, Dr. Vera Dragisich and Melinda Moore, who always made my work and life easier.

Finally, to my friends and family, I am incredibly grateful for your love and support, I am confident that graduate school would not have been possible without your willingness to accept my many phone calls and provide encouragement. I am grateful to my parents, Dean and Jenny, my brothers, Justin and Jacob, and to my numerous extended family who I am fortunate to see

more than most are able to, for all of their support through the highs and lows of graduate school. To my friends, Eric, Caroline, Morgan, Beth, Hannah, Michelle, Fauzia, Kim, Baorui, Aritrajit, Tim, Maggie, Hannah, and to all the members of the world-renowned Baseliners softball team, I extend my deepest thanks for your support and friendship. I have had so much fun exploring Chicago and more of the world together with you and am thankful for all of the memories we have shared together.

Abstract

Semiconductor nanocrystals (NCs) serve as useful building block materials made attractive by their solution processibility and size dependent optical properties. In this thesis, I begin by introducing the fundamental properties and applications of semiconductor NCs and the use of X-ray scatting to probe NC solution properties. Chapter 2 focuses on the synthesis of high quality PbS NCs and their ligand exchange into polar solvents with multivalent metal chalcogenide complex (MCC) ligands. I explore the chemical analysis of the NC surface chemistry and how it impacts the colloidal stability of NCs in N-methylformamide solvents. Small angle X-ray scattering analysis is used to probe the concentration dependent solution structure factors and quantify the repulsive interaction potentials which are largest for intermediate (~6 nm) PbS NCs. In the second half of the thesis, Chapter 3 focuses on the transition of these electrostatically stabilized NCs from the solution to solid phase. Long-range order emerges as NCs flocculate and self-assemble into densely packed 3D supercrystals with interparticle spacings less than 0.5 nm. Supercrystals predominantly nucleate into face centered cubic (fcc) structures and can be dissolved in fresh solvent to recover the initial colloidal NCs without any change to the NC size or shape. I find that the supercrystal nucleation proceeds through both one-step and two-step mechanisms where supercrystals nucleate from a dense fluid phase in the latter case. The position of the NC solution within a phase diagram and the proximity to the binodal line separating dilute and dense fluid phases dictate the crystalline yield and kinetics of supercrystal nucleation. I also find that faceted PbS NCs assemble with atomic coherence between their atomic crystal structures across micron sized supercrystals, a feature dictated by the high surface charge density on the faceted NC surfaces.

1. Introduction

1.1. Colloidal synthesis and quantum confinement of semiconductor nanocrystals

Colloidal nanocrystals (NCs) synthesized from the organic solutions offer a promising route to functional metallic, semiconducting, insulating, and magnetic materials with tunable size, shape, and surface chemistry. A typical synthesis of semiconducting metal chalcogenide NCs is performed by rapid injection of a chalcogenide precursor solution into a hot flask containing target metal ions stabilized by surfactant molecules in a nonpolar solvent.[1] Reaction temperatures are chosen to tune the precursor reactivity and allow the crystallization of a given NC material. Surfactant molecules coordinate to NC surfaces with terminal functional groups (e.g., carboxylic acids, amines) and have long-chain organic backbones facing the surrounding solution.

Semiconductor NCs with sizes smaller than the Bohr exciton radius for a given material show quantum confinement effects of electron hole pairs (excitons) and a quantization of electronic states near the conduction and valence band edges. The energy of the first excitonic transition (E) is described by:

$$E = E_g + \frac{\hbar^2 \pi^2}{2R^2}\left(\frac{1}{m_e} + \frac{1}{m_h}\right) - \frac{1.8e^2}{\epsilon R}$$

which is calculated for a NC of known radius (R), bulk material bandgap (E_g), permittivity (ϵ), and effective mass of electron (m_e) and hole (m_h).[2] Spherical NCs that undergo quantum confinement effects are called quantum dots, and their band gap gas a strong size dependence for sizes less than the bulk Bohr exciton radius (Figure 1-1). CdSe has a bulk Bohr radius of 5.4 nm, and NCs with 3 to 5 nanometer diameters show size dependent absorption features across the visible spectrum with increasing confinement for smaller NC sizes (Figure 1-1B).

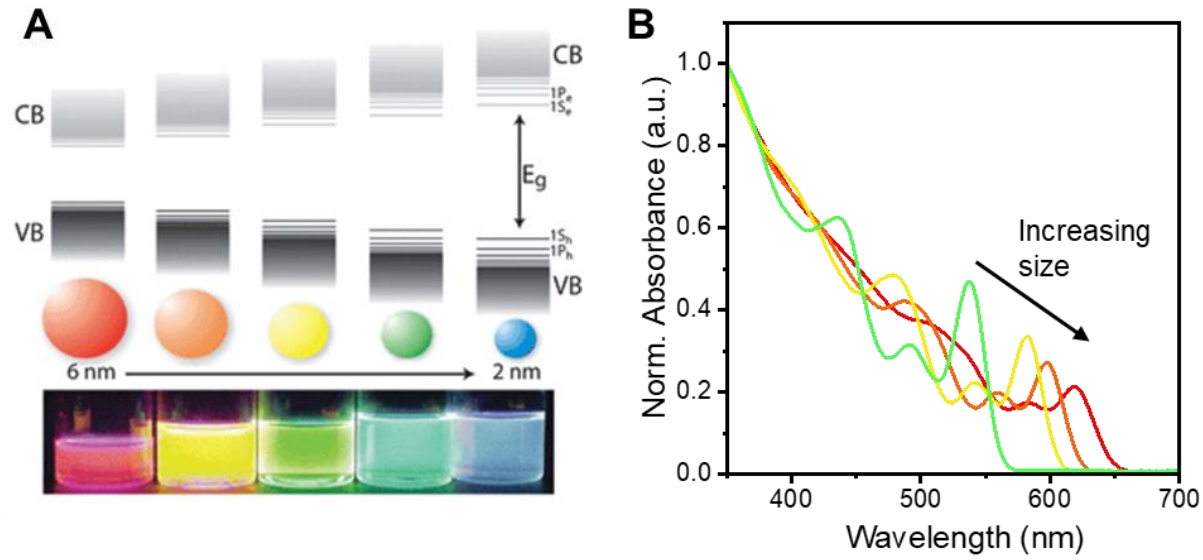

Figure 1-1: Quantum confinement of CdSe nanocrystals.

(**A**) Schematic of CdSe size dependent band gaps and discrete energy states near the band edges and corresponding images of size dependent NC photoluminescence (bottom). Reproduced with permission from Donegá et al., copyright Royal Society of Chemistry.[3] (**B**) Absorbance spectra for a series of CdSe NC sizes in non-polar solvents, normalized to bulk CdSe absorbance at 350 nm. Data show reduced quantum confinement and oscillator strength of the exciton absorbance for larger NC sizes.

1.2. Applications of semiconductor nanocrystals and the role of all-inorganic surface chemistry

Colloidal NCs show great promise as nanoscale building block materials with many material properties controlled directly from the solution-based synthesis. Solution processable NC inks enable inexpensive and scalable thin film deposition techniques including spin coating, spray coating, and inkjet printing without the need for high temperature or vacuum conditions.[4] Much attention has been placed on the optoelectronic applications of NCs as bright emitters in display technologies[5] and as active materials in photovoltaics,[6] photodetectors,[7] and transistors.[8]

Native organic ligands on NC surfaces prevent conduction pathways in thin films due to their insulating behavior, but a large library of inorganic surface ligands has been developed which

increase the NC film conductivity by up to eleven orders of magnitude (Figure 1-2).[9] The increase in coupling strength between nanocrystals with inorganic ligands is due to the decreased interparticle distance and enables functional devices such as transistors constructed entirely from semiconducting, insulating, and metallic NCs with inorganic surface ligands.[11] Strong coupling has also led to the observation of band-like transport in NC solids with electronic conductivity proceeding through discrete QD electronic states.[12–14] NCs capped with inorganic ligands maintain solution processibility and dissolve into polar solvents stabilized by repulsive electrostatic interactions. In this thesis, I focus much attention to the surface chemistry of NCs with metal chalcogenide complex (MCC) ligands and their stabilization of PbS, CdSe, and Au NCs. MCC ligands are multivalent in nature and can provide more stability in the form of surface charge density than other classes of ligands such as monovalent halides or pseudo halides.

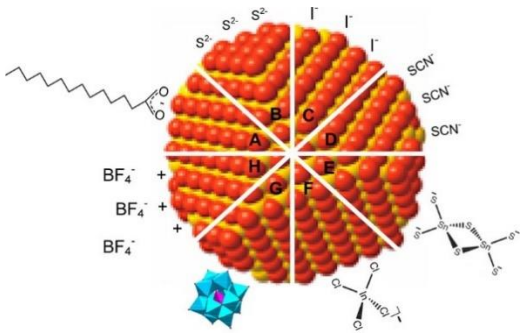

Figure 1-2: Nanocrystal surface ligand diversity.

Schematic of a NC surface stabilized by (**A**) organic ligands, (**B**) chalcogenide ions, (**C**), halide ions, (**D**) pseudohalide ions, (**E**) metal chalcogenide complex (MCC) ligands, (**F**) halometallate ions, (**G**) polyoxometalate ions, and (**H**) bare surfaces with non-bonding counterions. Reproduced with permission from Kovalenko et al., copyright American Chemical Society.[10]

1.3. Small angle X-ray scattering as a tool for nanocrystal size analysis and probe for colloidal stability.

The size of semiconductor NCs determines the optical properties of the material and impacts the total interparticle interactions in colloidal solutions. Measuring the true NC size is an important endeavor in the characterization of these materials for an accurate picture of the system at the nanoscale. Direct measurement of NC sizes by electron microscopy requires the individual sizing of many NCs to construct an accurate histogram and can suffer from population under sampling and human bias. Image processing algorithms can solve a few of these challenges but can still suffer from inconsistent determination of the NC edges at varying focal planes. For relatively spherical NCs, small angle X-ray scattering (SAXS) offers a useful sizing alternative with high repeatability and precision as the entire NC population within the beam volume is sampled.

SAXS intensity of colloidal NCs can be broken down into contributions from the solution structure factor, $S(q)$, and form factor, $P(q)$:

$$I(q) = S(q)P(q)$$

The structure factor and form factor consist of contributions from interparticle and intraparticle scattering, respectively. Ideal colloidal solutions have $S(q)$~1, and the remaining form factor intensity is dependent on the NC radius, R, and size distribution, $n(R)$:

$$P(q) = \int n(R) \langle |F(q,R)|^2 \rangle \, dR$$

where $F(q)$ is the form factor for spheres of uniform density:

$$F(q) = A \frac{3(\sin(qR) - qR\cos(qR))}{(qR)^3}$$

Here, the coefficient A can be quantitively determined by measurements of the scattering length density (ρ) contrast between the NC and solvent.[15] When only the relative form factor is needed for NC sizing, A is left as a free fitting parameter. The NC size distribution, $n(R)$, can be modeled by multiple functional forms, but a normalized gaussian distribution is convenient in most cases:

$$n(R) = \frac{1}{\sigma\sqrt{2\pi}} e^{\frac{-(R-R_{NC})^2}{2\sigma^2}}$$

An example of size analysis for PbS NCs in non-polar methylcyclohexane is shown in Figure 1-3 which results in an average NC diameter of 7.2 nm and standard deviation of 0.38 nm after fitting to the experimental SAXS data. To ensure good size fitting, NC samples require good colloidal stability with a minimal structure factor to cleanly model the form factor.

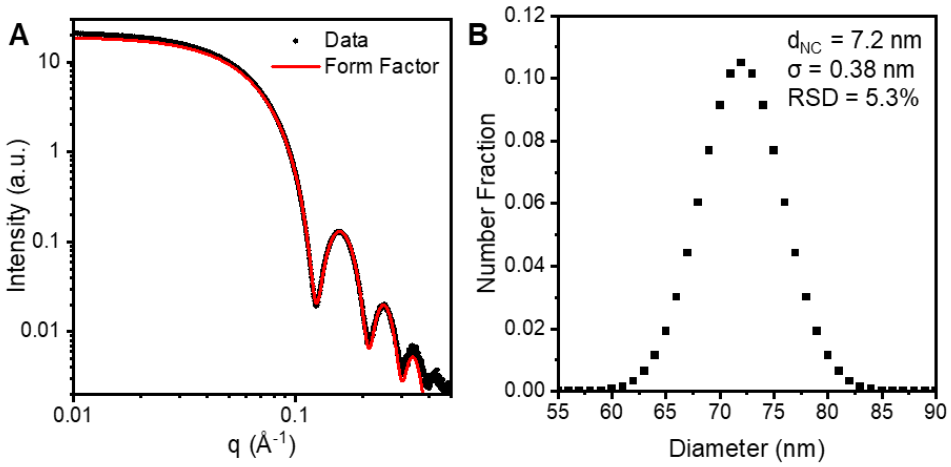

Figure 1-3 Size analysis of SAXS for spherical particles.

(**A**) Representative SAXS data of 7.2 nm PbS-OA in methylcyclohexane. Calculated form factor, $P(q)$, is in good agreement with experimental SAXS data. (**B**) Normalized gaussian number distribution of NCs, $n(R)$, used to calculate the NC form factor.

The colloidal stability of NCs can be readily probed by SAXS analysis, especially by determination of the solution structure factor:

$$S(q) = \frac{I(q)}{P(q)}$$

The structure factor scaling as $S(q) \to 0$ is a visual tool that qualitatively predicts the NC colloidal stability. In Chapter 2, I discuss the NC structure factors in more detail and qualitatively use them to determine the colloidal stability of PbS NCs with both organic ligands and inorganic MCC ligands. I also use colloidal structure factor analysis to quantitively measure the NC second virial coefficient, B_2, which describes the net attractive or repulsive interparticle interactions.

1.4. Self-assembly of nanocrystals into structures with long-range order and strong coupling

Colloidal NCs are synthesized and processed in solution form, but the transformation from liquid to solid is a key step in the application of NCs as functional materials in thin films. As NCs with long organic ligands are confined into small volumes and form solids, they behave similar to hard spheres where the lowest energy state is a crystalline structure to minimize the free energy of the system. In this configuration, the local energy is maximized with more translational and rotational freedom per particle than a corresponding disordered, jammed state at identical volume fractions.[16] In practice, spherical NCs with organic ligands and narrow size distributions readily form densely packed superlattices upon solvent drying (Figure 1-4), and more complex assemblies are also accessible by self-assembly of 2D nanoplatelet or binary structures from two sizes of spherical NCs which follow the same principle of free energy minimization. In cases where the liquid to solid transition is too rapid (e.g., fast solvent evaporation), NCs can become kinetically trapped without the ability to access the lowest energy configuration of fcc crystals for uniform spheres.

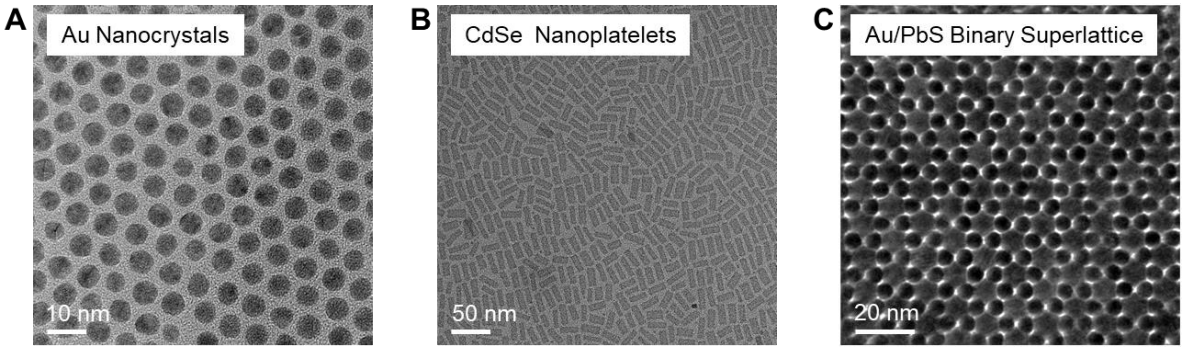

Figure 1-4 Nanocrystal self-assembly overview.

TEM images depict self-assembly of three nanocrystals systems. (**A**) Au NCs with dodecanethiol ligands. (**B**) 2D CdSe nanoplatelets with oleic acid ligands assembled in a face-down alignment. (**C**) Binary superlattice with an AB_2 binary structure composed of 4.8 nm Au NCs with dodecanethiol ligands and 8.9 nm PbS NCs with oleic acid ligands.

Spherical NCs with organic ligands can form long-range ordered structures but lack the strong coupling often desired in NC device applications. On-film ligand exchanges can be used to increase the coupling strength after initial assembly, but the native organic ligands can only partially be removed lattice contraction cannot uniformly affect films without leaving voids.[17] In Chapter 3, I describe a novel approach to synthesize strongly coupled NC assemblies from bottom-up methods while achieving both long-range order and strong-coupling. Highly charged NCs with MCC surface ligands self-assembly into large three-dimensional supercrystals and display a complex phase behavior through the destabilization pathway. A high NC polarizability generates increased surface charges relative to low dielectric materials which do not yet have the ability to form dense crystalline structures with MCC surface ligands. Supercrystals assembled from PbS NCs show atomic coherence of the PbS atomic lattices between neighboring particles across micron sized distances and approaches the ultimate limit for strong coupling of semiconductor NCs with small lattice spacings limited by the size of surface ligands.

1.5. Chapter 1 bibliography

1. Yu, W. W.; Peng, X. Formation of High-Quality CdS and Other II–VI Semiconductor Nanocrystals in Noncoordinating Solvents: Tunable Reactivity of Monomers. *Angew. Chem. Int. Ed.* **2002**, *41* (13), 2368–2371.
2. Brus, L. Electronic Wave Functions in Semiconductor Clusters: Experiment and Theory. *J. Phys. Chem.* **1986**, *90* (12), 2555–2560.
3. Donegá, C. de M. Synthesis and Properties of Colloidal Heteronanocrystals. *Chem Soc Rev* **2011**, *40* (3), 1512–1546.
4. García de Arquer, F. P.; Armin, A.; Meredith, P.; Sargent, E. H. Solution-Processed Semiconductors for next-Generation Photodetectors. *Nat. Rev. Mater.* **2017**, *2* (3), 16100.
5. Won, Y.-H.; Cho, O.; Kim, T.; Chung, D.-Y.; Kim, T.; Chung, H.; Jang, H.; Lee, J.; Kim, D.; Jang, E. Highly Efficient and Stable InP/ZnSe/ZnS Quantum Dot Light-Emitting Diodes. *Nature* **2019**, *575* (7784), 634–638.
6. Yang, Z.; Janmohamed, A.; Lan, X.; García de Arquer, F. P.; Voznyy, O.; Yassitepe, E.; Kim, G.-H.; Ning, Z.; Gong, X.; Comin, R.; Sargent, E. H. Colloidal Quantum Dot Photovoltaics Enhanced by Perovskite Shelling. *Nano Lett.* **2015**, *15* (11), 7539–7543.
7. Ackerman, M. M.; Chen, M.; Guyot-Sionnest, P. HgTe Colloidal Quantum Dot Photodiodes for Extended Short-Wave Infrared Detection. *Appl. Phys. Lett.* **2020**, *116* (8), 083502.
8. Dolzhnikov, D. S.; Zhang, H.; Jang, J.; Son, J. S.; Panthani, M. G.; Shibata, T.; Chattopadhyay, S.; Talapin, D. V. Composition-Matched Molecular "Solders" for Semiconductors. *Science* **2015**, *347* (6220), 425–428.
9. Kovalenko, M. V.; Scheele, M.; Talapin, D. V. Colloidal Nanocrystals with Molecular Metal Chalcogenide Surface Ligands. *Science* **2009**, *324* (5933), 1417–1420.

10. Kovalenko, M. V.; Manna, L.; Cabot, A.; Hens, Z.; Talapin, D. V.; Kagan, C. R.; Klimov, V. I.; Rogach, A. L.; Reiss, P.; Milliron, D. J.; Guyot-Sionnnest, P.; Konstantatos, G.; Parak, W. J.; Hyeon, T.; Korgel, B. A.; Murray, C. B.; Heiss, W. Prospects of Nanoscience with Nanocrystals. *ACS Nano* **2015**, *9* (2), 1012–1057.
11. Choi, J.-H.; Wang, H.; Oh, S. J.; Paik, T.; Sung, P.; Sung, J.; Ye, X.; Zhao, T.; Diroll, B. T.; Murray, C. B.; Kagan, C. R. Exploiting the Colloidal Nanocrystal Library to Construct Electronic Devices. *Science* **2016**, *352* (6282), 205–208.
12. Choi, J.-H.; Fafarman, A. T.; Oh, S. J.; Ko, D.-K.; Kim, D. K.; Diroll, B. T.; Muramoto, S.; Gillen, J. G.; Murray, C. B.; Kagan, C. R. Bandlike Transport in Strongly Coupled and Doped Quantum Dot Solids: A Route to High-Performance Thin-Film Electronics. *Nano Lett.* **2012**, *12* (5), 2631–2638.
13. Lee, J.-S.; Kovalenko, M. V.; Huang, J.; Chung, D. S.; Talapin, D. V. Band-like Transport, High Electron Mobility and High Photoconductivity in All-Inorganic Nanocrystal Arrays. *Nat. Nanotechnol.* **2011**, *6* (6), 348–352.
14. Lan, X.; Chen, M.; Hudson, M. H.; Kamysbayev, V.; Wang, Y.; Guyot-Sionnest, P.; Talapin, D. V. Quantum Dot Solids Showing State-Resolved Band-like Transport. *Nat. Mater.* **2020**, *19* (3), 323–329.
15. Li, T.; Senesi, A. J.; Lee, B. Small Angle X-Ray Scattering for Nanoparticle Research. *Chem. Rev.* **2016**, *116* (18), 11128–11180.
16. Boles, M. A.; Engel, M.; Talapin, D. V. Self-Assembly of Colloidal Nanocrystals: From Intricate Structures to Functional Materials. *Chem. Rev.* **2016**, *116* (18), 11220–11289.

17. Zabet-Khosousi, A.; Trudeau, P.-E.; Suganuma, Y.; Dhirani, A.-A.; Statt, B. Metal to Insulator Transition in Films of Molecularly Linked Gold Nanoparticles. *Phys. Rev. Lett.* **2006**, *96* (15), 156403.

2. Synthesis and electrostatic stabilization of charged colloidal nanocrystals

2.1. Introduction

Quantum confined semiconductors have been the focus of considerable research efforts due to the size dependent absorption and emission properties and high degree of control over the size, shape, and surface chemistry of solution processed nanocrystals (NCs) with diameters smaller than the Bohr exciton radius. The relatively cheap solution-based synthesis of crystalline semiconducting materials has accelerated NC research for optoelectronic applications including visible and near infrared (IR) light emission,[1,2] photovoltaics,[3,4] and solar concentrators.[5] Sensing applications based on NCs in the near IR are becoming increasingly relevant, especially with the growing demand for camera technologies in the era of smartphone cameras and self-driving cars,[6] which require the ability to see through fog or in low-light conditions. Mercury chalcogenide NCs have been widely explored as IR absorbers for sensors with small bandgaps in the mid and far IR while lead chalcogenide NCs (PbS, PbSe, and PbTe) have size tunable bandgaps that span across most of the near IR (800-5000 nm).

This chapter focuses on the properties of PbS NCs with particular attention to high-quality, high-yield NC synthesis from organic solutions. I also detail the ligand exchange of PbS surfaces with multivalent metal chalcogenide complex (MCC) ligands which greatly increases the coupling strength between NCs compared to organic ligands due to the increased conductivity of the inorganic infill and smaller interparticle spacings in thin film applications. The surface chemistry of MCC capped PbS NCs is examined along with the structure factors of PbS colloidal solutions with highly charged surfaces. Finally, I quantify the strength of the repulsive interparticle interactions by experimentally measuring the second virial coefficient of charged PbS NCs in polar media.

2.2. PbS nanocrystal synthesis and characterization

The synthesis of PbS NCs typically involves the rapid injection of a reactive sulfur precursor into a hot solution (90-150 °C) of lead oleate in a high-boiling organic solvent such as 1-octadecene (ODE) (Figure 2-1A). The three most common PbS syntheses involve the hot-injection of $(TMS)_2S$ into a solution of lead oleate,[7,8] hot-injection of a sulfur-oleylamine solution into a solution of lead chloride and oleylamine,[9] and hot-injection of a thiourea into a solution of lead oleate.[10] Of these three methods, the use of substituted thioureas with varying reactivity produces the highest quality PbS NCs in large quantities (Figure 2-2). While the synthesis from lead chloride also yields highly monodisperse PbS, the final NC surface contains many lead-chloride bonds which is not desirable for future ligand exchange with MCC ions. By contrast, the preparation demonstrated by Hendricks *et al.* generates PbS NCs with clean surfaces, narrow size distributions, and high yields.

The final size of PbS NCs can be controlled with a high degree of repeatability by changing the reactivity of the substituted thiourea (Figure 2-1B) as well as the reaction environment. For example, similar synthetic conditions for PbS synthesized with thiourea 4 leads to larger NC sizes at higher temperatures (Figure 2-3A). While the exact reason for the temperature dependence can be due to multiple factors, thiourea 4 has a slow (~30 seconds) onset of nucleation at 90 °C and slower growth kinetics compared to the rapid (~3 seconds) onset of nucleation at 120 °C and faster growth. Altogether, the suppressed reactivity limits the growth of NCs while nucleation persists throughout the growth process and the reaction temperature leads to a self-limiting effect due to size and temperature dependent growth kinetics.[11,12] Changing the reaction solvent also has a large influence on the final PbS NC size with ~7 nm and ~5.8 nm PbS NCs produced using 1-octadecene and 1-octene solvents under identical reaction conditions, respectively (Figure 2-3B). The

difference in viscosity between the two solvents changes the reaction kinetics with monomers diffusing more slowly in the more vicious ODE solvent compared to octene.

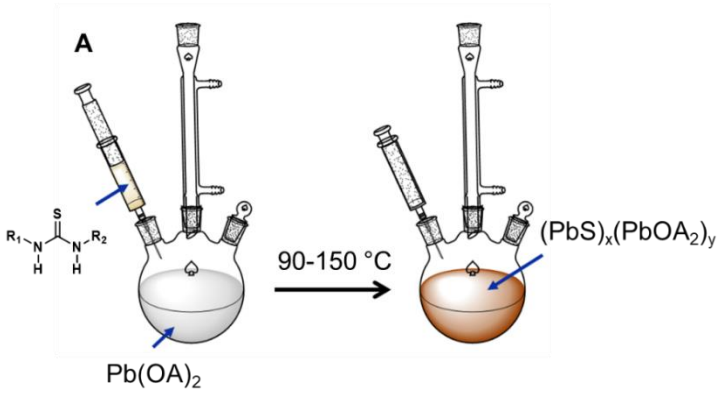

B

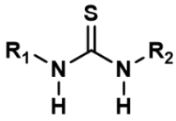

Thiourea	R_1	R_2
1	Ph	Ph
2	4-CN-Ph	$C_{12}H_{25}$
3	4-CF_3-Ph	$C_{12}H_{25}$
4	Ph	$C_{12}H_{25}$
5	C_6H_{13}	$C_{12}H_{25}$

Figure 2-1: Overview of PbS nanocrystal synthesis.

(**A**) Schematic of PbS nanocrystal synthesis by hot-injection of a thiourea solution into a hot solution of lead oleate, $Pb(OA)_2$. (**B**) Table of substituted thioureas used in synthetic studies previously developed by Hendricks et al.[10]

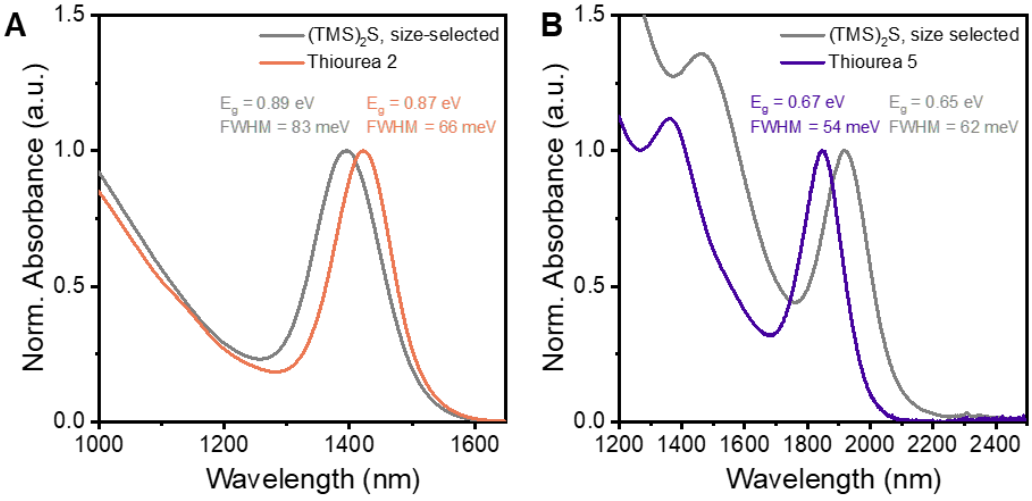

Figure 2-2: Comparison of PbS NCs synthesis using $(TMS)_2S$ vs thiourea precursors.

Both (**A**) 0.89 eV and (**B**) 0.65 eV bandgap PbS samples synthesized from $(TMS)_2S$ were washed with significant size-selective precipitation resulting in relatively low NC yields. PbS synthesized with thioureas 2 and 5 did not undergo size selection and have narrower NC size distributions with yields of >1 g of PbS.

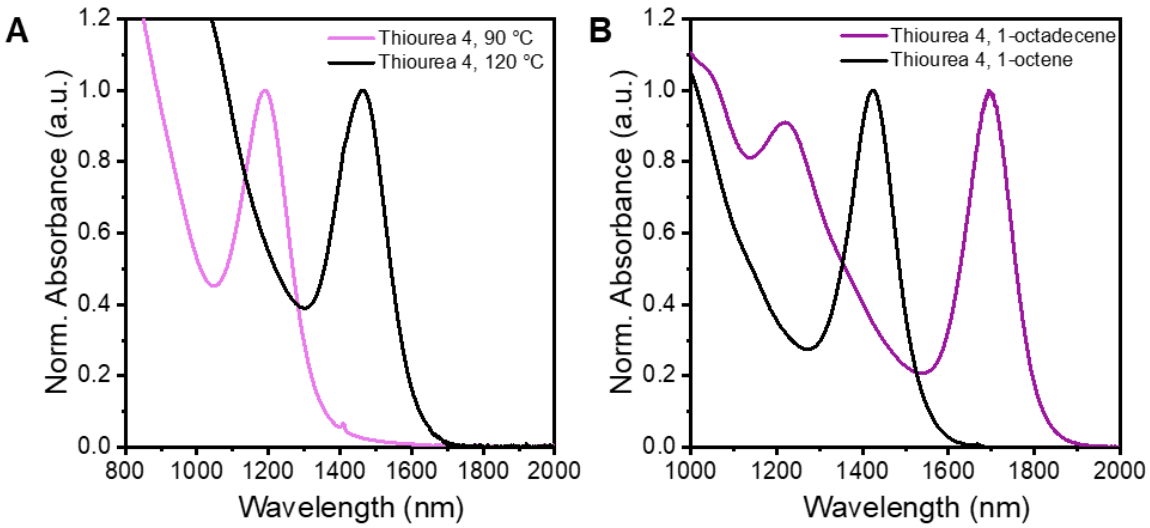

Figure 2-3: PbS synthesis temperature and solvent dependence.

(**A**) Temperature dependence of PbS NC synthesis in 1-octene. (**B**) Solvent dependence of PbS NCs synthesized at 120 °C due to a change in solvent viscosity.

While most nanocrystal syntheses are performed by injection of a chalcogenide solution into a hot flask containing a metal precursor, many efforts have been put towards the one-pot synthesis of NCs removing the variability of precursor injection rate, splashing, and temperature depression upon injection.[13] In the one-pot approach, all precursors are loaded into one flask and the experiment is simplified to depend solely on the heating rate which can be highly reproducible. In many NC preparations, the precursors are highly reactive and cannot be combined at low temperatures without reacting. The tunable reactivity of substituted thioureas, however, serves as an ideal platform for a heat up synthesis as the thiourea and lead oleate do not react until ~70 °C. Indeed, high quality PbS NCs are synthesized from multiple thioureas using a heat-up synthesis with monodispersity similar to that of the equivalent hot-injection reaction (Figure 2-4). The PbS NCs synthesized by heat-up have a consistently larger size (ignoring the outlier of thiourea 2) which can be explained by the onset of nucleation at lower temperatures and growth at temperatures higher (0-10 °C) than the equivalent hot-injection reaction. As the PbS NCs grow in

the one-pot reaction, the reaction temperature increases at the maximum heating rate and eventually plateaus at a slightly higher temperature than the constant temperature achieved during hot-injection. The growth kinetics of PbS NCs have been shown to be dependent on NC size and temperature, so it is unsurprising that higher temperatures in the heat-up synthesis lead to larger NCs with increased growth rates.[12]

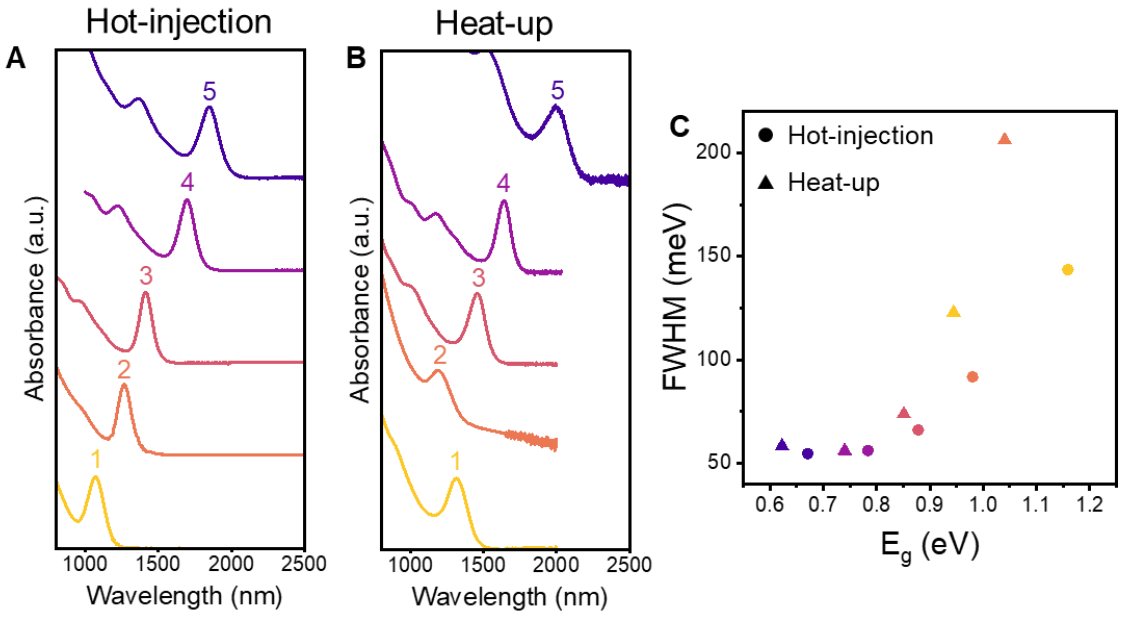

Figure 2-4: Comparison of hot-injection and heat-up PbS NC synthesis.

(**A**) Offset absorbance spectra of PbS NCs synthesized by hot-injection of thioureas 1-5 in ODE. Reaction temperatures are 90, 120, 120, 120, and 150 °C, respectively. (**B**) Heat-up PbS NC synthesis with thioureas 1-5 dissolved in ODE. Temperature is quickly raised to the equivalent hot-injection temperature with an ~10 °C overshoot and slow decrease. (**C**) Comparison of PbS FWHM and bandgaps (E_g) from PbS absorbance data.

The air stability of PbS NCs has often been a claim made in synthetic works. In some cases, the surface chemistry protects the PbS surface from oxidation due to strong binding of small ions (e.g., Cl^-).[9] In syntheses where oleic acid is the only ligand present, the air stability of PbS has a strong size dependence due to the highly faceted surfaces and size dependent NC shape.[14] PbS

NCs >4 nm take the shape of a truncated octahedron with exposed (111) and (100) surface facets. The (111) surfaces are well protected from oxidation by oleic acid ligands, but (100) surfaces can be easily oxidized from air exposure (Figure 2-5A). Upon oxidation, the excitonic peak in the NIR blue shifts and narrows from the formation of small amounts of PbO which changes the effective Bohr radius of the NC and has a partial type-I core-shell effect due to the high bandgap of PbO relative to PbS. Exposure to oxygen during the synthesis also affects the final PbS NCs size, with the excitonic peak blue shifted relative to the nitrogen control due to both oxidation and a smaller NC diameter (Figure 2-5B).

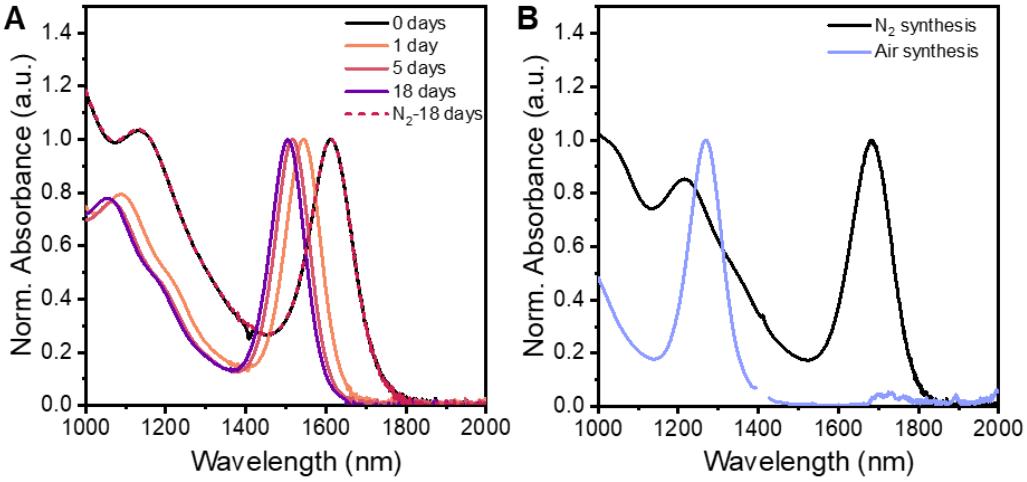

Figure 2-5: Air stability of PbS NCs.

(**A**) Absorbance of a PbS NC solution in hexane stored in air and in a nitrogen filled glovebox for 18 days. Air-exposure produces a clear blue shift and peak narrowing due to surface oxidation. (**B**) PbS synthesis from thiourea 4 performed under nitrogen and exposed to air resulting in a smaller final NC size.

The air stability of PbS NCs is an important consideration given that the location of the excitonic peak in the NIR is commonly used to determine the average NC diameter by applying a published correlation between NC TEM size and optical bandgap (Figure 2-6A).[15] Here, I extract the average NC size from small angle X-ray scattering (SAXS) data (Figure 2-6B) and show that a size-dependent offset exists between PbS diameters determined by SAXS and TEM. A sizing

curve was fit to experimental SAXS data (Figure 2-6A, red line) limited by the bulk PbS bandgap (E_g=0.41 eV) at large diameters:

$$E_g = 0.41 + \frac{1}{0.0354d^2 + 0.169d}$$

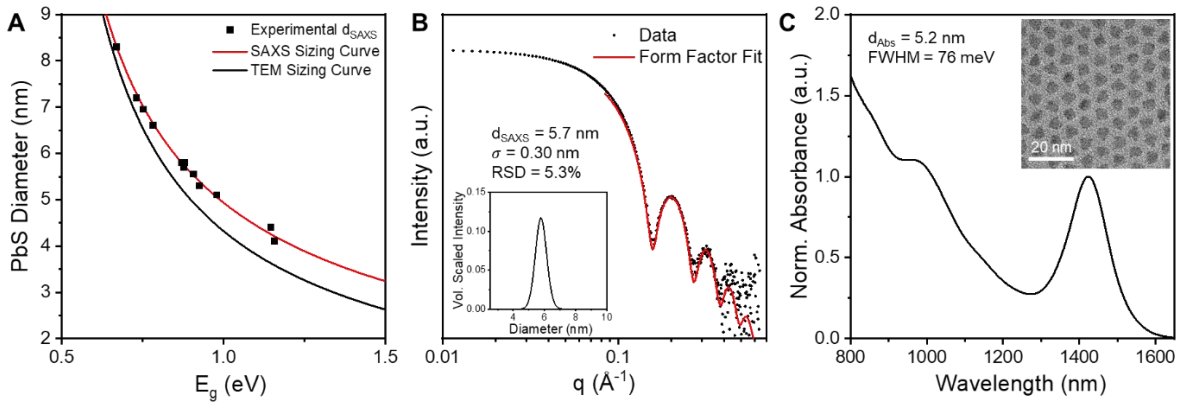

Figure 2-6: PbS nanocrystal size determination.

(**A**) Sizing curve of PbS-OA samples in hexane with experimental diameters determined by SAXS fitting and bandgaps determined from solution absorbance with no air exposure. Red line is a fit to experimental SAXS data. Black line is a previously measured PbS sizing curve based off of TEM analysis of NC diameters.[15] Large deviations between the two methods exists for small PbS diameters due to non-spherical geometry. (**B**) SAXS fitting of a 5.8 nm PbS-OA in hexane. Inset shows extracted volume scaled size distribution with a relative standard deviation of 6%. (**C**) Absorbance of the same PbS-OA NC sample in panel B which has a predicted size of 5.2 nm based on the TEM sizing curve. Inset: TEM image of PbS-OA NCs.

The offset between the SAXS and TEM sizing curves is >0.6 nm for small NC sizes where the PbS NC shape can become non-spherical and the ligand electron density contributes a larger fraction to the overall NC electron density. SAXS form factor fitting assumes a spherical NC shape which can be a good approximation for large PbS diameters with truncated octahedron and rounded cube shapes, but small NCs with octahedral shapes significantly deviate from the spherical form factor. Accurate size determination of small octahedral NCs is also a difficult task by TEM, especially when estimating a circular cross section through a non-spherical NC at various

focal planes, and it is possible that the published TEM sizing curve also has a small offset for small PbS diameters. Even with a systematic discrepancy between the two sizing methods, it is useful to gather the SAXS sizing information for the following analysis on PbS colloids which relies heavily on SAXS data and form factor modeling. Herein, all NC diameters are referred to as the size extracted from SAXS with organic surface ligands.

2.3. Surface chemistry characterization of MCC capped semiconductor nanocrystals

Colloidal nanocrystals are traditionally synthesized with organic surface ligands, but for applications of NC materials in thin films the presence of extended organic ligands and large interparticle spacings prevent conduction pathways from forming between neighboring NCs. Previous reports have detailed the synthesis of metal chalcogenide complexes (MCCs) which bind to NCs surfaces and facilitate phase transfer from non-polar solvents to highly polar solvents such as N-methylformamide (NMF), formamide (FA), N-methylpropionamide (NMPA), and hydrazine.[16,17] Here, I use $K_4Sn_2S_6$, K_3AsS_3, and K_4GeS_4 surface ligands to exchange PbS NCs from hexane to NMF (Figure 2-7). The presence of chalcogenide based ligands on the PbS NC surface produces a red shift of the PbS excitonic peak due to the larger electron delocalization across the inorganic NC and ligand and effectively weaker quantum confinement. The colloidal stability of the PbS solutions is determined by SAXS (Figure 2-7C). The form factor of the PbS NCs remains largely unchanged confirming that the NC shape does not change during the ligand exchange while the low-q scattering deviates due to the presence of additional structure factor in the PbS colloids. The decrease (increase) in scattering for Sn_2S_6 and AsS_3 (GeS_4) surface ligands implies a highly repulsive (slightly attractive) interparticle potential. The exact form of these low-

q structure factors can be used to extract quantitative interparticle interactions by means of the second viral coefficient (see section 2.7).

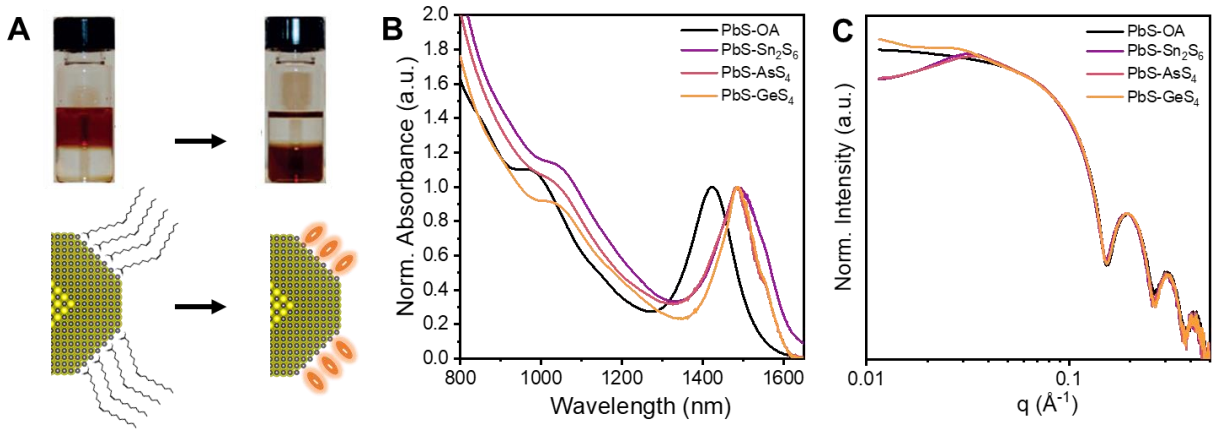

Figure 2-7: Nanocrystal ligand exchange into polar solvents.

(**A**) Top: Picture of NC phase transfer from hexane (top layer) to NMF (bottom layer). Bottom: Schematic of PbS NC surface chemistry from oleic acid to charged MCC ligands. Normalized absorbance (**B**) and normalized SAXS (**C**) of 5.8 nm PbS NCs before and after ligand exchange from hexane into NMF with three MCC ligands.

While the core PbS NC size does not change in size or shape after ligand exchange with MCC anions, the effective diameter extracted by SAXS fitting can be significantly larger than the corresponding NC with organic ligands. This effect is seen clearly for small NCs, where the effective NC diameter increases from 4.1 to 4.5 nm (Figure 2-8A). SAXS is sensitive to the electron density of the particle, and the electron density contrast between the PbS NC core and ligand is extremely large. Moving from oleic acid to Sn_2S_6 increases the electrons per ligand by ~24% with higher electron densities in the relatively small MCC ligands (~0.5 nm) compared to oleic acid (~2 nm) which should explain the observed increase in NC diameter. This effect is relatively small for large 8.2 nm PbS NCs where the total NC volume is 8 times larger than the 4.1 nm NCs which should help the NC core dominate the total scattering intensity (Figure 2-8B).

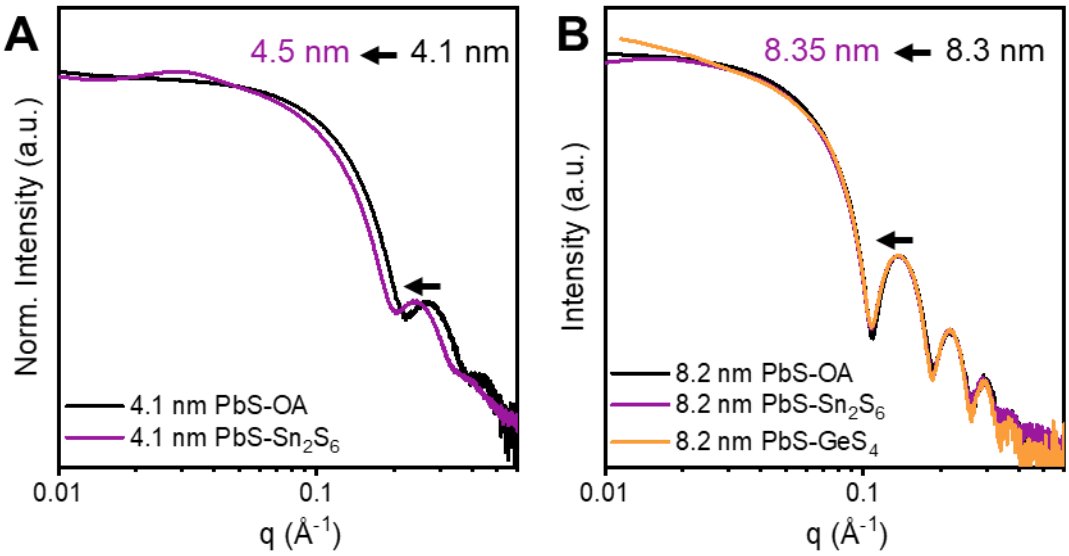

Figure 2-8: Ligand dependent size broadening of PbS NCs by SAXS.

Effective PbS NC size increase after ligand exchange from carbon based oleic acid to inorganic MCC ligands. Small NCs have a relatively large shift in the form factor (**A**) while large NCs have a smaller ligand contribution (**B**).

A similar ligand exchange was performed on zinc blende CdSe NCs by exchanging native oleic acid ligands with $K_4Sn_2S_6$, K_3AsS_3, and K_4GeS_4 (Figure 2-9). CdSe NCs were synthesized by a previously reported method using cadmium myristate and selenium dioxide.[18] The absorbance of the CdSe NCs main excitonic peak at 574 nm remains largely unchanged after ligand exchange with MCC ligands, but the binding of GeS_4 ligands retains a small amount of band edge emission from the NCs with low quantum yields while no emission is observed from NCs with Sn_2S_6 or AsS_3 ligands (Figure 2-9A, inset). The reason for this emission may be that the band alignment of GeS_4 is wide enough to form a type-I structure with the CdSe NCs while smaller bandgaps of Sn_2S_6 and AsS_3 form type-II structures which trap excitons and quench emission. SAXS analysis of the CdSe NC solutions in NMF show no change in the NC form factor after ligand exchange, and only CdSe with Sn_2S_6 ligands shows decreased scatting at low q indicating a net repulsive interparticle interaction. Previous reports on the ligand exchange of CdSe with thiostannate anions

commonly used hydrazine, but I show here that hydrazine is not a benign solvent to the CdSe NC size or shape with a significantly different form factor than the same NCs exchanged into NMF (Figure 2-9C).

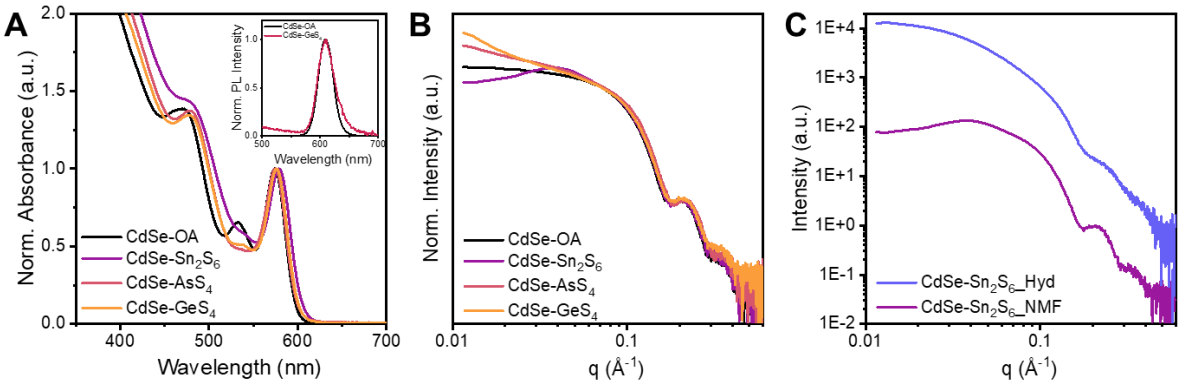

Figure 2-9: MCC ligand exchange of CdSe NCs into polar solvents.

(**A**) Normalized absorbance of 4.4 nm CdSe with oleic acid ligands in hexane, and MCC inorganic ligands in NMF. Inset: Normalized photoluminescence spectra showing band edge emission from oleic acid and GeS_4 capped CdSe. (**B**) Normalized SAXS of 5.4 nm CdSe with oleic acid ligands in hexane and MCC ligands in NMF. (**C**) Offset SAXS of 5.4 nm CdSe exchanged with thiostannate ligands into both NMF and hydrazine, with significant NC size and shape change in hydrazine relative to the initial NCs.

Elemental analysis of MCC capped PbS NCs allows for the calculation of ligand grafting densities to NC surfaces. I digest NCs according to previously established protocols for semiconductor NCs and perform elemental analysis by inductively coupled plasma optical emission spectroscopy (ICP-OES).[19] NC solutions are washed with acetonitrile after ligand exchange to remove excess free ligands, but elemental analysis alone cannot differentiate between free and bound ligands. Here, I perform a series of dialysis experiments using centrifugal dialysis filters where solvent and free ligand can diffuse through membrane pores while the large NCs cannot travel through the membrane. Three cycles of dialysis are performed, each with an effective dialysis ratio of 5x, and the grafting density on 5.8 nm PbS in NMF is tabulated in Figure 2-10A. Thiostannate ligands have an initial grafting density of 0.75 which decays to 0.55 ligands per nm^2

after three cycles while arsenic sulfide ligands decay from 2.89 to 2.25 ligands per nm^2. Germanium sulfide ligands, however, do not leave the PbS surface with a constant grafting density of 1.23 ligands per nm^2. The loss of ligands per NC does not necessarily come only from initially free ligands as the equilibrium distribution between free and bound ligands can change and bound ligands partially desorb from the NC surface.

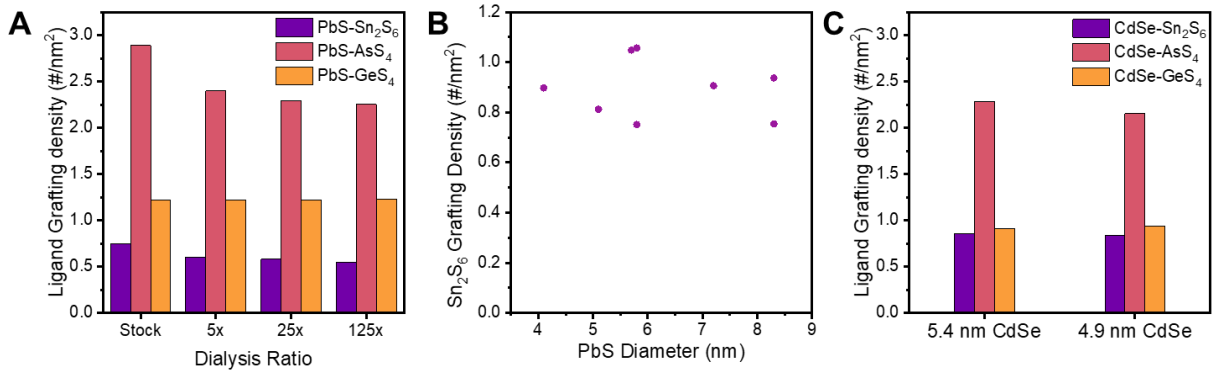

Figure 2-10: Elemental analysis of nanocrystal MCC ligand grafting density.

(**A**) MCC ligand grafting densities on 5.8 nm PbS NCs in NMF through increasing dialysis cycles. Thiostannate and arsenic sulfide ligand density slightly decays as free ligand is eliminated and free vs bound ligand equilibrium shifts, while germanium sulfide ligands remain strongly attached. (**B**) Thiostannate grafting densities on PbS NCs of various sizes in NMF. No dialysis was applied. (**C**) MCC ligand grafting densities on two sizes of CdSe NCs in NMF.

The amount of residual free MCC ligand in solution could be highly variable based on the efficiency of sample washing and could drastically change the behavior of electrostatically stabilized colloids with varying solution ionic strengths. To test for sample consistency of PbS with thiostannate ligands in NMF, a series of PbS NC sizes were analyzed for ligand grafting density with no dialysis performed (Figure 2-10B). The thiostannate grafting density varies from 0.75-1.05 ligands per nm^2 which is reasonable based on previous reports of thiostannate binding to CdSe NCs in NMF.[20] Elemental analysis of two sizes of CdSe NCs in NMF reveals similar

ligand grafting density for Sn_2S_6 and AsS_3, with a slightly lower density of GeS_4 ligands (0.92 ligands per nm^2).

Thus far, I have proposed that the stoichiometry of thiostannate ligand molecules is Sn_2S_6, but multiple forms of tin sulfide have previously been observed in polar solvents including SnS_4 and Sn_2S_7.[17,20] NMR analysis of the ^{119}Sn nucleus from thiostannate ligands in both NMF and FA show only one peak at 55 ppm corresponding to Sn_2S_6 (Figure 2-11). Adding excess sulfide in the form of K_2S does not affect the thiostannate structure with no additional Sn chemical environments observed. The anhydrous NMF used in experiments is distilled and stored over molecular sieves, but similar experiments with non-anhydrous NMF did not change the thiostannate stoichiometry.

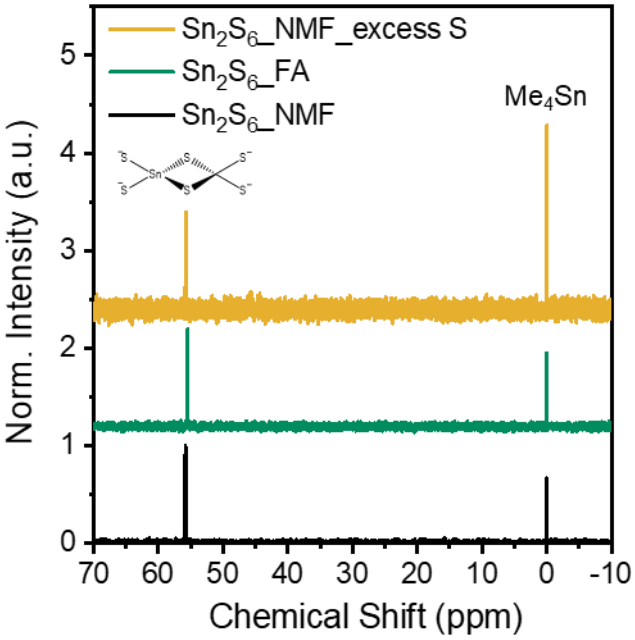

Figure 2-11: Chemical identification of thiostannate in polar solvents.

^{119}Sn NMR spectra of $K_4Sn_2S_6$ synthesized in NMF. Data are normalized to the thiostannate peak at 55 ppm and offset for clarity. Tetramethyl tin is used as a chemical shift reference (0 ppm). Middle sample in formamide (FA) was synthesized in NMF, then precipitated with acetonitrile and redispersed in FA. Excess sulfide (yellow trace) did not affect the Sn chemical environment.

2.4. Structure factors of MCC capped nanocrystal solutions

The structure factor, S(q), of an ideal solution consisting of non-interacting particles would be equivalent to S(q)=1 across all scattering angles. The physical meaning of a structure factor of unity is the absence of any interparticle interaction, and any observable SAXS intensity would come from the shape dependent form factor, or effectively intraparticle scattering. The total SAXS intensity is given as the product of both the form factor and structure factor:

$$I(q) = S(q)P(q)$$

In reality, colloidal NCs do not behave as ideal gasses and always have a net attractive or repulsive potential which impacts the observed structure factor. Weakly interacting systems (e.g., NCs with organic ligands) show only small deviations from S(q)=1, but NCs with high surface charge densities can have strong repulsive interactions and show large structure factors under conditions where the screening length, or range of the interaction potential, is long compared to the particle size (Figure 2-12). The Debye length, κ^{-1}, estimates the range of interparticle interaction based on the solvent dielectric constant, ε, and the ionic strength, I:

$$\kappa^{-1} = \sqrt{\frac{\varepsilon_{sol}\varepsilon_0 k_B T}{2e^2 I}}$$

For PbS NCs in NMF with a background thiostannate concentration of ~0.5 mM, the Deybe length is equal to ~8.2 nm which corresponds to a $1/e$ decay in the electrostatic potential form the NC surface. A common form of the pair potential decaying from the NC surface is the Yukawa potential which takes the form of exponential decay from a cutoff length at the NC+ligand surface (Figure 2-12C).[21]

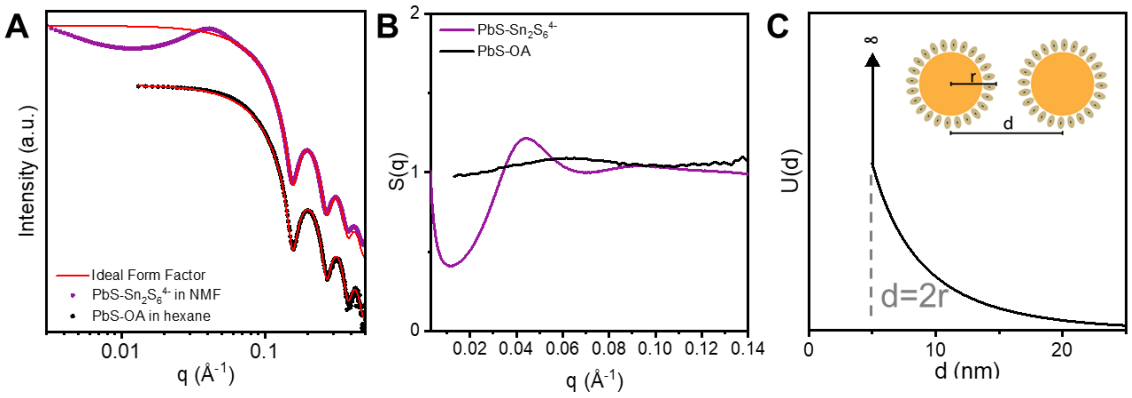

Figure 2-12: Structure factor of charged PbS NC colloids.

(**A**) Offset SAXS of 5.7 nm PbS NCs with oleic acid ligands in hexane and thiostannate ligands in NMF. Red line overlays the form factor for 5.7 nm spheres with significant deviation for the charged PbS NCs. (**B**) Extracted structure factors calculated by dividing data in panel A by the form factor (red line). Clear interparticle correlations are observed for MCC capped PbS while organic ligands have minimal structure factor. (**C**) Example Yukawa potential for charged spheres interacting through a repulsive potential with long screening lengths.

The strength of repulsive NC interactions ideally does not depend on the NC concentration, but the structure factor of charged NCs has a strong dependence on concentration due to the changing average distance between diffusing colloidal particles (Figure 2-13). Multiple correlation peaks emerge in the structure factor at increasing q values for higher concentrations. The peak position from the structure factors is correlated against the cubed root of the NC number density and shows a linear trend. The experimental values are in close agreement with the theoretical maximum slope based on a geometric calculation of interacting spheres at infinitely low ionic strength (i.e. infinitely long screening length) providing additional evidence that MCC capped NCs interact through long range pair potentials.[21]

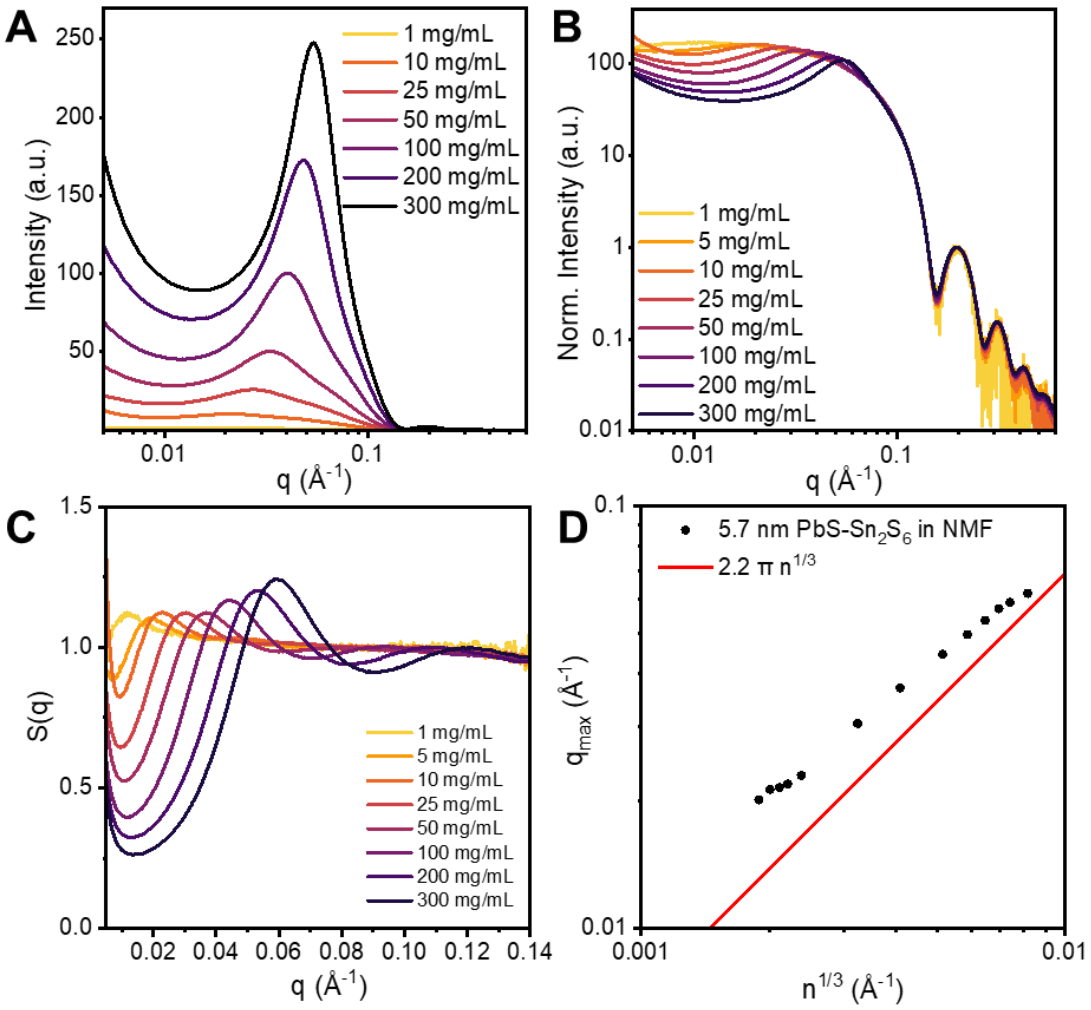

Figure 2-13: Concentration dependence of MCC capped PbS structure factor.

(**A**) Lin-log plot of background subtracted SAXS data for 5.7 nm PbS-Sn_2S_6 NCs in NMF. (**B**) Log-log plot of SAXS data from panel A normalized to the first-order form factor peak. (**C**) Extracted structure factors for same PbS NCs showing a concentration dependent correlation peak. (**D**) Log-log plot of q_{max} positions from solution structure factors plotted against $n^{1/3}$ where n is the NC number density. Red line shows geometric calculation for correlation at infinitely low ionic strength.

Adding additional ligands to a solution of MCC capped PbS NCs in NMF decreases the screening length and decreases the total repulsive interaction between NCs (Figure 2-14). As a result, the structure factors are reduced with little interparticle correlations observed by SAXS at concentrations of 5 mM K_3AsS_4 and above. For NC solutions with identical concentrations (50

mg/mL), the relative increase in low q scaling (q = 0.008-0.02 $Å^{-1}$) as the ligand concentration increases directly corresponds to the transition from a net repulsive to net attractive interaction potential. At 20 mM, low q scattering also greatly increases in intensity from the formation of small clusters of NCs in solutions.

The primary solvent to stabilize charged PbS NCs is NMF due to its anomalously high dielectric constant at room temperature ($\varepsilon_{NMF} = 171$) compared to most polar solvents. Within the same solvent family, N-methylpropionamide (NMPA, $\varepsilon_{NMPA} = 163$) and formamide (FA, $\varepsilon_{FA} = 109$) can also stabilize PbS-Sn_2S_6 NCs (Figure 2-15).[22] NMPA has a higher viscosity than NMF and struggles to achieve high concentrations above 50 mg/mL due to mixing limitations, but 150 mg/mL solutions can readily be formed with FA. SAXS intensities and structure factors for NCs dissolved in NMPA behave identically to NMF, but structure factors in FA do not follow the same trend. Formamide's lower dielectric constant could play a role in the change in behavior, but a more likely explanation is the molecular stability of FA solvent molecules surrounding the NC or a low donor number toward the coordination of FA to the NC surface. A high background concentration of ions in the FA sample is not observed which could help explain the reduction in repulsive potential. A mixed solvent of NMF and of 75:25 NMF:DMF creates a dielectric environment similar to that of FA,[23] but the structure factor observed in pure NMF solvents is maintained with the only difference being a slightly shorter screening length (Figure 2-16).

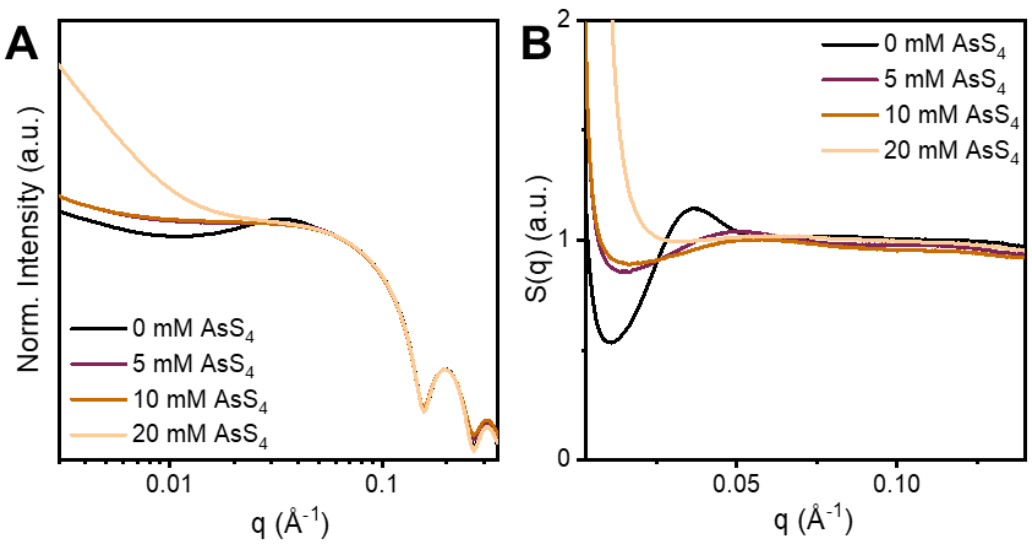

Figure 2-14: Ionic strength dependent structure factor.

(**A**) Normalized SAXS of 5.7 nm PbS-Sn_2S_6 NCs in NMF at 50 mg/mL PbS with increasing concentration of K_3AsS_4. (**B**) Extracted structure factors show a decrease in interparticle correlations as the screening length is decreased (higher ionic strength).

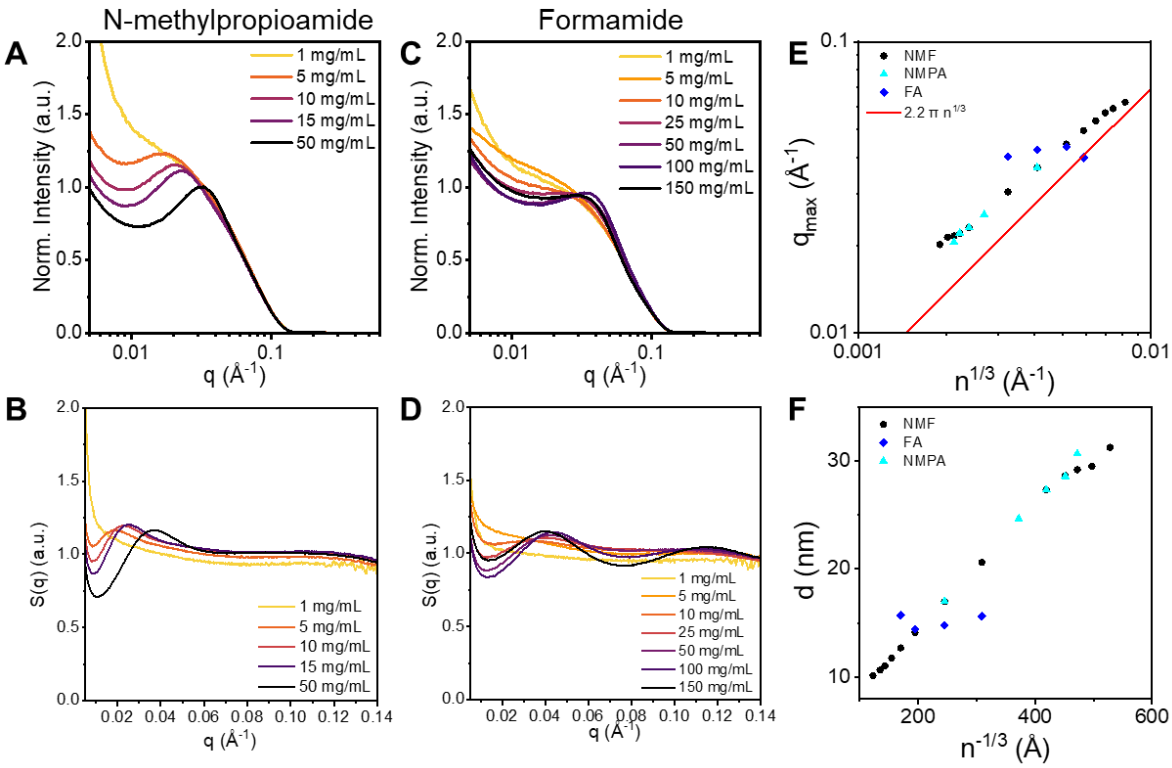

Figure 2-15: Solvent dependent PbS structure factor.

Normalized SAXS and extracted structure factors show N-methylpropionamide (NMPA) behaves similarly to NMF as a solvent for charged PbS NCs (**A,B**), but formamide (FA) has different scattering intensities at low q (**C,D**). (**E**) NMF and NMPA structure factor peak positions follow the same trend plotted against the cube root of number density (n) while FA shows different behavior. Red line shows geometric prediction for correlation at infinitely low ionic strength. (**F**) Data from panel E replotted as d spacing vs $n^{-1/3}$.

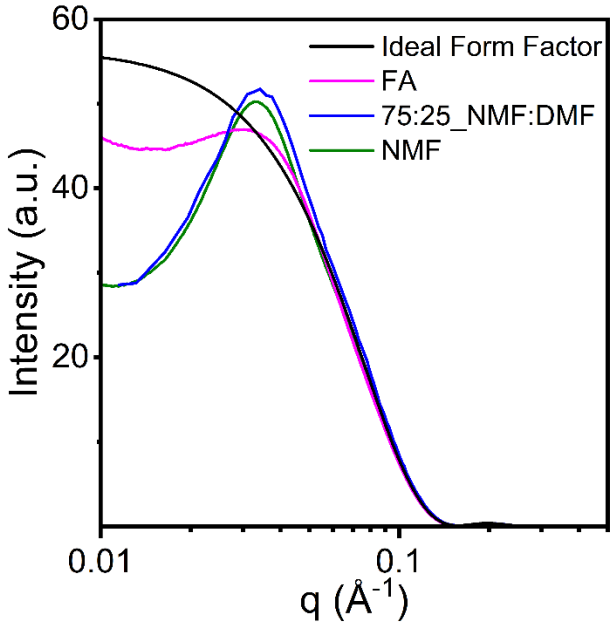

Figure 2-16: Solution structure factors from formamide family solvents.

Lin-log SAXS plot of 5.7 nm PbS-Sn_2S_6 at 50 mg/mL stabilized in NMF, FA, and 75:25 NMF:DMF. The NMF and mixed NMF:DMF solutions show similar structure factors but the sample in FA shows different behavior. Ideal form factor is calculated for 5.7 nm spheres.

Attempts to stabilize PbS-Sn_2S_6 NCs in additional polar solvents including DMF, ethanolamine, hydrazine, and water, do not result in colloidal solutions as observed by SAXS analysis (Figure 2-17). NCs dissolve into the solution and a homogenous black liquid is formed, but NCs cannot stabilize themselves and establish the screening lengths necessary to break out of aggregates. Hydrazine is a particularly bad solvent for PbS as it etches the NC into small clusters within minutes after contact with the NC surface.

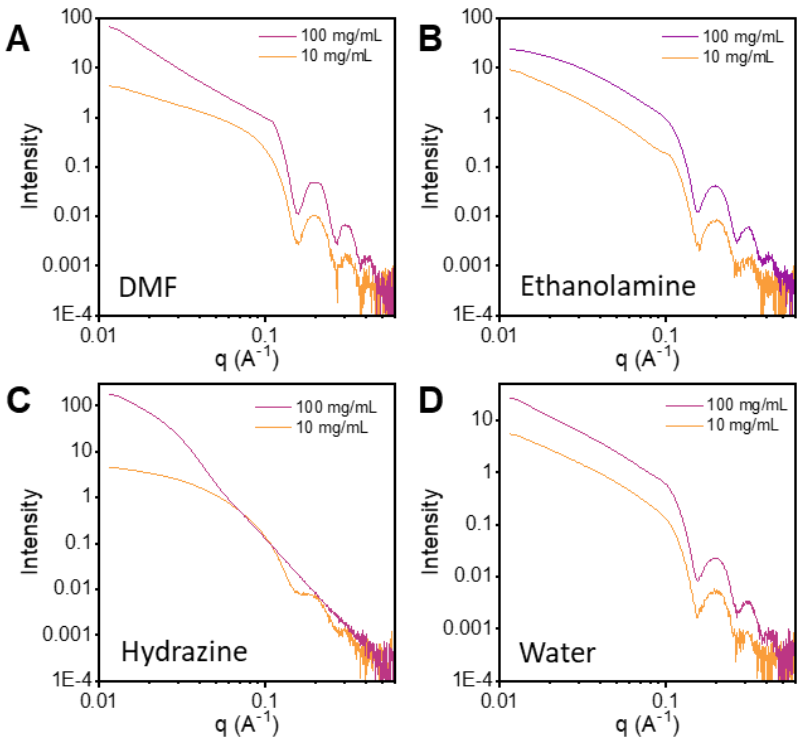

Figure 2-17: Colloidal instability of PbS NCs in non-formamide solvents.

SAXS of 5.7 nm PbS-Sn_2S_6 NCs precipitated from NMF and redispersed into (**A**) DMF, (**B**), ethanolamine, (**C**) hydrazine, and (**D**) water. All solutions appear homogeneous and well dispersed by eye, but lack complete colloidal stability as observed by significant scattering tails in the Guinier region of the SAXS spectra.

2.5. Quantification of interparticle interactions through the second virial coefficient

Charged NCs in polar solvents maintain colloidal stability through repulsive, electrostatic interactions, but experimentally quantifying the magnitude of these interparticle interactions is a challenging problem with traditional NC characterization. Colloidal stability is often determined solely from common absorption measurements, and the absence of a wavelength dependent scattering tail is enough for most to claim a repulsive potential with the absence of large agglomeration in solution. Moving to dynamic light scattering experiments can provide sizing information on both single particles and clusters in solution, and Zeta potentials offer some insight

on the NC surface charge but in practice can be highly unreliable for quantitative measurements especially in systems with multivalent or complex ligands and salts. Similarly, elemental and chemical analysis (e.g., ICP-OES, NMR) to determine the surface structure and grafting density of charge ligands can provide only estimates of a surface charge density though highly involved analysis and still require theoretical calculations to estimate any interparticle interactions.

The true measure of NC interparticle interactions can be determined by treating each NC as a non-ideal 'gas' molecule and applying the virial equation of state as an expansion of the ideal gas law around the particle density, ρ:

$$\frac{P}{kT} = \rho + B_2(T)\rho^2 + B_3(T)\rho^3 + \cdots$$

Here, the coefficients at each power term correspond to a measure of an effective interaction potential, with $B_2(T)$ as the two-body interaction term which has the largest contribution to non-ideal interparticle interactions.[24] Positive $B_2(T)$ values are defined as repulsive interactions while negative values are defined as attractive. Three-body interactions and higher order terms have relatively low contributions, especially at low concentrations, and are ignored for the purposes of the following analysis. It should be noted that the virial state equation breaks down at high concentrations where solutions cannot be approximated as near-ideal, and also uses the assumption that particles occupy no volume as an ideal gas. Further corrections such as the van der Waals equation remove this assumption and incorporate an excluded volume term for the non-zero density of interacting particles.[25]

The second virial coefficient has units of volume, and the physical interpretation can be thought of as a correction to the total volume the particle occupies up in solution. From a known interparticle potential, $U(r)$, the second virial coefficient can be calculated by performing a radial integration:

$$B_2 = -2\pi \int (e^{-U(r)/kT} - 1) r^2 dr$$

In practice, the exact pair potential is not known, but can be approximated by a model such as the Yukawa potential for charged hard spheres interacting through repulsive coulomb potential.[21] Information about the pair potential can be gained by experimentally measuring B_2 across a series of conditions using a form of static light scattering. For example, protein solutions have commonly been measured by visible static light scattering experiments, and the self-assembly behavior of protein solutions has been predicted by the resulting B_2 values.[26] Semiconductor nanocrystals, however, often have significant visible light absorption limiting the utility of visible static light scattering experiments relative to those for proteins. Instead, X-ray scattering is used to increase the sample transmittance and to gain extended spatial resolution by simultaneously collecting many scattering angles on one detector. Two previous examples have used X-ray scattering to measure the B_2 of metallic Au and insulating metal oxide nanocrystals,[27,28] both capped with organic ligands in non-polar solvents. Herein, I will perform a similar analysis to determine the B_2 values of charged PbS NCs in polar solvents.

2.6. Determination of charged PbS nanocrystal second virial coefficients by quantitative small angle X-ray scattering

Nanocrystal interparticle interactions are quantified by measuring the second virial coefficient (B_2) which can be extracted from the structure factor of colloidal solutions by small angle X-ray scattering. In general, a relative increase in structure factor as the NC concentration increases indicates an attractive interparticle interaction which would yield a negative B_2 value. Highly charged particles, however, should see a decrease in structure factor with increasing NC concentration due to the repulsive potential, a behavior expected for the system studied here of

PbS-Sn_2S_6 NCs in a high dielectric medium of N-methylformamide (NMF, $\varepsilon_{NMF} = 170$). The first method I use to extract B_2 from charged PbS NCs models the concentration dependent SAXS intensity by a Zimm analysis and was first used to model Au NCs capped with dodecanethiol ligands.[27,29]

First, the osmotic second virial coefficient (A_2) is determined from SAXS data which quantifies the interparticle interactions from the perspective of solvent molecules in the system. The statistical second virial coefficient can be easily calculated from A_2 using the ratio of solvent and NC molar volumes, v_c:

$$B_2 = A_2 v_c \frac{MW_{NC}^2}{N_A}$$

where MW_{NC} is determined from the nanocrystal size distribution extracted from SAXS data:

$$MW_{NC} = N_A \frac{\sum n_r m_r^2}{\sum n_r m_r}$$

where n_r is the NC number fraction and m_r is the NC mass with radius, r (Figure 2-19). SAXS data for thiostannate capped PbS NCs is shown in Figure 2-19 and linearized to extrapolate to q=0. Finally, a Zimm plot is constructed based on the equation:

$$\frac{1}{MW_{NC}c} = \frac{K}{I(0,c)} - 2A_2$$

and A_2 is calculated from the y-intercept. The B_2 values for five sizes of PbS NCs are tabulated in Table 2-1 along with the second virial coefficient of pure hard spheres with diameter, d:

$$B_2^{HS} = \frac{2\pi}{3} d^3$$

and the normalized second virial coefficient, b_2:

$$b_2 = \frac{B_2}{B_2^{HS}}$$

which puts the measured B_2 values in context relative to an identically sized sphere with purely hard sphere interactions.

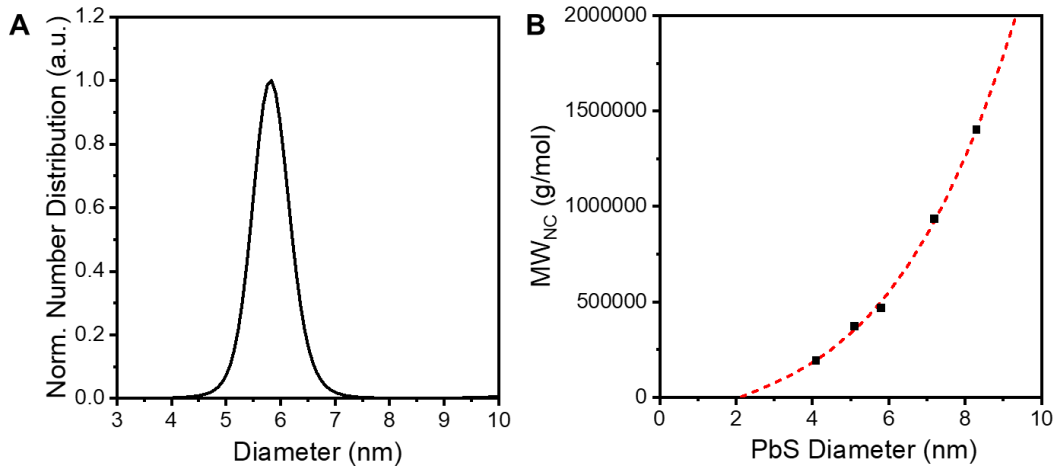

Figure 2-18: Nanocrystal molecular weight calculation.

(**A**) Normalized number distribution modeled from SAXS of 5.8 nm PbS-OA NCs in methylcyclohexane. (**B**) PbS NC molecular weights calculated for five NC sizes. Data follow a cubic polynomial trend (dashed red line) expected for increasing NC volume.

The results from Zimm analysis of PbS-Sn_2S_6 NCs show near-zero B_2 values with slightly negative magnitudes across the entire size range. Put in context with the magnitudes of equivalent hard sphere NCs (B_2^{HS}), the obtained B_2 values do not agree with expectations for an expected repulsive system with charge stabilization and show no size dependence. The reason for this difference is that the fitted q-range of the SAXS data does not contain structural information on the interparticle potential, and the final B_2 values are expected to be ~0. Close examination of the initial SAXS data (Figure 2-19A) reveals three regions of behavior in the Guinier region: 1) q ~ 0.06-0.02 $Å^{-1}$ with decreasing intensity towards q=0, 2) q ~ 0.02-0.04 $Å^{-1}$ with structural correlation peaks, and 3) q ~ 0.04-0.1 $Å^{-1}$ with increasing intensity toward q=0. Zimm analysis requires the use of the third q region and is not able to account for strong interactions between particles like those observed here while it does work well for weakly interacting organic NCs in

non-polar solvents. While this Zimm analysis does not contain any meaningful results for the B_2 values of charges NCs, it does serve as a useful example showcasing the quality and consistency of SAXS data obtained by synchrotron scattering experiments.

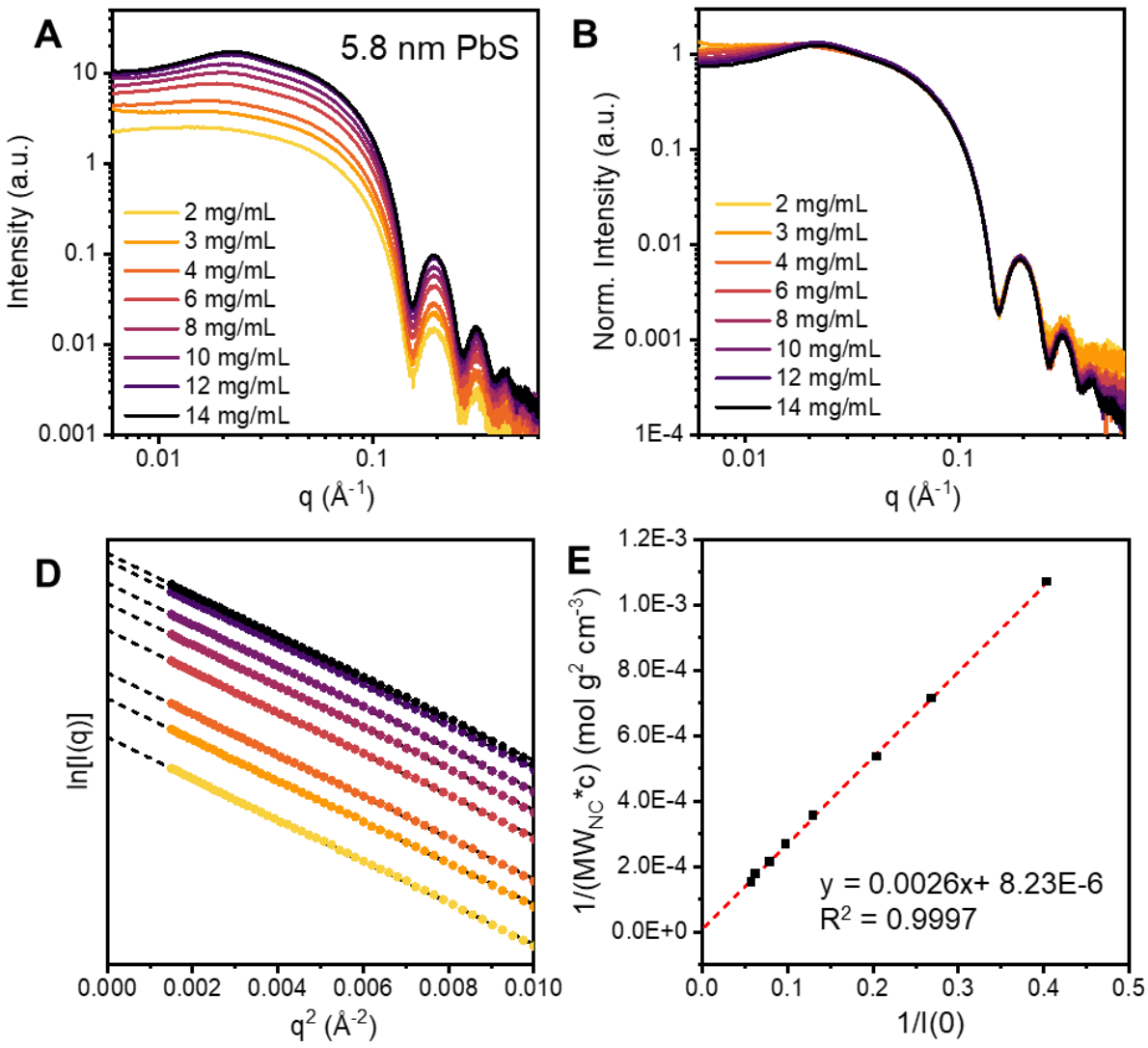

Figure 2-19: Zimm analysis of PbS NC second virial coefficients.

(**A**) Background subtracted SAXS data for a series of 5.8 nm PbS-Sn_2S_6 NCs in NMF. (**B**) Data from panel A normalized by the PbS concentration showing good agreement in sample preparation and measurement across the concentration range. (**C**) Guinier plot of data at q values higher than the solution structure factor (q ~ 0.01-0.04 $Å^{-1}$) with linear fits to extrapolate data to I(0). (**D**) Zimm plot of extrapolated data with excellent linear agreement. Data extends to a y-intercept close to 0, indicating little to no influence of interparticle interactions on the SAXS intensity within this q range.

Table 2-1: Second virial coefficient results for PbS-Sn_2S_6 NCs in NMF by Zimm analysis.

PbS Diameter (nm)	A_2 (mol g^2 cm^{-3})	MW_{NC} (g/mol)	$\boldsymbol{B_2}$ (nm^3)	$\boldsymbol{B_2^{HS}}$ (nm^3)	$\boldsymbol{b_2}$
4.1	-9.34×10^{-6}	191,000	-0.79	144	-0.0019
5.1	-8.27×10^{-6}	373,000	-1.6	278	-0.0056
5.8	-4.12×10^{-6}	467,000	-0.90	409	-0.0022
7.2	-1.31×10^{-6}	933,000	-0.64	782	-0.0008
8.3	-1.27×10^{-6}	1,401,000	-0.95	1,198	-0.0079

I turn now to a second method to determine B_2 using the first q-range described above with q ~ 0.06-0.02 $Å^{-1}$ and a clear decrease in SAXS intensity at higher concentrations corresponding to repulsive interactions. SAXS data for four sizes of PbS-Sn_2S_6 NCs in NMF at multiple concentrations were collected and structure factors were extracted (Figure 2-20). At high q values, the structure factor approaches 1, but the low q region shows first decreasing and then a rapid increase in intensity as q approaches 0. The decrease in structure factor is due to the repulsive interactions to be modeled, but the rapid rise at low q is due to a convolution of multiple factors. First, small agglomeration of NC clusters in solution leads to a scattering tail even though the vast majority of NCs remain as free colloids in the dilute solutions (ϕ<0.002). Second, the total amount of scattering strength relative to background air, glass, and solvent scatting is very small, and any errors in the background subtraction can be magnified. Third, data are collected in glass capillaries, and any misalignment with the capillary center can lead to a slightly different sample path length or glass thickness, much of which is protected against at higher q values with high scattering intensity relative to the background. Together, these factors mean that the rise at q < 0.01 $Å^{-1}$ is real, but less quantitative due to the challenging measurement conditions.

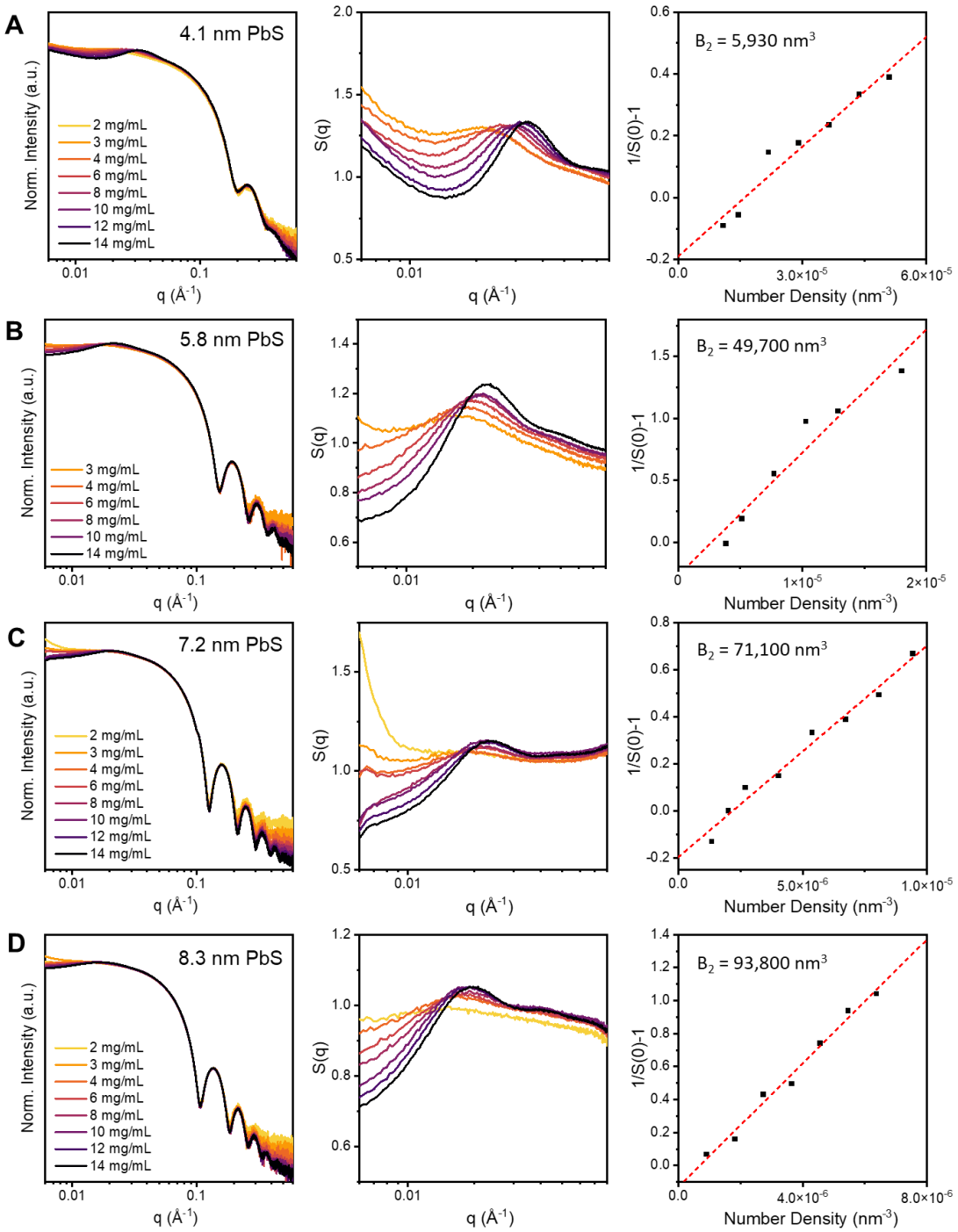

Figure 2-20: Second virial coefficient results for PbS-Sn_2S_6 in NMF by low-q structure factor analysis.

Normalized log-log SAXS (left column) and lin-log structure factor plots (middle column) are shown for NCs with (**A**) 4.1, (**B**) 5.8, (**C**) 7.2, and (**D**) 8.3 nm diameters. Right column shows extracted 1/S(0) against NC number density and extracted B_2 values from the fitted slope.

To extract B_2 from this data, the structure factor is extrapolated to q=0 using a quadratic functional form. Care is taken in the selection of the fitting region to exclude the structure factor peaks and the low q rise in scattering while maintaining the quadratic decrease in intensity. The resulting S(0) values for each concentration are plotted against the NC number density (n) and fitted to the equation:

$$\frac{1}{S(0)} - 1 = 2B_2 n + O(n^2)$$

which emerges from a virial expansion of the osmotic pressure.[28] The resulting linear fits are shown in Figure 2-20 and B_2 values are calculated from the slope.

The measured B_2 values are highly positive (repulsive) and much larger than the purely hard sphere B_2^{HS} values (Table 2-2). Interestingly, the normalized b_2 value is largest for 5.8 nm PbS NCs which are experimentally observed to be highly colloidal and can self-assemble into highly ordered supercrystals. Based on the decreasing surface to volume ratio as the diameter increases, it is expected that attractive vdW forces will begin to outcompete electrostatic repulsion at large sizes, but the smallest 4.1 nm NCs fall out of this trend with the lowest observed b_2 value. This behavior could be related to a NC shape transition at small sizes where PbS NCs lose the small contribution of (100) facets in favor of a continuous (111) NC surface with an octahedral shape. These results showcase the first example where interparticle repulsive interactions are quantified for MCC capped inorganic nanocrystals and prompt interesting questions about the full colloidal behavior of MCC capped PbS NCs including how they can be manipulated in future applications, especially in colloidal to solid phase transformations (e.g., self-assembly, spin-coating).

Table 2-2: Second virial coefficient results for PbS-Sn_2S_6 NCs in NMF by low-q structure factor analysis of SAXS data.

PbS Diameter (nm)	B_2 (nm^3)	B_2^{HS} (nm^3)	b_2
4.1	5,930	144	41
5.8	49,700	409	122
7.2	71,100	782	91
8.3	93,800	1,198	78

2.7. Chapter 2 bibliography

1. Won, Y.-H.; Cho, O.; Kim, T.; Chung, D.-Y.; Kim, T.; Chung, H.; Jang, H.; Lee, J.; Kim, D.; Jang, E. Highly Efficient and Stable InP/ZnSe/ZnS Quantum Dot Light-Emitting Diodes. *Nature* **2019**, *575* (7784), 634–638.
2. Kamath, A.; Schaller, R. D.; Guyot-Sionnest, P. Bright Fluorophores in the Second Near-Infrared Window: HgSe/CdSe Quantum Dots. **2023**.
3. Yang, Z.; Janmohamed, A.; Lan, X.; García de Arquer, F. P.; Voznyy, O.; Yassitepe, E.; Kim, G.-H.; Ning, Z.; Gong, X.; Comin, R.; Sargent, E. H. Colloidal Quantum Dot Photovoltaics Enhanced by Perovskite Shelling. *Nano Lett.* **2015**, *15* (11), 7539–7543.
4. McDonald, S. A.; Konstantatos, G.; Zhang, S.; Cyr, P. W.; Klem, E. J. D.; Levina, L.; Sargent, E. H. Solution-Processed PbS Quantum Dot Infrared Photodetectors and Photovoltaics. *Nature Mater* **2005**, *4* (2), 138–142.
5. Coropceanu, I.; Bawendi, M. G. Core/Shell Quantum Dot Based Luminescent Solar Concentrators with Reduced Reabsorption and Enhanced Efficiency. *Nano Letters* **2014**, *14* (7), 4097–4101.
6. Guyot-Sionnest, P.; Ackerman, M. M.; Tang, X. Colloidal Quantum Dots for Infrared Detection beyond Silicon. *J. Chem. Phys.* **2019**, *151* (6), 060901.
7. Hines, M. A.; Scholes, G. D. Colloidal PbS Nanocrystals with Size-Tunable Near-Infrared Emission: Observation of Post-Synthesis Self-Narrowing of the Particle Size Distribution. *Advanced Materials* **2003**, *15* (21), 1844–1849.
8. Zhang, J.; Crisp, R. W.; Gao, J.; Kroupa, D. M.; Beard, M. C.; Luther, J. M. Synthetic Conditions for High-Accuracy Size Control of PbS Quantum Dots. *J. Phys. Chem. Lett.* **2015**, *6* (10), 1830–1833.

9. Weidman, M. C.; Beck, M. E.; Hoffman, R. S.; Prins, F.; Tisdale, W. A. Monodisperse, Air-Stable PbS Nanocrystals *via* Precursor Stoichiometry Control. *ACS Nano* **2014**, *8* (6), 6363–6371.
10. Hendricks, M. P.; Campos, M. P.; Cleveland, G. T.; Jen-La Plante, I.; Owen, J. S. A Tunable Library of Substituted Thiourea Precursors to Metal Sulfide Nanocrystals. *Science* **2015**, *348* (6240), 1226–1230.
11. Abécassis, B.; Greenberg, M. W.; Bal, V.; McMurtry, B. M.; Campos, M. P.; Guillemeney, L.; Mahler, B.; Prevost, S.; Sharpnack, L.; Hendricks, M. P.; DeRosha, D.; Bennett, E.; Saenz, N.; Peters, B.; Owen, J. S. Persistent Nucleation and Size Dependent Attachment Kinetics Produce Monodisperse PbS Nanocrystals. *Chem. Sci.* **2022**, *13* (17), 4977–4983.
12. Campos, M. P.; De Roo, J.; Greenberg, M. W.; McMurtry, B. M.; Hendricks, M. P.; Bennett, E.; Saenz, N.; Sfeir, M. Y.; Abécassis, B.; Ghose, S. K.; Owen, J. S. Growth Kinetics Determine the Polydispersity and Size of PbS and PbSe Nanocrystals. *Chem. Sci.* **2022**, *13* (16), 4555–4565.
13. van Embden, J.; Chesman, A. S. R.; Jasieniak, J. J. The Heat-Up Synthesis of Colloidal Nanocrystals. *Chem. Mater.* **2015**, *27* (7), 2246–2285.
14. Choi, H.; Ko, J.-H.; Kim, Y.-H.; Jeong, S. Steric-Hindrance-Driven Shape Transition in PbS Quantum Dots: Understanding Size-Dependent Stability. *J. Am. Chem. Soc.* **2013**, *135* (14), 5278–5281.
15. Moreels, I.; Lambert, K.; Smeets, D.; De Muynck, D.; Nollet, T.; Martins, J. C.; Vanhaecke, F.; Vantomme, A.; Delerue, C.; Allan, G.; Hens, Z. Size-Dependent Optical Properties of Colloidal PbS Quantum Dots. *ACS Nano* **2009**, *3* (10), 3023–3030.

16. Kovalenko, M. V.; Scheele, M.; Talapin, D. V. Colloidal Nanocrystals with Molecular Metal Chalcogenide Surface Ligands. *Science* **2009**, *324* (5933), 1417–1420.
17. Kovalenko, M. V.; Bodnarchuk, M. I.; Zaumseil, J.; Lee, J.-S.; Talapin, D. V. Expanding the Chemical Versatility of Colloidal Nanocrystals Capped with Molecular Metal Chalcogenide Ligands. *J. Am. Chem. Soc.* **2010**, *132* (29), 10085–10092.
18. Chen, O.; Chen, X.; Yang, Y.; Lynch, J.; Wu, H.; Zhuang, J.; Cao, Y. C. Synthesis of Metal-Selenide Nanocrystals Using Selenium Dioxide as the Selenium Precursor. *Angew. Chem. Int. Ed.* **2008**, *47* (45), 8638–8641.
19. Morrison, C.; Sun, H.; Yao, Y.; Loomis, R. A.; Buhro, W. E. Methods for the ICP-OES Analysis of Semiconductor Materials. *Chem. Mater.* **2020**, *32* (5), 1760–1768.
20. Protesescu, L.; Nachtegaal, M.; Voznyy, O.; Borovinskaya, O.; Rossini, A. J.; Emsley, L.; Copéret, C.; Günther, D.; Sargent, E. H.; Kovalenko, M. V. Atomistic Description of Thiostannate-Capped CdSe Nanocrystals: Retention of Four-Coordinate SnS4 Motif and Preservation of Cd-Rich Stoichiometry. *J. Am. Chem. Soc.* **2015**, *137* (5), 1862–1874.
21. Heinen, M.; Holmqvist, P.; Banchio, A. J.; Nägele, G. Pair Structure of the Hard-Sphere Yukawa Fluid: An Improved Analytic Method versus Simulations, Rogers-Young Scheme, and Experiment. *The Journal of Chemical Physics* **2011**, *134* (4), 044532.
22. Bass, S. J.; Nathan, W. I.; Meighan, R. M.; Cole, R. H. Dielectric Properties of Alkyl Amides. II. Liquid Dielectric Constant and Loss. *J. Phys. Chem.* **1964**, *68* (3), 509–515.
23. Sengwa, R. J.; Khatri, V.; Sankhla, S. Static Dielectric Constants and Kirkwood Correlation Factor of the Binary Mixtures of N-Methylformamide with Formamide, N,N-Dimethylformamide and N,N-Dimethylacetamide. *J Solution Chem* **2009**, *38* (6), 763–769.

24. McQuarrie, D. A.; Simon, J. D. *Physical Chemistry: A Molecular Approach*; University Science Books: Sausalito, Calif, 1997.
25. Vrij, A.; Tuinier, R. 5 Structure of Concentrated Colloidal Dispersions. In *Fundamentals of Interface and Colloid Science*; Elsevier, 2005; Vol. 4, p 5.1-5.103.
26. George, A.; Wilson, W. W. Predicting Protein Crystallization from a Dilute Solution Property. *Acta Crystallogr D Biol Crystallogr* **1994**, *50* (4), 361–365.
27. Saunders, A. E.; Korgel, B. A. Second Virial Coefficient Measurements of Dilute Gold Nanocrystal Dispersions Using Small-Angle X-Ray Scattering. *J. Phys. Chem. B* **2004**, *108* (43), 16732–16738.
28. Ofosu, C. K.; Kang, J.; Truskett, T. M.; Milliron, D. J. Effective Hard-Sphere Repulsions between Oleate-Capped Colloidal Metal Oxide Nanocrystals. *J. Phys. Chem. Lett.* **2022**, *13* (48), 11323–11329.
29. Zimm, B. H. The Scattering of Light and the Radial Distribution Function of High Polymer Solutions. *The Journal of Chemical Physics* **1948**, *16* (12), 1093–1099.

3. Self-assembly of nanocrystals into strongly electronically coupled all-inorganic supercrystals

3.1. Introduction

Self-assembly of nanocrystals (NCs) into long-range ordered arrays can enable bottom-up design of hierarchically organized functional and multifunctional materials.[1,2] A large body of work has identified conditions for assembly of colloidal NCs into face-centered cubic (fcc) and body-centered cubic (bcc) solids [3,4], multicomponent binary and ternary NC superlattices,[5–8] and quasicrystalline structures.[9,10] These approaches used NCs with surfaces functionalized by long hydrocarbon chains or surface-tethered DNA strands that supported colloidal stability but also separated NCs with electrically insulating barriers, at least 1 to 2 nm in thickness. These barriers lead to poor electronic conductivity of ordered NC assemblies and constrain their prospects for practical applications. Some collective effects can develop through distant coupling of plasmonic excitations[11] or magnetic dipoles,[12] but free electron movement is needed to develop conduction bands. The combination of translational symmetry and strong electronic coupling holds the promise of enabling a general platform for the construction of new functional materials from the available library of NCs.

Strong coupling between NCs can be achieved by using very compact (typically inorganic) surface ligands. For example, thin films of CdSe NCs capped with $In_2Se_4^{2-}$ surface ligands can develop bandlike electronic transport.[13] These ligands add charge to the NC surface,

and NCs act as electrostatically stabilized colloids in polar solvents. However, NCs with such ligands failed to form ordered superstructures because the van der Waals attractive forces arising between touching NCs are too strong and arrest the system as a gel or glass.[14] An alternative approach to building strongly electronically coupled NC solids is to remove the native insulating organic ligands after assembly,[15,16] which sometimes results in the oriented attachment of NCs.[16–18] However, irreversible oriented attachment cannot produce large, ordered SC domains because structural defects accumulate. This problem is inherent to any assembly process that lacks a self-healing pathway enabled by microreversibility.[19,20]

This chapter describes a new class of all-inorganic super-crystalline (SC) materials that combine long-range order with strong electronic coupling (Figure 3-1). I first describe the reversible self-assembly process to synthesize strongly coupled supercrystals using metallic and semiconducting NC building blocks such as Au, Pt, Ni, PbS and PbSe NCs with small and conductive metal chalcogenide complex (MCC) ligands (such as $Sn_2S_6^{4-}$, $Sn_2Se_6^{4-}$, AsS_4^{3-}, and GeS_4^{4-}). Second, I examine the internal crystal structures of Au and PbS supercrystals. I then provide an analysis of the accumulation of negatively charged anionic ligands near the surfaces of nanocrystals with high dielectric constants which provides an additional repulsive interparticle force and enables enough microreversibility for crystallization to proceed. Next, I investigate the nucleation mechanism of supercrystals which either occurs via a one-step mechanism with solid supercrystals growing directly from "gaseous" colloidal NCs, or a two-step mechanism where supercrystals nucleate from a "colloidal liquid" intermediate phase. Kinetic studies by in situ measurements of supercrystal nucleation and growth provide direct evidence of both one and two-step nucleation behavior for PbS NCs. The supercrystals formed from PbS NCs are found to

exhibit crystallographic alignment of the PbS atomic rock salt lattices across the entire supercrystal due to the highly faceted surfaces of PbS NCs.

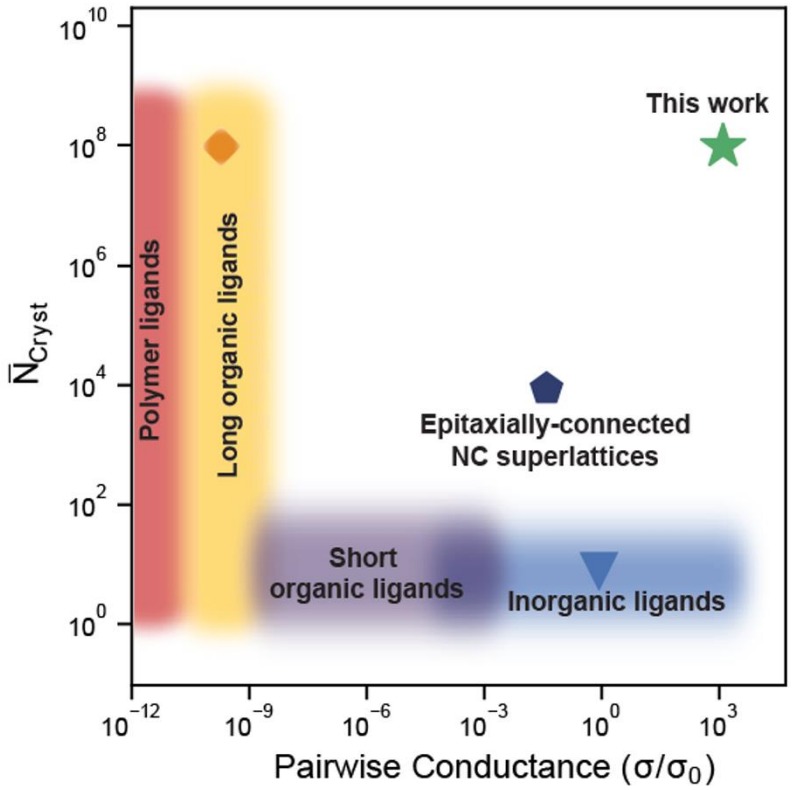

Figure 3-1: Comparison of long-range order and strong coupling across nanocrystal assemblies.

As a measure of electronic coupling in different ordered and disordered structures, we used the interparticle conductance ($s^*=s/s_0$) normalized by the conductance quantum ($s_0=2e^2/h$),where e is the electron charge and h is Plank's constant. As a measure of the ordering, we took the average number of particles in a crystalline domain. The data points indicated are as follows: red diamond, superlattices of DDT-capped Ag NCs;[21] light blue inverted triangle, film of inorganically capped HgTe NCs;[22] and dark blue pentagon, epitaxially connected PbSe superlattice by oriented attachment.[17] Green star indicates data from the present work.

3.2. Synthesis and reversible self-assembly of all-inorganic supercrystals from charged colloidal nanocrystals

The most critical parameters in the synthesis of supercrystals from charged NCs are the quality of the NC feedstock solutions (e.g., size and monodispersity) and the preparation of their

surface chemistry. The synthesis of highly monodisperse NCs with native organic ligands is detailed in Chapter 2 along with details on the precise ligand exchange with charged MCC ligands into polar solvents. The colloidal stability of charged NCs solutions is a determining factor in their ability to self-assemble into supercrystals, and any clear evidence of interparticle attraction by SAXS, observed as an increased scattering tail at low angles in the Guinier region (see Chapter 2.4), has resulted in amorphous solids without the microreversibility needed to find the lowest energy state of a densely packed crystal. Charged NCs are self-assembled into SCs through a controlled flocculation with multivalent anionic salts and either alkali metals, NH_4^+, or $N_2H_5^+$ serving as counterions in polar solvents such as hydrazine and N-methylformamide (Figure 3-2). Faceted three-dimensional SCs of 5 nm Au NCs with $(N_2H_5^+)_4Sn_2S_6$ surface ligands (Figure 3-3A,B) showed micrometer-size domains containing ~10^8 NCs. The MCC ions remained in the superlattice and separated the Au NCs by ~0.3 nm. The small- and wide-angle X-ray scattering (SAXS and WAXS) patterns of macroscopic samples showed two sets of face centered cubic (fcc) reflections, from the atomic planes inside individual NCs at the momentum transfers $q > 1$ Å^{-1} and from the SC planes at $q < 1$ Å^{-1} (Figure 3-3C and D). These structures formed spontaneously upon addition of $K_4Sn_2S_6$ to colloidal solutions of Au NCs with $Sn_2S_6^{4-}$ surface ligands in hydrazine. Interestingly, the addition of 1:1 electrolytes such as NaCl precipitated amorphous aggregates typical for irreversible binding of NCs (Figure 3-4), as had been seen with many previous studies of electrostatically stabilized NC colloids.[14] An additional remarkable observation was that NCs of materials with high dielectric constant (ε_{NC}), such as metals ($\varepsilon_{NC} \to \infty$), PbS ($\varepsilon_{NC} = 170$), and PbSe ($\varepsilon_{NC} = 220$) readily formed SCs (Figure 3-3E-H), whereas any NCs with $\varepsilon_{NC} < 20$ (CdSe, InAs, and Fe_2O_3) formed gels or glasses.

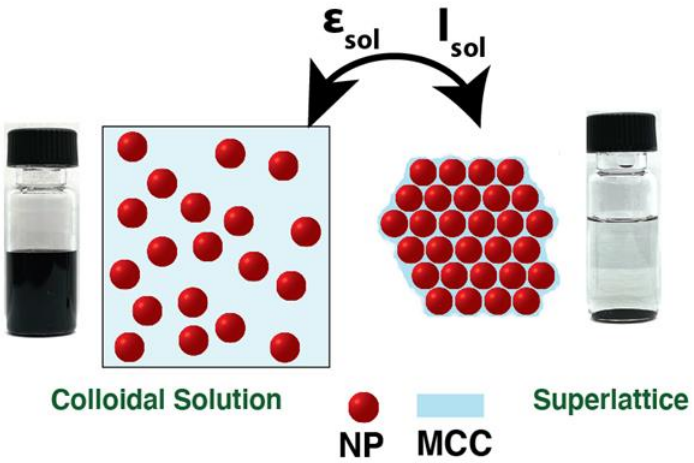

Figure 3-2: Schematic of electrostatic self-assembly.

Schematic diagram and photo of a colloidal solution of Au-Sn_2S_6 NCs in hydrazine (left). After flocculation by addition of $(N_2H_5^+)_4Sn_2S_6$ ions to increase the ionic strength, solid supercrystals form and sink to the bottom of the vial (right).

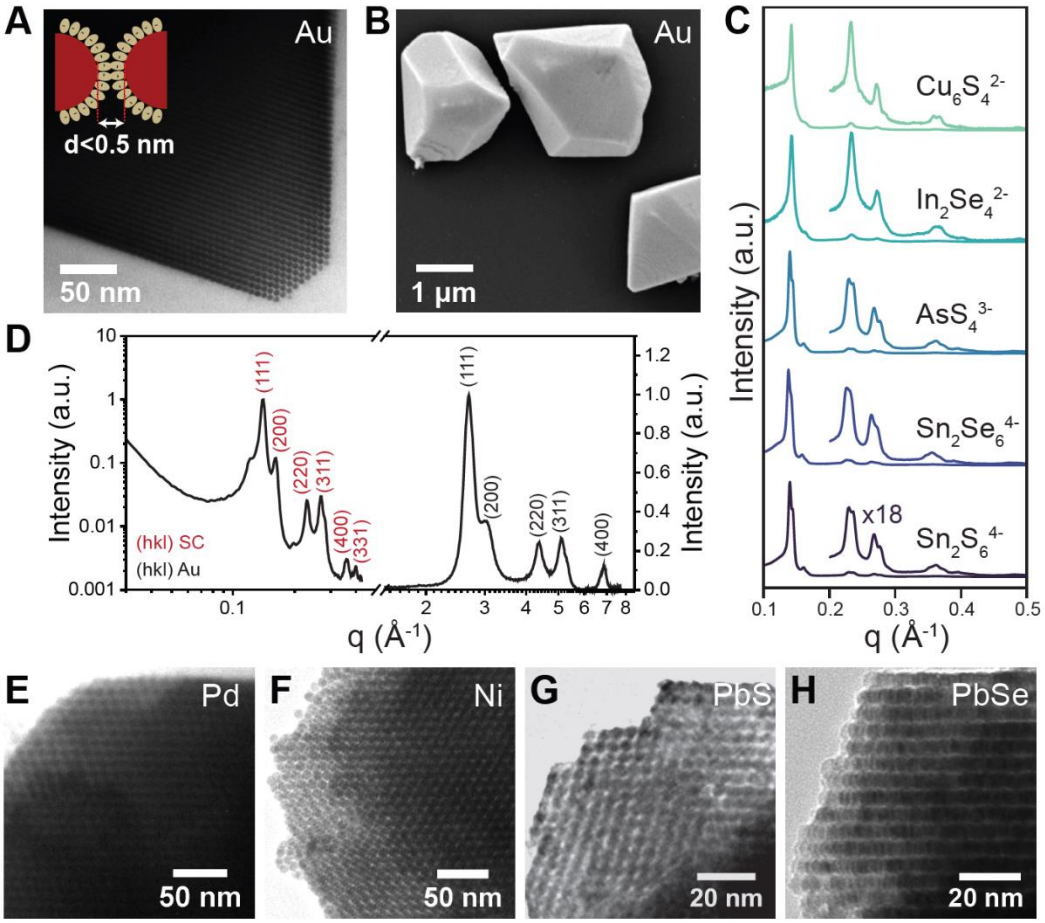

Figure 3-3: Compositional diversity of all-inorganic NC assemblies.

(**A**) TEM and (**B**) SEM micrographs of supercrystals assembled from 3.8-nm Au NCs with $(N_2H_5)_4Sn_2S_6$ surface ligands. (**C**) SAXS patterns for self-assembly of a population of 5 nm Au NCs with different MCC ligands, yielding crystalline superlattices in each case (inset: vertically magnified view of the SAXS pattern after the 111 peak). (**D**) SAXS and WAXS patterns of supercrystals assembled from Au NCs with $(N_2H_5)_4Sn_2S_6$ ligands showing fcc crystalline order at both the supercrystal and atomic length scales. Data have been normalized to the 111 peaks. (**E to H**) TEM micrographs of different all-inorganic NC assemblies, showing ordered domains of 9 nm Pd, 9 nm Ni, 5 nm PbS, and 6 nm PbSe NCs with MCC ligands, respectively.

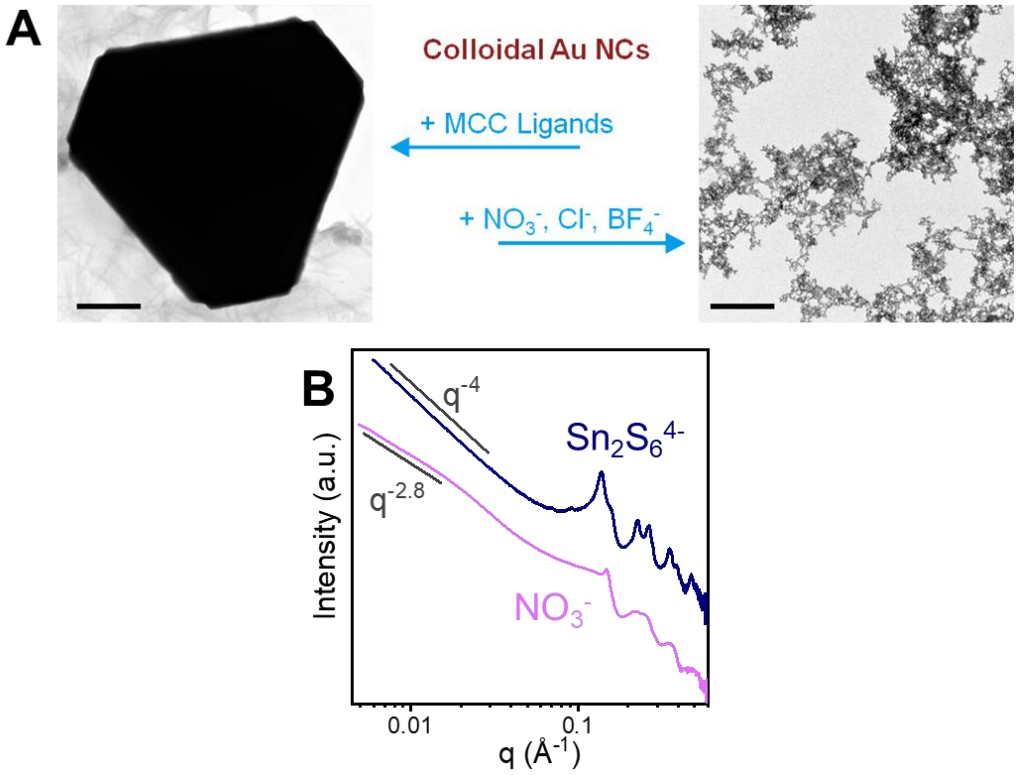

Figure 3-4: Flocculating salt valency controls NC long-range order.

(**A**) TEM images showing assembled Au NCs with MCC ligands in hydrazine after addition of excess MCC ligands (left) and fractal aggregation after addition of 1:1 electrolytes (right). Scale bars are 500 nm. (**B**) Log-log scale SAXS comparing the Porod's Law scaling at low q for Au-Sn_2S_6 flocculated with $NaNO_3$ and with $(N_2H_5)_4Sn_2S_6$.

The assembly of MCC capped NCs is completely reversible with no observable effect on the individual NCs. After self-assembly and removal of trace solvent though washing steps, the SCs dissolve completely into their individual NC building blocks when placed into pure NMF or hydrazine (Figure 3-5). NCs do not undergo necking or sintering even after low-temperature transport studies on films of Au NCs. Size analysis of PbS and Au NCs after redissolution shows no change in the average NC size and SAXS of the solutions show no change in colloidal stability relative to the initial stock solutions.

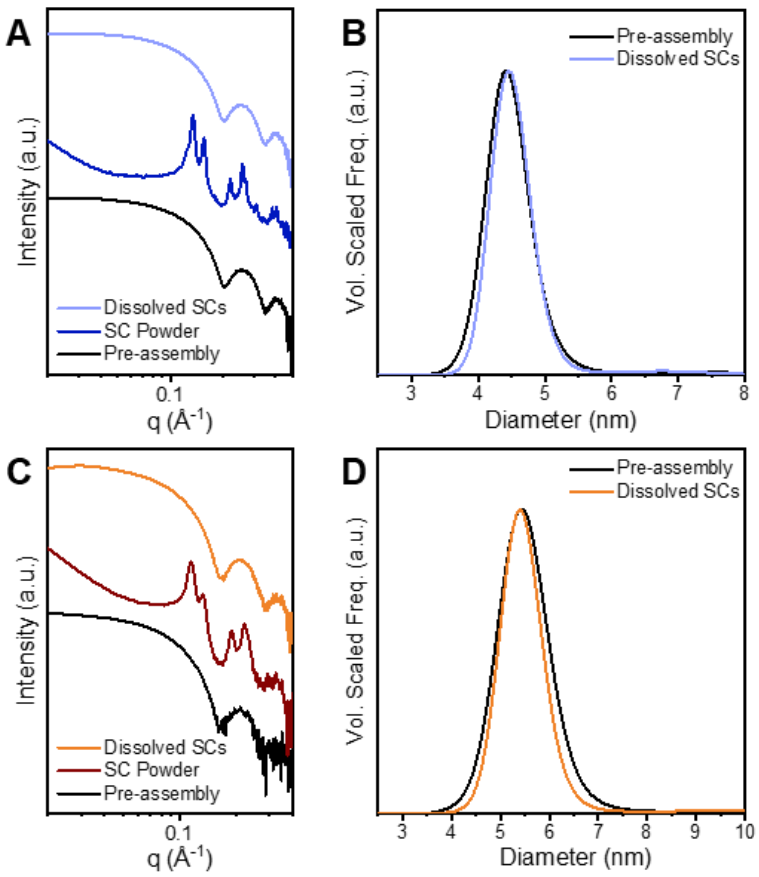

Figure 3-5: Reversibility in NC self-assembly.

(**A,C**) SAXS patterns of 4.5 nm Au-Sn_2S_6 NCs in hydrazine and 5.5 nm PbS-Sn_2S_6 NCs in NMF before assembly, as SC powders, and after redissolution of the superlattices in hydrazine or NMF, respectively. (**B,D**) Extracted size distributions of Au and PbS NCs before assembly and after redissolution into hydrazine or NMF, respectively.

3.3. Crystal structures of all-inorganic supercrystals

The most common crystal structure observed in the self-assembly of MCC capped NCs is the most densely packed fcc phase (Figure 3-6). Based on purely hard sphere interactions, higher density phases are the most energetically favorable due to a maximal increase in the system entropy. While most NCs have significant deviations from a hard sphere model due to soft, ~2 nm organic ligands that contribute significantly to the total particle volume, MCC ligands are relatively compact (~0.5 nm) and can strongly bind to the NC surface. The interparticle

interactions between MCC capped NCs can be complicated by electrostatic double layers and long Debye lengths in solutions. However, self-assembly occurs under conditions of high ionic strength where electrostatic interactions are largely removed by screening effects and the system approaches a purely hard sphere interaction with only a short-range attractive potential remaining.

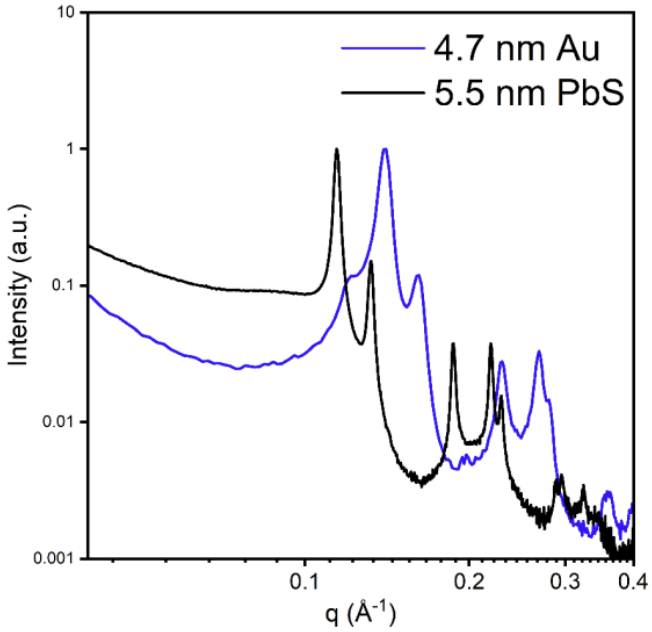

Figure 3-6: PbS and Au fcc supercrystal comparison.

Normalized SAXS of supercrystals assembled from 5.5 nm PbS-Sn_2S_6 NCs in NMF and 4.7 nm Au-Sn_2S_6 NCs in hydrazine. Both structures show an fcc crystal structure and are measured directly inside the self-assembly matrix with excess MCC ligands and solvent present.

The volume fraction of the NC cores within supercrystals is determined by the ligand length and total amount of lattice contraction. When NCs first assemble into an fcc crystal in solution, the lattice is relatively loose with surface-to-surface distances of ~1.4 nm (Figure 3-7). After washing the supercrystals with acetonitrile to isolate them as a powder, the lattice contracts to ~0.5 nm between NC surfaces as excess ligands and solvent are removed while maintaining the fcc crystal structure. Thiostannate ligand molecules are ~0.5 nm in length which would

account for one bridging ligand between NCs in dried supercrystals. This analysis assumes that NCs are perfect spheres, however, and it is known that PbS NCs with diameters above ~4 nm transition from octahedral to truncated octahedron shapes with exposed (100) and (111) surface facets.

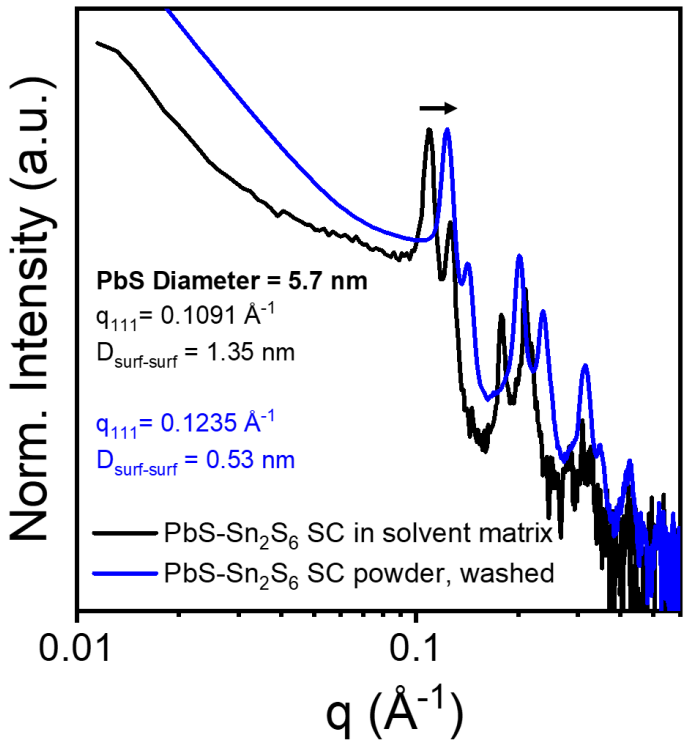

Figure 3-7: Lattice contraction of PbS NC supercrystals.

Log-log normalized SAXS of 5.7 nm PbS-Sn_2S_6 supercrystals measured inside a flocculating solution of 150 mM K_3AsS_4 in 70:30 NMF:ACN (black line) and measured as a granular powder after washing with ACN (blue line). The fcc crystal structure is maintained through the washing and drying steps leading to lattice contraction. Surface-to-surface distances are calculated assuming spherical NCs with PbS NC core sizes determined via SAXS fitting to the same sample with oleic acid ligands prior to ligand exchange with $K_4Sn_2S_6$ ligands.

Interestingly, I find that supercrystals assembled from 5.7 nm PbS-Sn_2S_6 NCs have an additional degree of order across the supercrystal with crystallographic alignment between neighboring PbS rock salt atomic lattices (see section 3.7). PbS NCs have been known to form multiple crystal structures with organic surface ligands due to a facet and oxidation dependent

binding of oleic acid ligands,[23] but the exact structure of MCC ligands surrounding PbS nanocrystals in not known. Analysis of the supercrystal structure reveals that the atomic PbS lattices are co-aligned along the [110] zone axis of the fcc supercrystal. Within the fcc unit cell, the closest approach between neighboring NCs is always facet edges, with a large prevalence of both tetrahedral and octahedral interstitial sites surrounded by (111) and (100) facets, respectively. The atomic alignment likely occurs during the initial assembly of NCs into loose fcc structures to keep the charged NC surfaces as far away as possible while maximizing the overall packing density of the supercrystal.

Au SC crystals structures in hydrazine behaved similarly to PbS SCs in NMF, but multiple additional non-fcc phases were also observed at smaller Au NC sizes (< 4.5 nm). Upon complete flocculation after rapid addition of MCC ligands (>75 mM $Sn_2S_6^{4-}$), predominantly fcc structure factors are observed for Au NCs in hydrazine (
A). However, at low ligand concentrations (e.g., 25 mM $Sn_2S_6^{4-}$), partial flocculation can result in complex structure factors resembling topologically close-packed Frank-Kasper phases.[24] Non-fcc phases are likely metastable structures enabled by the additional microreversibility at low quench depths. For the SCs assembled at 25 mM in
A, ~70% of the Au NCs are estimated to remain colloidal multiple days after the initial assembly based on the supernatant scattering intensity demonstrating the high degree of microreversibility in the system.

Slow flocculation of Au NCs can also lead to complex structure factors of the resulting supercrystals. In one example, 4.5 nm Au-Sn_2S_6 NCs in hydrazine were slowly flocculated with three separate anions with decreasing valency: thiostannate, arsenic sulfide, and sulfide (

B). All three samples show similar behavior after all NCs are precipitated with an array of >5 sharp peaks near the (111) and (200) diffraction peaks expected for fcc supercrystals. Two possible explanations for these structures are hypothesized. 1) When the ionic strength is increased slowly, NCs are size-selectively self-assembled with the largest NCs precipitating first as fcc SCs due to stronger attractive vdW forces and a lower critical flocculation concentration. The final powder contains a polydisperse mixture of micron sized fcc supercrystals with varying lattice constants, each with a lower average internal strain due to the higher monodispersity of NCs inside each supercrystal. 2) At low ligand concentrations and slow assembly, NCs find equilibrium non-fcc structures which grow as the colloid is depleted, but when a critical salt concentration is reached, kinetic fcc products begin to dominate. The final powder would contain a complex mixture of multiple crystalline phases and/or lattice constants leading to the complex structure factor observed in experiments. While the exact sample description is not known, I suggest that size-selective self-assembly is the more likely conclusion due to the rarity of non-fcc phases observed among Au NC assemblies.

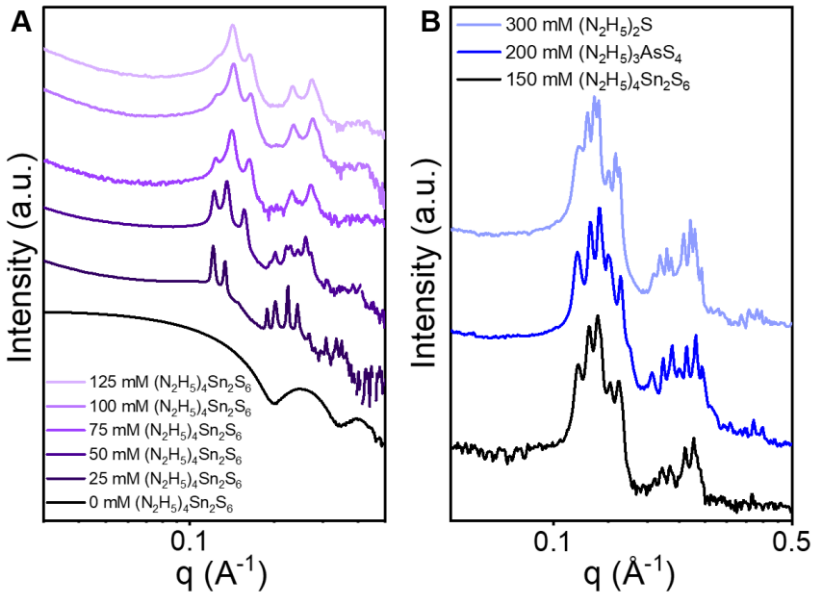

Figure 3-8: Complex structure factors in Au NC supercrystals.

(**A**) SAXS of 4.2 nm Au-Sn_2S_6 NCs in hydrazine. SAXS data are shown at a series of excess ligand concentrations and collected by measuring the solids at the bottom of a glass capillary containing a combination of free colloidal NCs in solution and solid supercrystals. (**B**) SAXS of 4.5 nm Au-Sn_2S_6 NCs in hydrazine assembled slowly by addition of three different MCC ligands. In each case, the ligand concentration is increased in steps of 25-50 mM and allowed to equilibrate for ~15 min before increasing the ligand concentration.

While the majority phase of Au SCs is fcc, a small fraction of hexagonal close packed (hcp) SCs have also been observed by SAXS and TEM for small Au NC sizes (Figure 3-9). The packing fraction of fcc and hcp structures are identical for hard spheres (ϕ=0.74), but theoretical calculations have shown that fcc phases dominate in experiment due to a lower interfacial free energy which makes it the preferred phase for nucleation.[25] Small diffractions peaks corresponding to the (100) and (110) lattice planes are often observable for Au SCs which are allowed for hcp crystals but not fcc. Large Au NCs (~5 nm and above) do not show any non-fcc phase behavior due to the large Hamaker constant of Au NCs (~1.6 eV) which rapidly increases the attractive vdW forces with increasing radius and accelerates the agglomeration process during self-assembly. In

fact, the vdW size scaling is so dominant that >6 nm Au NCs are difficult to assemble into fcc SCs with high yields or crystallinity from hydrazine colloids.

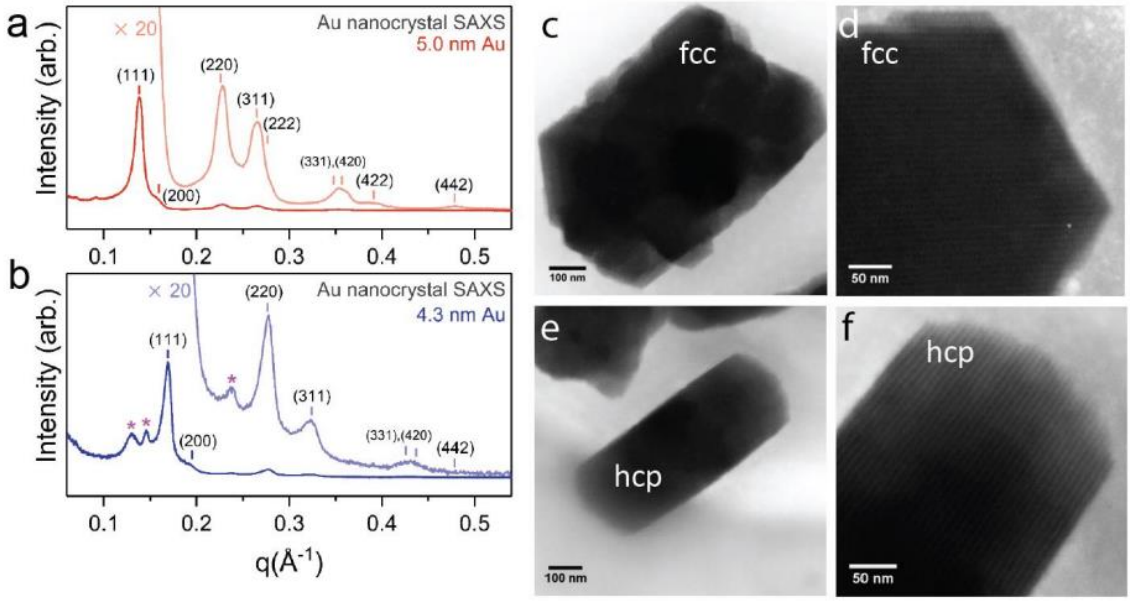

Figure 3-9: Supercrystal fcc/hcp phase coexistence.

(**a**) SAXS pattern of a typical Au-Sn_2S_6 assembly showing nearly phase-pure fcc solid. (**b**) SAXS pattern of a Au assembly with a mixture of fcc and hcp phases. Additional hcp peaks are indicated by an asterisk. (**c-f**) Representative TEM images of fcc and hcp superlattices.

3.4. Charge accumulation around highly polarizable nanocrystals

Self-assembly of metallic (Au, Pd, and Ni) and semiconducting (PbS and PbSe) NCs results in large fcc supercrystals, but flocculation of CdSe NCs results in only fractal or compact aggregates with no observable long-range order (Figure 3-10). The CdSe NC size does not change the outcome during agglomeration despite the change in the interparticle vdW attractive forces. The outlying factor for CdSe NCs is their low dielectric constant ($\varepsilon_{CdSe} = 9.7$) compared to those of the lead chalcogenides with anomalously high static dielectric constants (ε_{PbS}=190, ε_{PbSe}=280) among II-VI semiconductors.[26] In a dense matrix of MCC ligands, highly polarizable NCs are predicted to form image charges at the NC surface which can lead to increased charge

accumulation around the NC. The presence of these charge accumulations and restructuring of multivalent anions is a key factor in the ability of NCs to maintain microreversibility throughout the agglomeration process into supercrystals.

Molecular dynamics (MD) simulations showed that multivalent ions formed a dense layer near the NC surface for metallic NCs ($\varepsilon_{NC} \rightarrow \infty$), whereas typical dielectric NCs (ε_{NC}<20) have only loosely associated counterions with the NC surface (Figure 3-11A). Radial density profiles were calculated for anions and revealed that as ε_{NC} increased, the anions accumulated near the NC surface beyond one full monolayer (Figure 3-11B). The driving force resulted from the dielectric mismatch between the NCs and the surrounding medium.[27] This mismatch induced polarization, which created an attraction between the anions and the image charges inside the NCs.[28] As the anion valency is decreased, the surface induced charges were reduced, which led to loose packing of the condensed anions (Figure 3-11C).

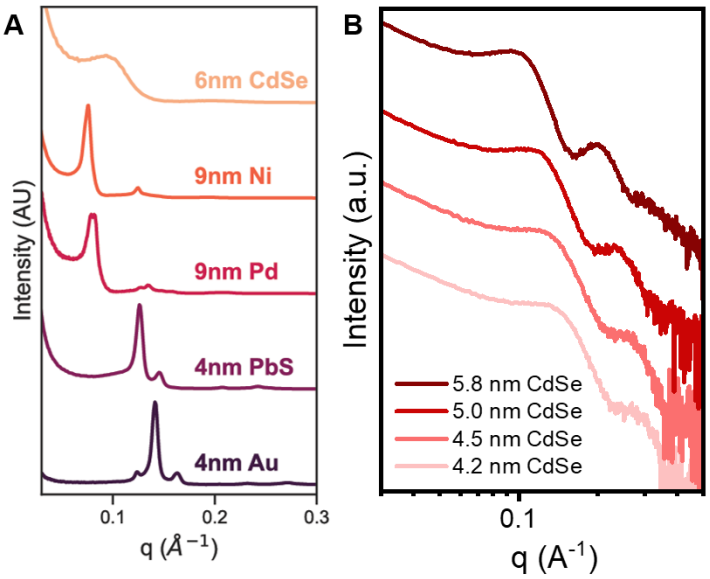

Figure 3-10: NC material composition dependent self-assembly.

(**A**) Linear plots of SAXS patterns with NCs of different compositions and sizes flocculated by MCC ligands showing crystalline assembly in all cases except for CdSe. (**B**) Log-log SAXS patterns of four sizes of CdSe NCs with $K_4Sn_2S_6$ ligands flocculated from NMF solutions using similar methods to the successful self-assembly of PbS NCs, but only compact aggregates are observed for CdSe NC solids.

Direct chemical analysis data supported the theory of increased anion accumulation around high dielectric materials. ICP-OES analysis of the MCC ligand grafting densities revealed ~40% higher grafting density around PbS NCs than similarly sized CdSe NCs (Figure 3-12A). Ligand grafting is calculated based purely on the metal (M=Pb, Cd) content of digested nanocrystals assuming a metal to chalcogenide ratio of 1:1 and spherical NC shapes. PbS NCs also exhibit a slightly higher negative zeta potential (and therefore surface charge) in agreement with elemental analysis showing increased anion condensation and consistent with our model of high ε_{NC} enabling self-assembly due to increased ligand coverage.

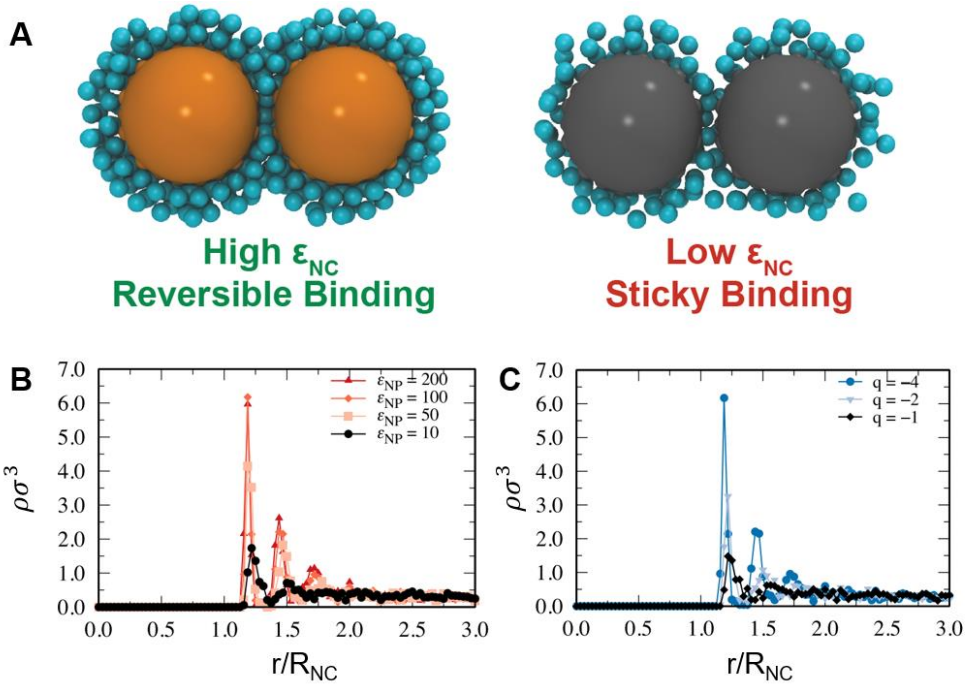

Figure 3-11: Charge accumulation at high dielectric NC surfaces.

(**A**) Qualitative difference in interactions of NCs with high (ε_{NC}= 200) and low (ε_{NC}= 10) dielectric constant, with multivalent ions resulting in reversible and sticky NC binding, respectively. (**B**) Radial charge density profiles of the anions surrounding a NC for different NC dielectric constants at a fixed distance of d/(2R_{NC})=1.1. (**C**) Radial charge density profiles of the anions surrounding NCs for different anion valences, q, at a fixed distance of d/(2R_{NC})=1.1.

A

ICP-OES Analysis

Sample in NMF	MCC grafting density (nm^{-2})
4.4 nm PbS-$Sn_2S_6^{4-}$	1.3
4.5 nm zb-CdSe-$Sn_2S_6^{4-}$	0.84

Sample in NMF	MCC grafting density (nm^{-2})
5.7 nm PbS-$Sn_2S_6^{4-}$	1.2
5.5 nm zb-CdSe-$Sn_2S_6^{4-}$	0.94
5.8 nm zb-CdSe-$Sn_2S_6^{4-}$	0.83

B

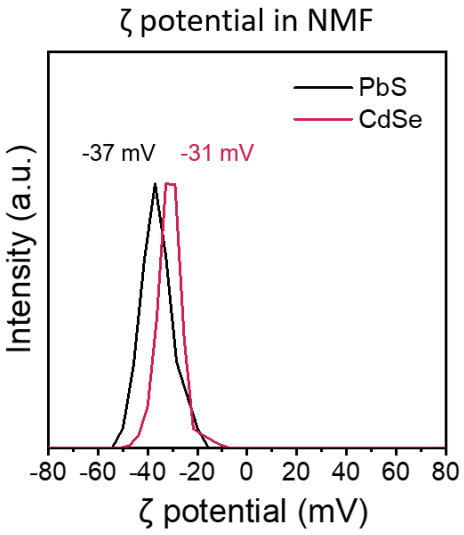

Figure 3-12: Semiconductor NC charge density of elemental analysis.

(**A**) Elemental analysis by ICP-OES of PbS and CdSe NC samples stabilized by $K_4Sn_2S_6$ in N-methylformamide. (**B**) ζ-potential measurements of 5.7 nm PbS and 5.5 nm CdSe with identical $K_4Sn_2S_6$ in N-methylformamide.

3.5. Short-range interparticle attraction leads to triple-phase coexistence of colloidal NC gas, liquid, and solid phases

The exact form of pair potentials for colloidal NCs smaller than 10 nm is generally not known and cannot be easily extracted from available experimental data [29], but Derjaguin-Landau-Verwey-Overbeek (DLVO) theory can serve as the minimal framework accounting for three major components – van der Waals (vdW) attraction, electrostatic repulsion, and an additional steep short-range repulsion at hard contact of NC cores.[30] For a broad range of input parameters, such as surface charge and Hamaker constant, the competition between vdW attraction and electrostatic repulsion results in a narrow (< 1 nm width) potential well with depth larger than 5 k_BT, where k_B is the Boltzmann constant and T is temperature (Figure 3-13A). According to the Noro-Frenkel extended law of corresponding states, the equilibrium phase diagram of systems with short-range attraction, including MCC capped NCs, can be represented

by particles interacting through square-well potentials (Figure 3-13C, inset) with depth u_0 and width $2\lambda R$, where R is the particle radius.[33] For $\lambda < 0.2$, regardless of the exact well shape, the phase diagram consists of two equilibrium phases, a colloidal fluid and a solid, with a "hidden" binodal curve separating two metastable fluid phases (Figure 3-13B).[32,34] Haxton *et al*. modeled the dynamics of a colloidal fluid as function of u_0 and λ (Figure 3-13C) and mapped regions with high probability to form crystals (Regions I and II), metastable fluids with a prohibitively slow nucleation rate (Region III), kinetically frozen metastable gels (Region IV), and a stable liquid phase (Region V).

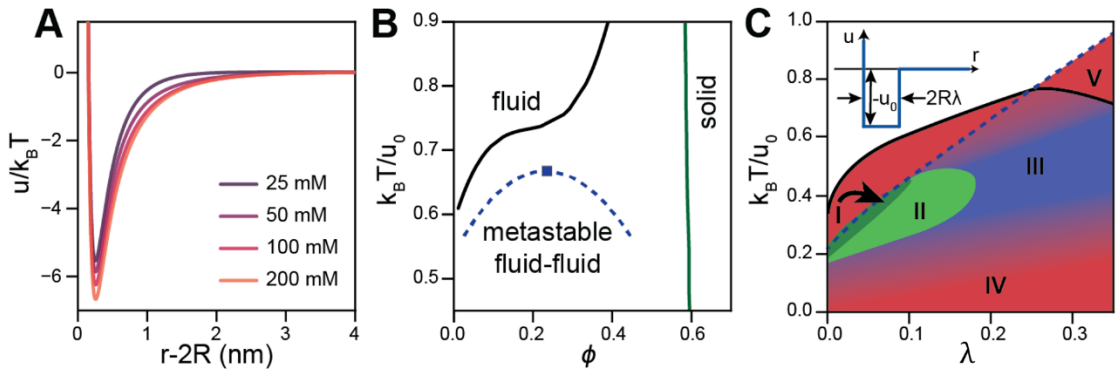

Figure 3-13: Modeling interactions and phase equilibria of charge-stabilized colloidal nanocrystals.

(**A**) Estimated pair potential for 4.5 nm Au NCs in the presence of different concentrations of 1:3 electrolyte. (**B**) Phase diagram for a colloid with a square-well attractive potential with $\lambda = 0.18$. Solid square shows the metastable fluid-fluid critical point. Data were taken from references [31] and [32]. (**C**) Probability of supercrystal nucleation represented by color gradients (green indicates high; blue, intermediate; and red,low) as a function of u_0 and λ of a square-well potential for a colloid with volume fraction of $\phi = 0.1$. The diagram highlights regions corresponding to (I) one-step nucleation, (II) two-step nucleation, (III) coexistence of two metastable fluids with a slow nucleation rate, (IV) gel formation, and (V) a thermodynamically stable colloidal fluid. The dashed blue curve is the metastable fluid-fluid binodal curve, and the solid black curve is the thermodynamic boundary for stability of an fcc crystal. Inset: a square-well potential determined by the depth (u_0) and range of the attraction (λ). Data were taken from reference [31].

Although exact parameters of NC pair potentials may be difficult to access, the appearance, evolution, and the final state of NC colloid offers insights to its location within the

phase diagram. In experiments, the formation of SCs was often preceded by separation of the NC colloid into dense and dilute fluid phases (Figure 3-14A). Such behavior was reported for polymethylmethacrylate (PMMA) spheres[35] and globular proteins[36] but not for inorganic NCs. For Au NCs, optical studies showed that the dense fluid was highly metastable and converted into SCs within seconds, but for PbS NCs, the dilute and dense fluid phases, both with no long-range order, could coexist for many hours, followed by the slow formation of fcc SCs from the dense fluid phase. The dense fluid phase exhibited a short-range structure factor (Figure 3-15) resulting from interparticle correlations at high concentration, similar to previous reports of large PMMA spheres.[32] Such triple-phase coexistence of two metastable colloidal fluids and SCs confirmed the presence of a fluid-fluid binodal curve and further supported that charge-stabilized NC colloids followed the predictions for spheres with short-range attractive potentials.

The metastable binodal curve in the colloidal phase diagram includes a fluid-fluid critical point (Figure 3-13B). Ten Wolde and Frenkel suggested that critical density fluctuations in the vicinity of this critical point lower the activation barrier for crystal nucleation.[34] The SC nucleation can proceed along two different pathways (Figure 3-13C).[31,34] In a narrow window of parameters very close to the binodal curve, classical one-step nucleation (Region I) is predicted to be the main pathway to a crystalline state. Indeed, in situ SAXS studies showed that a gentle increase of $(N_2H_5)_4Sn_2S_6$ concentration in hydrazine up to ~50 mM induced a rapid nucleation of 4.6 nm Au NCs into SCs, which grew at the expense of the free colloid (Figure 3-14C). Photographs of the Au NC solution immediately after flocculation also confirm the rapid nucleation of 4.6 nm Au NCs into SCs, which grew at the expense of the free colloid (Figure 3-14C). Photographs of the Au NC solution immediately after flocculation also confirm the rapid transition of colloidal NCs to solids with no observable fluid intermediate state (Figure 3-16).

nucleation of 4.6 nm Au NCs into SCs, which grew at the expense of the free colloid (Figure 3-14C). Photographs of the Au NC solution immediately after flocculation also confirm the rapid transition of colloidal NCs to solids with no observable fluid intermediate state (Figure 3-16).

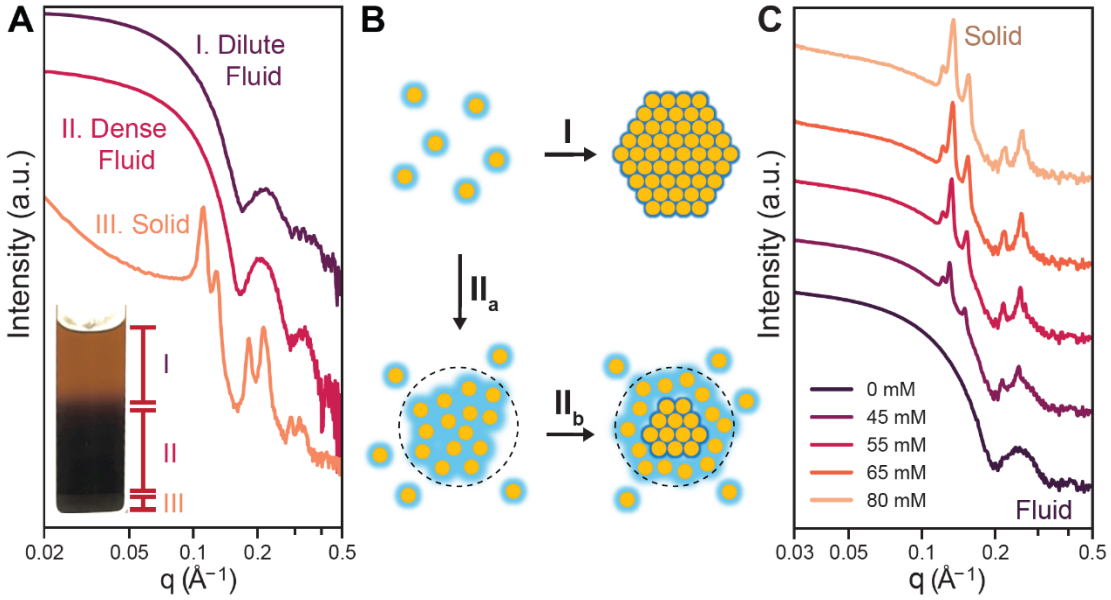

Figure 3-14: Triple-phase coexistence and nucleation in charge-stabilized NC colloids.

(**A**) Homogeneous colloidal solutions of 5.5 nm PbS NCs capped with $Sn_2S_6^{4-}$ ligands in NMF spontaneously form three phases upon addition of acetonitrile. SAXS data show three separate phases of dilute fluid, dense fluid, and fcc solid supercrystals. Inset: photograph of 5.5 nm PbS NC colloid showing the coexistence of three phases. (**B**) Schematic representation of one-step nucleation (I) and two-step nucleation (II_a and II_b) of supercrystals; phase separation precedes crystallization in the latter case. (**C**) In situ SAXS data for one-step nucleation of 4.6 nm Au NCs capped with (N2H5)4Sn2S6and flocculated by gently increasing the $(N_2H_5)_4Sn_2S_6$ concentration.

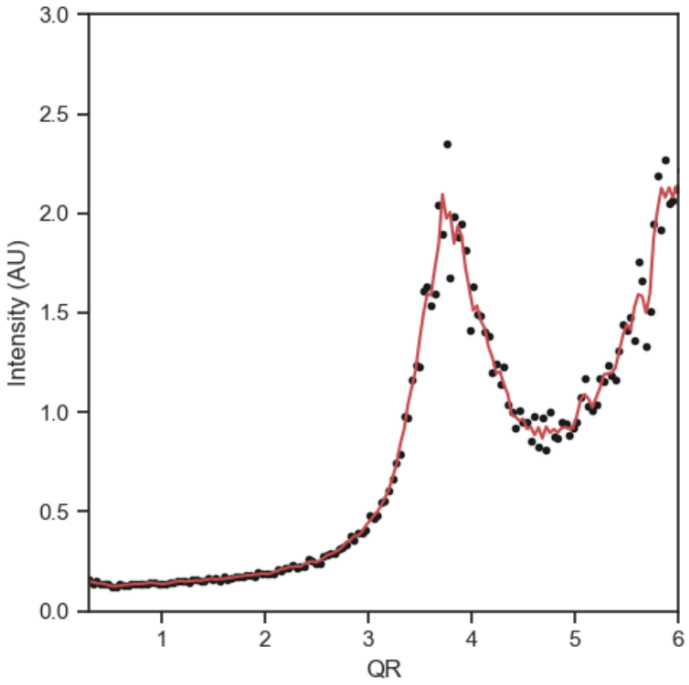

Figure 3-15: NC dense liquid phase structure factor.

Extracted structure factor for a typical "dense fluid" shown in Figure 3-14A for PbS NCs with an average diameter of 5.5 nm. Black points represent the raw data, and the red trace is a 3-point running boxcar average.

A qualitatively different pathway was observed for the assembly of 5.5 nm PbS NCs in NMF flocculated with K_3AsS_4 in the presence of acetonitrile (Figure 3-14A and Figure 3-17). The SC nucleation was preceded by a separation of the homogeneous colloid into droplets of dilute and dense fluids according to the binodal line of the phase diagram, and the nucleation occurred within the metastable dense fluid phase. Such a pathway is reminiscent of the nonclassical two-step nucleation, which is rather common for globular proteins.[37,38]

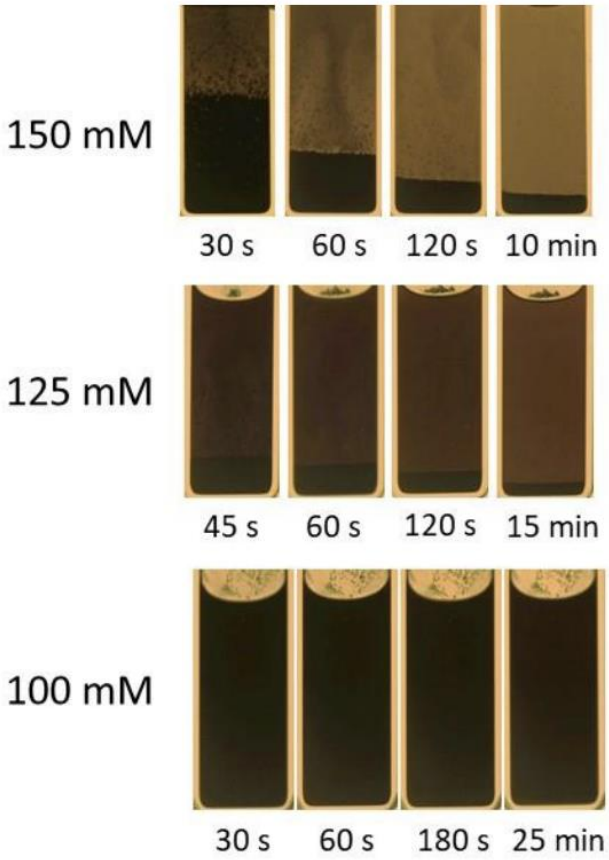

Figure 3-16: Visual inspection of Au supercrystal flocculation.

Photographs of 4.4 nm Au NCs with $Sn_2S_6^{4-}$ surface ligands in hydrazine taken immediately after the addition of $(N_2H_5)_4Sn_2S_6$ ligands to final concentrations of 150, 125, and 100 mM. Samples are suspended in 1 mm path length glass cuvettes and photos are taken inside of a nitrogen filled glovebox.

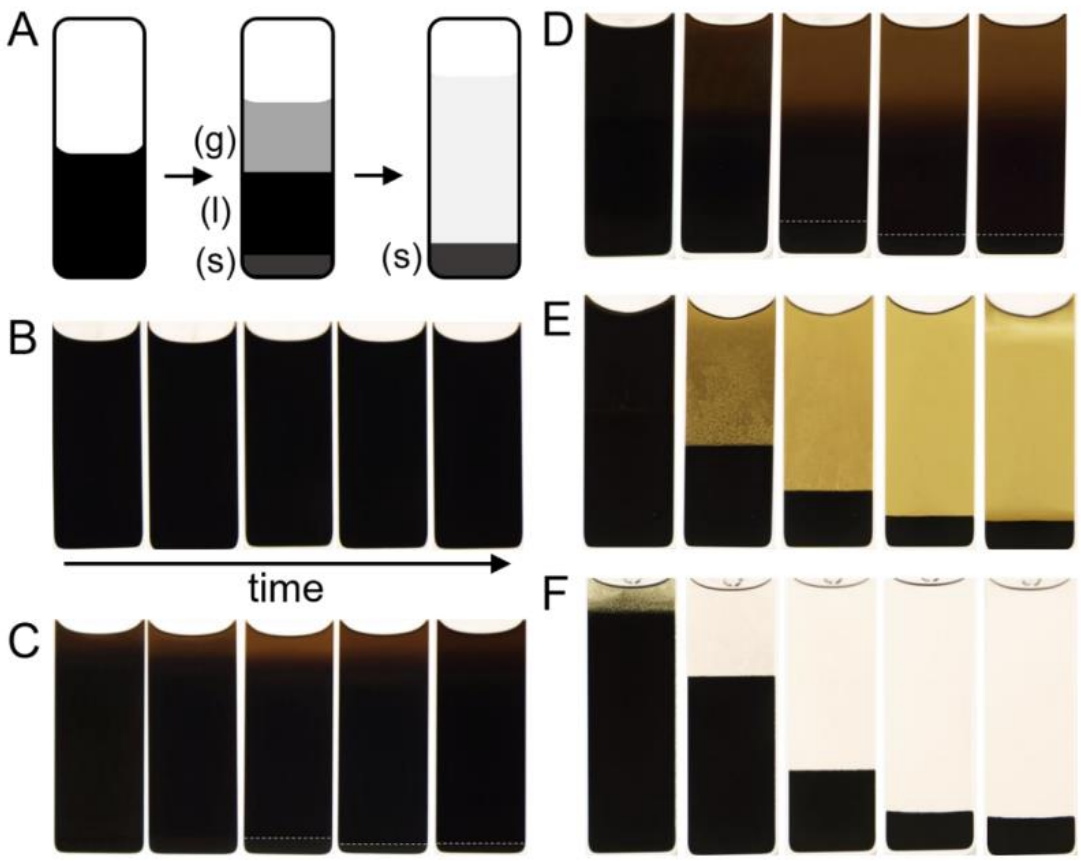

Figure 3-17: Phase separation of PbS NCs and triple-phase coexistence.

(**A**) Schematic representation of a colloidal solution partially destabilized to a triple phase coexistence and further destabilized to a solid precipitate. (**B-F**) Photographs (1 mm path length) of PbS NCs initially at 200 mM K_3AsS_4 in NMF diluted with 17, 21, 25, 29, and 32% ACN v/v, respectively. Phots are taken at 10 min, 20 min, 50 min, 11 hr, and 23 hr time points (left to right). Dotted white lines indicate solid-liquid phase separation visible by eye.

3.6. Kinetics of supercrystal nucleation

Experimental data for the self-assembly of MCC capped PbS NCs suggests a two-step nucleation pathway of supercrystals based on the phase separation of colloidal NCs into dilute and dense fluid phases. Here, I directly measure the nucleation behavior via in situ SAXS at multiple representative points within the NC phase diagram (Figure 3-18). The relative quench depth (effective temperature) of the NC solution is controlled by tuning both the ionic strength (K_3AsS_4

concentration) and solvent dielectric constant. N,N'-dimethylformamide (ε_{DMF}=37) serves as an effective non-solvent to control the screening length while maintaining similar molecular structure to the primary N-methylformamide solvent (ε_{NMF}=171). The final NMF:DMF ratios of 60:40 set the total dielectric constant at $\varepsilon_{60:40}$~90.[39] The NC concentration, reported here as volume fraction (ϕ), also determines the nucleation dynamics and relative position of the binodal line. The binodal line is often measured up to volume fractions of ϕ = 0.5 and above for proteins and polymer spheres due to relatively low Hamaker constants and vdW attractive forces from the primarily carbon-based materials. The maximum concentration of PbS-Sn_2S_6 NCs in pure NMF is $\phi \sim 0.07$ (~500 mg/mL PBS), but these high concentrations are not experimentally accessible for self-assembly which requires additional MCC ligands and DMF non-solvent. The maximum concentrations of PbS NCs relevant to self-assembly are ϕ ~ 0.005-0.01 (~50-100 mg/mL PbS).

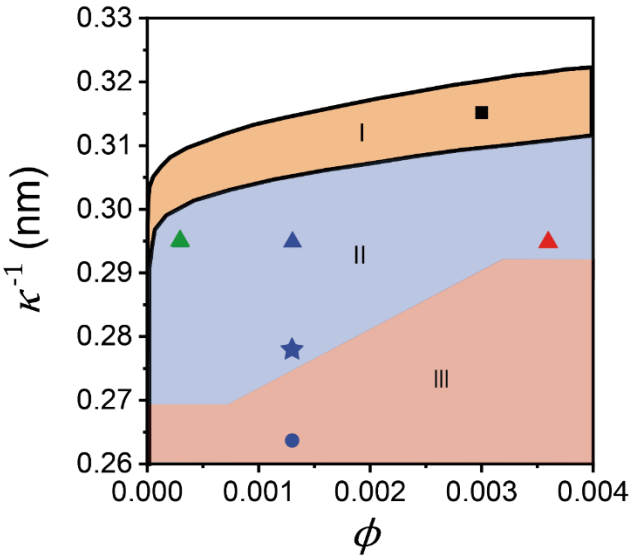

Figure 3-18: Phase diagram for PbS NCs in NMF/DMF.

Colloidal phase diagram schematic for PbS-Sn_2S_6 NCs in 60:40 NMF:DMF solvent based on experimental data. The y-axis is plotted as the calculated Debye length (κ^{-1}) which serves as a proxy for the effective temperature. The experimental binodal line is estimated to lie within region I where one-step self-assembly is observed in close proximity to the binodal line. Region II depicts conditions where two-step assembly is observed with varying nucleation kinetics. Region III depicts a boundary where kinetic trapping causes increased disorder in supercrystals.

The PbS NC phase diagram was explored by progressively lowering the effective temperature of the solution and the Debye length, κ^{-1}, is used as an experimentally accessible stand in for effective temperature:

$$\kappa^{-1} = \sqrt{\frac{\varepsilon_{sol}\varepsilon_0 k_B T}{2e^2 I}}$$

where ε_{sol} is the dielectric constant of the solvent and I is the ionic strength. At low quench depths, the first behavior encountered is the direct one-step nucleation of supercrystals with no observable liquid intermediates at a ligand concentration of 175 mM (Figure 3-19). One-step nucleation is expected to occur in close proximity to the binodal line, and similar behavior was indeed accessible at multiple NC concentrations tracing out an approximate region for the experimental binodal line. Higher MCC concentrations of 200 mM K_3AsS_4 revealed a variety of two-step nucleation behavior beneath the binodal line. At low NC concentrations (ϕ = 0.0003), a liquid phase emerged within seconds and persisted in a relatively constant equilibrium with the colloidal gas (Figure 3-20A,B). Supercrystals began to emerge after ~10 minutes, but in very small yields with a slow nucleation rate. At slightly higher NC concentrations (ϕ = 0.0013 and ϕ = 0.0035), a similar liquid structure emerges immediately after injection, but the kinetics of SC nucleation are progressively increased due to the higher density of NCs in solution (Figure 3-20C-F).

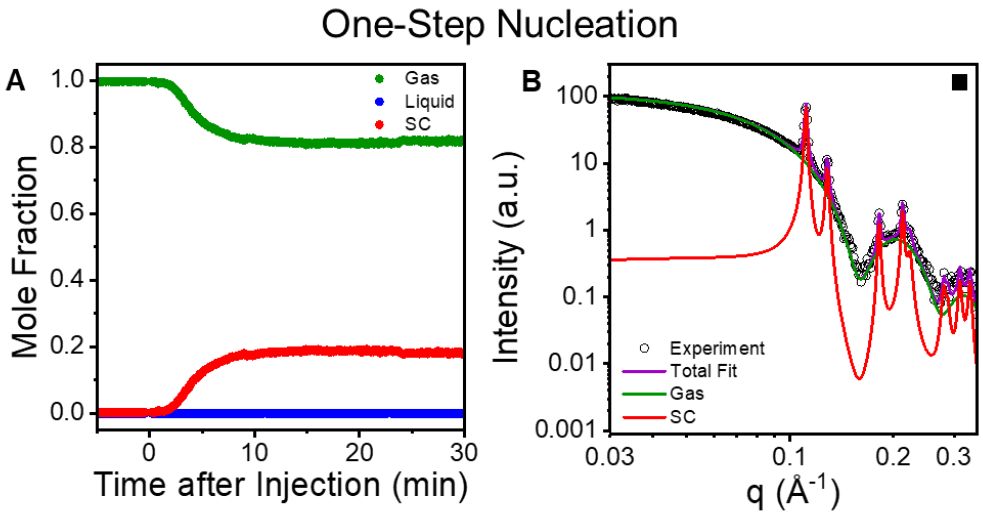

Figure 3-19: One-step in situ nucleation kinetics.

Self-assembly of 5.7 nm PbS-Sn_2S_6 NCs from a solution with 175 mM K_3AsS_4 and 21 mg/mL PbS (ϕ=0.003) in 60:40 NMF:DMF (Black square in Figure 3-18). (**A**) Calculated total contributions of colloidal gas, liquid and SC to the total fit of SAXS intensity at each time point. (**B**) Total fit contributions to experimental SAXS data at t=30 min. No dense liquid phase is observed under these conditions.

Holding the NC concentration constant (ϕ = 0.0013) and progressively increasing the MCC ligand concentration allows two-step assembly to procced until the attractive forces become too strong and kinetically trapped amorphous aggregates begin to dominate. Two-step nucleation is observed for both 200 and 225 mM K_3AsS_4 with increasing crystalline yields for the lower quench depth (Figure 3-21). Continuing to move down on the phase diagram at 250 mM, however, significantly alters the interparticle potential such that only a small amount of supercrystals are assembled with broadened diffraction peaks due to small crystallite sizes and increased disorder.

Continuous exposure to X-rays can significantly alter the sample dynamics, and steps were taken to minimize the total beam exposure during continuous in situ monitoring by sample stirring. Phase contributions of NC gas, liquid and solid were performed by fitting data with four terms. A background q^{-4} scattering term was included to account for Porod scattering from 3D structures.

The colloidal gas was fit with a spherical form factor with a 5.7 nm average diameter and Gaussian broadening.[40] Solid supercrystals were fit with a structure factor for a finite sized fcc crystal with Lorentzian peak shapes. The metastable liquid phase was fit with a Percus-Yevick hard sphere liquid structure factor.[41] It should be noted that separating the contribution of NC liquid and amorphous aggregate is difficult and the results presented here do not make distinction between the two phases. At the conclusion of experiments, multiple samples were observed to have a persistent dense fluid phase in the cuvette after stirring is stopped which confirms the presence of a metastable dense liquid phase.

Similar in situ SAXS of Au-Sn_2S_6 NCs in hydrazine was also collected which confirmed the one-step nucleation of Au supercrystals regardless of final ionic strength or MCC injection speed (Figure 3-22). No liquid-like intermediate states are observable at short times after ligand injection, and continuous addition of MCC ligands to the NC colloid shows clear fcc supercrystal growth at the expense of the colloidal background.

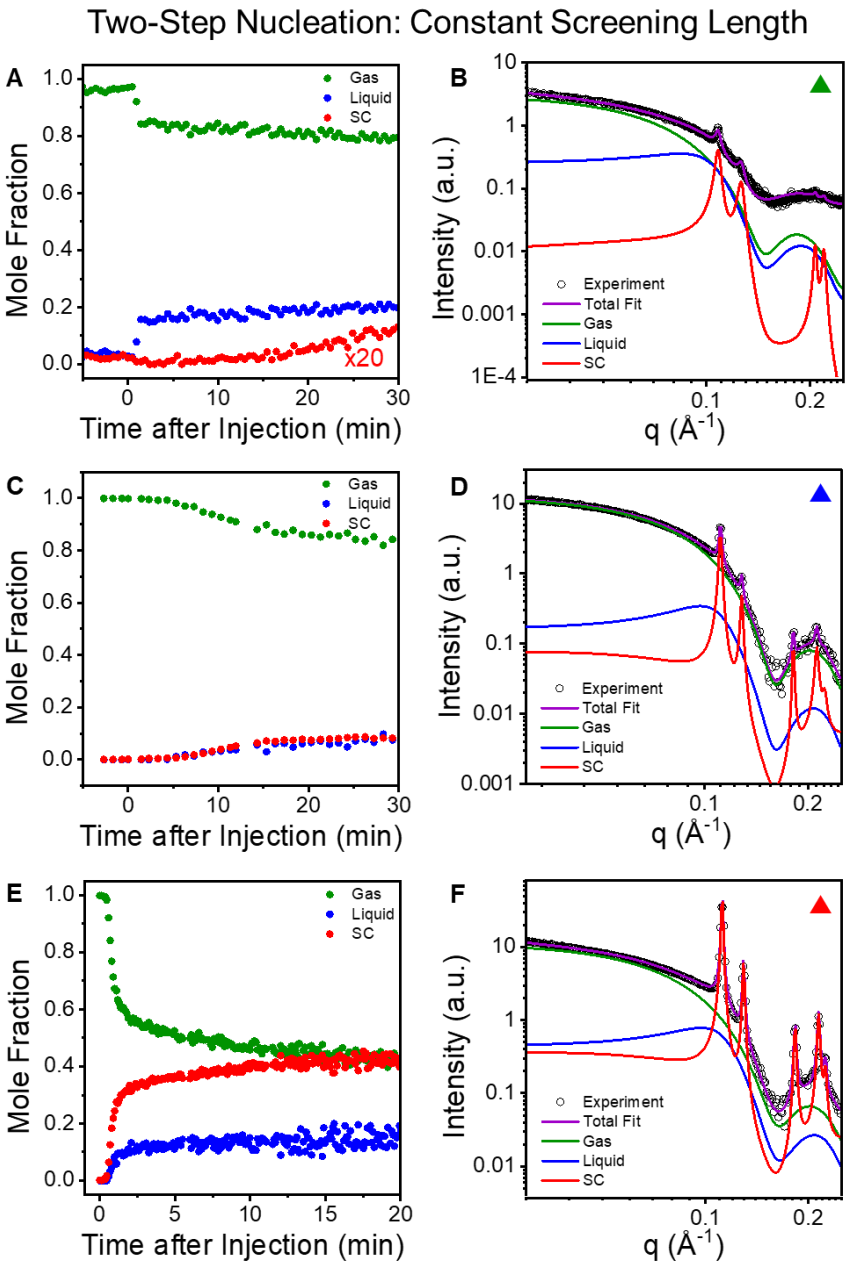

Figure 3-20: Two-step in situ nucleation at constant screening length.

Kinetics of 5.7 nm PbS-Sn_2S_6 NCs at 200 mM K_3AsS_4 in 60:40 NMF:DMF with conditions corresponding to green, blue, and red triangles on Figure 3-18. Two-step nucleation kinetics and total supercrystal yield increase with increasing NC concentration. Left column shows kinetics of fitted SAXS data to colloidal gas, liquid and, supercrystal components. Right column shows fitted SAXS data at t=30 min. (**A,B**) 2.1 mg/mL PbS NCs (ϕ=0.0003). (**C,D**) 10 mg/mL PbS NCs (ϕ=0.0013). (**E,F**) 27 mg/mL PbS NCs (ϕ=0.0036).

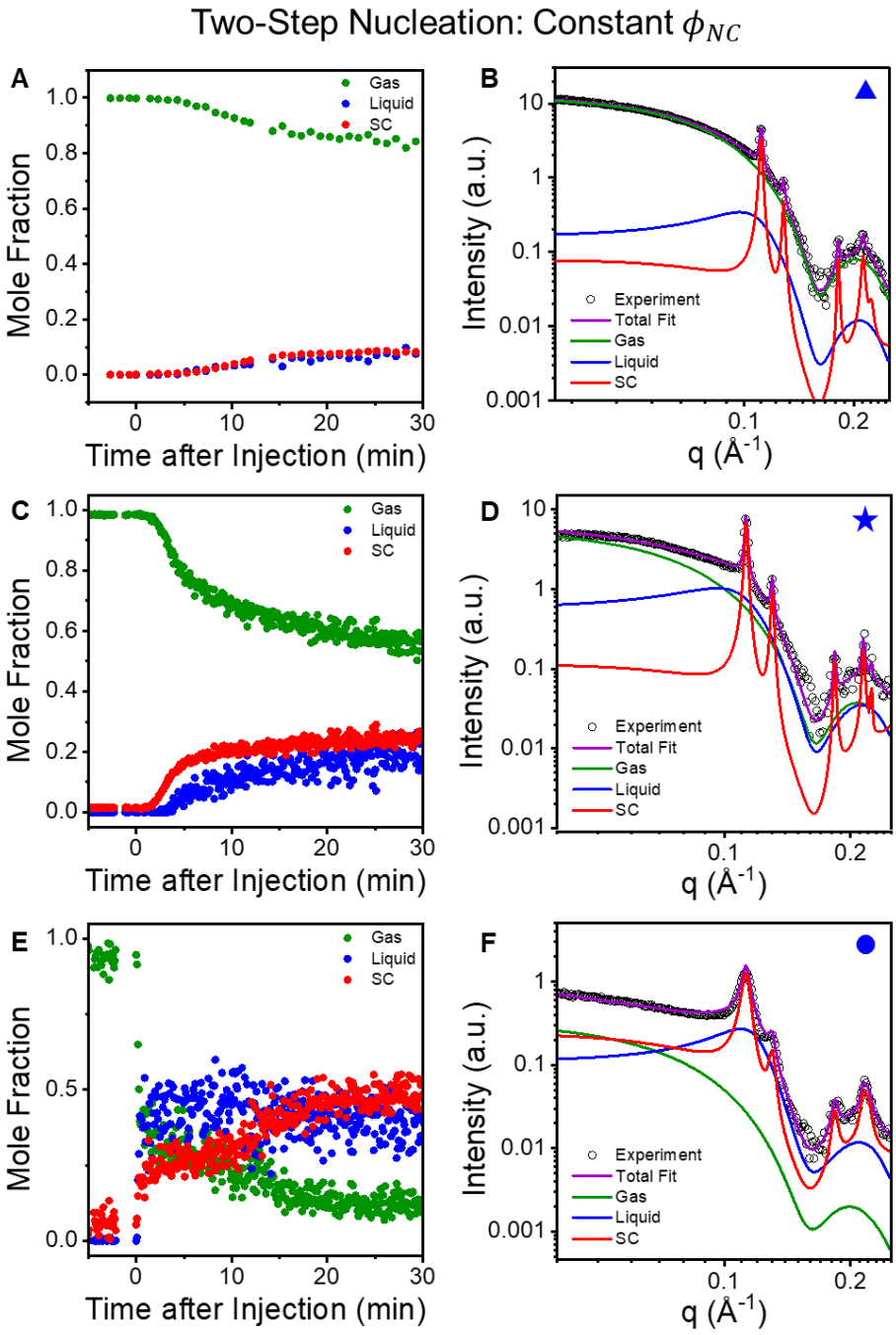

Figure 3-21: Two-step in situ nucleation at constant ϕ_{NC}.

Kinetics of 5.7 nm PbS-Sn_2S_6 NCs at 10 mg/mL PbS (ϕ=0.0013) in 60:40 NMF:DMF with conditions corresponding to the blue triangle, star, and circle on Figure 3-18. Deeper quench depths lead to higher crystalline yields and eventually kinetic trapping. Left column shows kinetics of fitted SAXS data to colloidal gas, liquid and, supercrystal components. Right column shows fitted SAXS data at t=30 min. (**A,B**) 200 mM K_3AsS_4 (κ^{-1} = 0.295 nm). (**C,D**) 225 mM K_3AsS_4 (κ^{-1} = 0.278 nm). (**E,F**) 250 mM K_3AsS_4 (κ^{-1} = 0.264 nm).

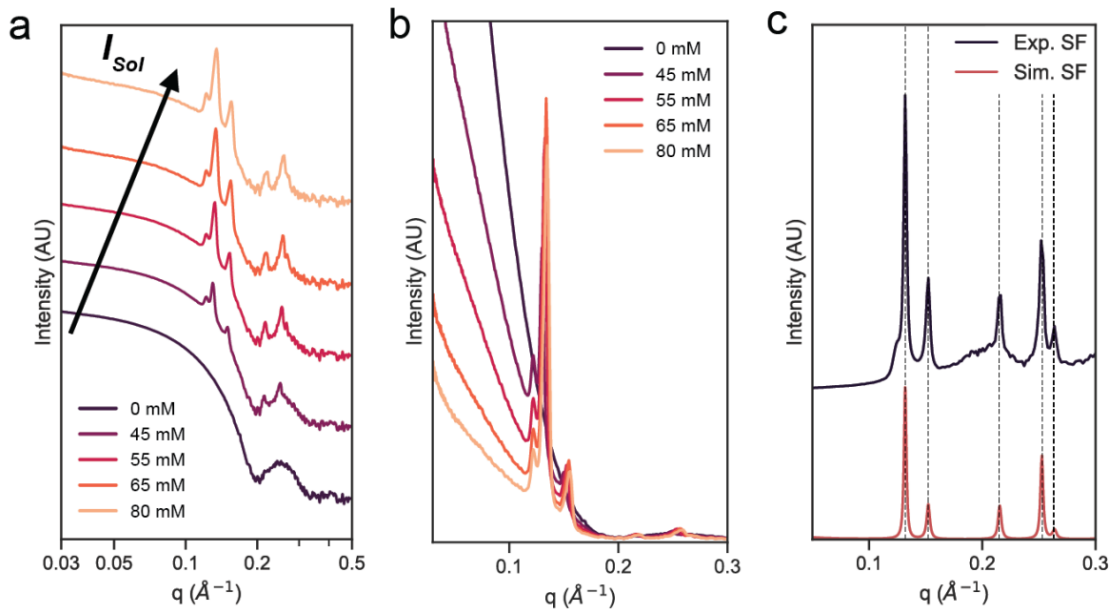

Figure 3-22: In situ monitoring of one step Au SC nucleation.

(**a**) Offset log-log SAXS patterns of 4.2 nm Au NCs at increasing concentrations of $(N_2H_5)_4Sn_2S_6$ measured continuously via in situ SAXS while the sample stirred. (**b**) The data from panel a shown on a linear scale (not offset), showing the decrease of colloidal background as the crystalline peaks grow, indicating incorporation of free colloidal particles into a crystalline solid. (**c**) Comparison of experimental and simulated fcc structure factor for the same particles at a ligand concentration of 50 mM.

3.7. Crystallographic alignment across all-inorganic PbS supercrystals

Lead chalcogenide NCs including PbS and PbSe are widely known for their highly faceted surfaces which lead to a size dependent shape seen across many synthetic protocols. Small PbS NCs under 4 nm tend to have an octahedral shape, and medium NCs sizes (4-8 nm) transition to truncated octahedra with (100) facets becoming energetically favorable due to steric crowding of oleic acid ligands on PbS surfaces.[23] Even larger PbS NCs above 8 nm often become cubes or rounded cubes with a high fraction of (100) surfaces. Self-assembly of these oleate capped PbS NCs can lead to superlattices with atomic alignment of the rock salt PbS NCs across single crystalline domains due to two factors: non-spherical shapes and facet dependent ligand binding. In one example, surface oxidation of (100) facets lead to a lower ligand density relative to non-

oxidized (100) surfaces, and the oxidized NCs assembled into bcc crystals with NCs sharing a common atomic alignment in the bcc unit cell.[42] Repeated washing of PbS NCs can also remove weakly bound oleate from (100) surfaces which can lead to the preferential assembly of different binary superlattice phases depending on the (100) PbS ligand density.[43]

The nature of MCC ligand binding to PbS (111) and (100) surface facets is not known, but any oxidation of (100) surfaces likely leads to a decreased MCC ligand grafting density due to full passivation of the lead atoms similar to the example of oleic acid ligands. Here, the PbS NCs presented are synthesized with rigorous air-free methods during synthesis, purification, ligand exchange, and self-assembly steps to reduce the chance of surface oxidation playing a major role in the NC surface chemistry. The surface termination of (111) surfaces, with surface lead atoms missing half of their total coordination sphere in a rock salt structure, allows for the strong X-type ligand binding of MCC anions such as thiostannate ($Sn_2S_6^{4-}$) as either a monodentate or bidentate ligand. Stoichiometric (100) PbS surfaces, however, have surface lead atoms with only one sulfur missing from their coordination sphere, reducing the strength of ligand interactions and making L-type association with both surface lead and sulfur atoms more likely.[44]

Characterization of PbS-$Sn_2S_6^{4-}$ supercrystals reveals large micron sized single crystals with an fcc structure (Figure 3-23). Selected area electron diffraction (SAED) across the entire single crystal supercrystal shows an array of diffraction peaks from the PbS atomic lattice with no obvious rings due to random orientation of PbS NCs. Close inspection of high-resolution TEM of PbS atomic lattices confirms that PbS NCs are crystallographically aligned across the entire supercrystal. Based on FFT analysis of both the fcc supercrystal and atomic PbS crystal ordering, I find that PbS NCs are coaligned with the fcc supercrystal along the $[110]_{NC}$ and $[110]_{SC}$ zone axes. Unit cell parameters and d spacings for the supercrystal and PbS atomic lattice calculated

from the (200) and (111) peaks in FFT images are in good agreement with values obtained by SAXS of a supercrystal granular powder and literature values of the PbS rock salt lattice (Table 3-1).

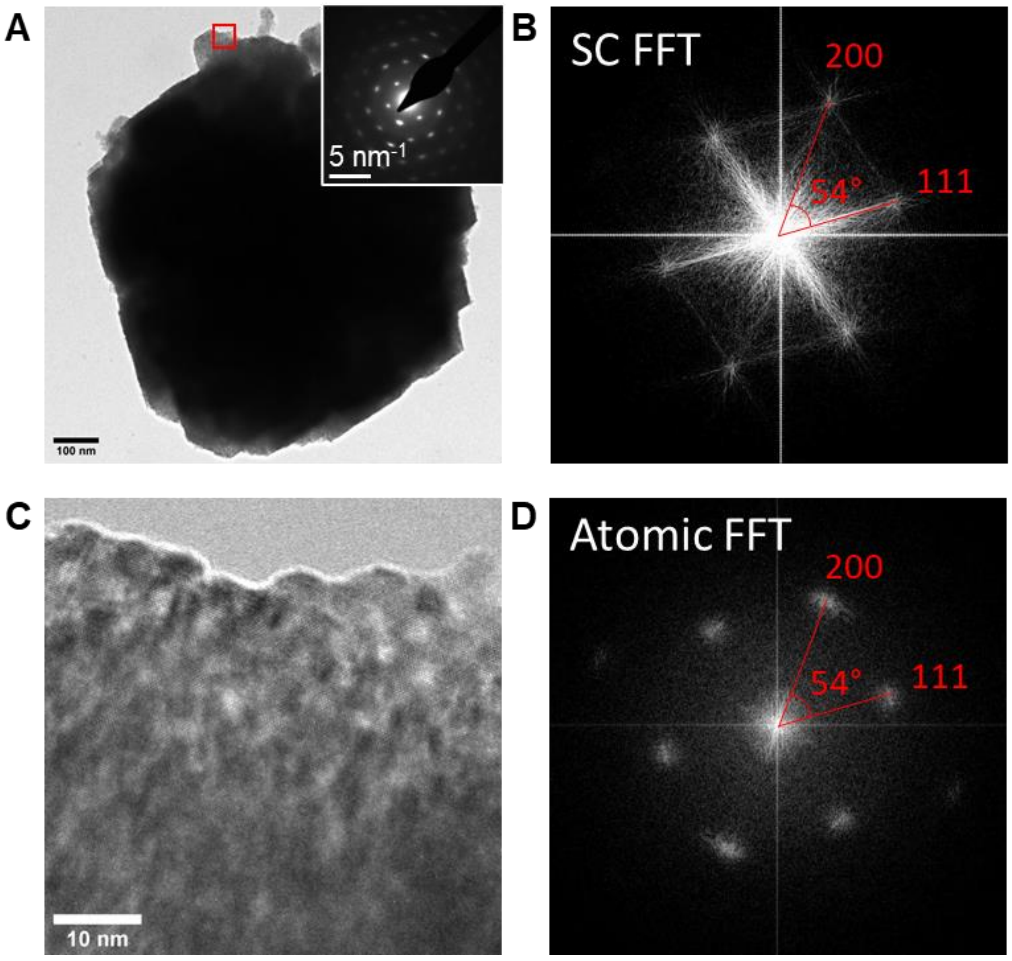

Figure 3-23: Atomic coherence in PbS supercrystals.

(**A**) TEM image of a single supercrystal assembled from 5.7 nm PbS-Sn_2S_6 NCs in NMF with a single crystal fcc domain. Inset: Electron diffraction across the entire supercrystal displaying diffraction peaks from the atomic [110] zone axis of rock salt PbS NCs. (**B**) FFT of the TEM image in panel A. Peaks from (200) and (111) planes are visible from the image on the [110] zone axis of the fcc supercrystal. (**C**) High-magnification TEM from the edge of the same supercrystal (red square in panel A). Atomic planes of the PbS crystal structure are visible along the edges of the entire supercrystal with visible alignment between all NCs. (**D**) FFT of the TEM image in panel C in agreement with the global atomic ordering observed by electron diffraction. PbS atomic rock salt lattices are imaged along the [110] zone axis and are aligned with the symmetry of the fcc supercrystal.

Table 3-1: Unit cell parameters and d spacings measured from an fcc supercrystal assembled from 5.7 nm PbS NCs and PbS NC atomic lattices.

	$d_{111\text{-}SC}$ (nm)	$d_{200\text{-}SC}$ (nm)	a_{SC} (nm)	$d_{111\text{-}PbS}$ (Å)	$d_{200\text{-}PbS}$ (Å)	a_{PbS} (Å)
SC SAXS	5.09	4.41	8.81	-	-	-
SC TEM FFT	5.1	4.4	8.8	-	-	-
Atomic PbS FFT	-	-	-	3.4	3.0	5.9
Lit. Atomic PbS	-	-	-	3.427	2.968	5.936

A schematic model of the supercrystal fcc unit cell was created using truncated octahedral PbS NC shapes expected for a 5.7 nm PbS diameter. Based on the observed alignment between fcc and rock salt crystal structures, the NCs are oriented with (100) surfaces along the (100) fcc unit cell surface (Figure 3-24). In this structure, the NCs maintain an edge-to-edge configuration while the ligand rich NC surfaces form the boundary of both tetragonal and octagonal interstitial sites surrounded by four (111) or six (100) PbS surfaces, respectively. The surface-to-surface distance between opposing (100) facets is ~3.1 nm across the octagonal interstitial sites, and the total packing fraction of the PbS NC cores in the fcc unit cell is ~57% without including volume contribution from thiostannate ligands.

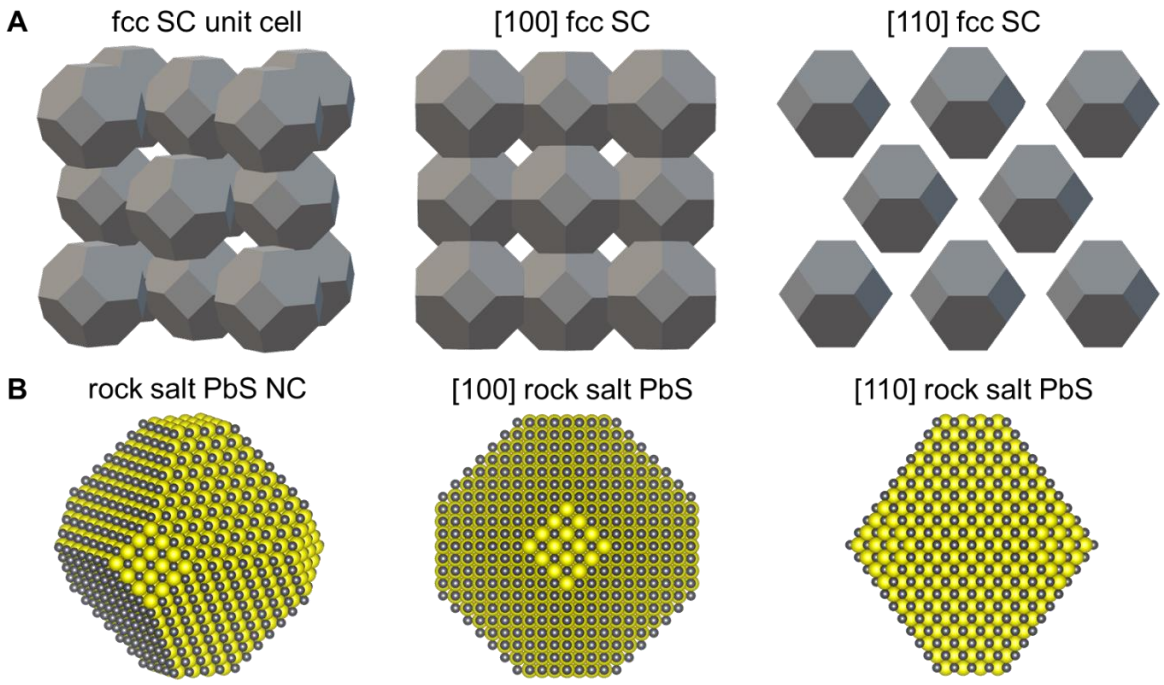

Figure 3-24: Unit cell reconstruction of atomically aligned PbS NCs

(**A**) Schematic representations of truncated octahedral PbS NCs with orientational alignment between the fcc SC and atomic PbS crystal lattices. A 3D reconstruction of the fcc unit cell is shown along with projections along the [100] and [110] zone axes. NC sizes and interparticle spacings are not drawn to scale. (**B**) Schematic model of a ~5.7 nm PbS NC with a rock salt atomic crystal structure and truncated octahedral shape. Projections are shown along the [100] and [110] atomic zone axes.

PbS NCs form edge-to-edge configurations in supercrystals to maximize the distance between repulsive, charged surfaces (Figure 3-25A). The (111) PbS surfaces form the boundary of tetrahedral sites in the fcc unit cell which take the shape of an octahedron due to the NC surface faceting. Coherent orientation is confirmed in fully contracted supercrystals after washing, but the orientational order should preferentially form in the expanded fcc supercrystals as NCs become restricted in the fcc lattice. Previous examples of atomic alignment in PbS superlattices with organic ligands has proceeded through complex phase transformations from fcc to bcc crystals,[45] but in all cases the ligand rich (111) NC surfaces orient with a surface-to-surface alignment (Figure 3-25B). This surface-to-surface alignment can be interpreted as an

additional ‘bond’ forming between organic surfaces that change the enthalpy of interparticle interactions throughout lattice contraction. Opposing atomic alignment moving from soft organic ligands to hard inorganic anions is unsurprising given the replacement of attractive vdW interactions with highly repulsive charged MCC anions.

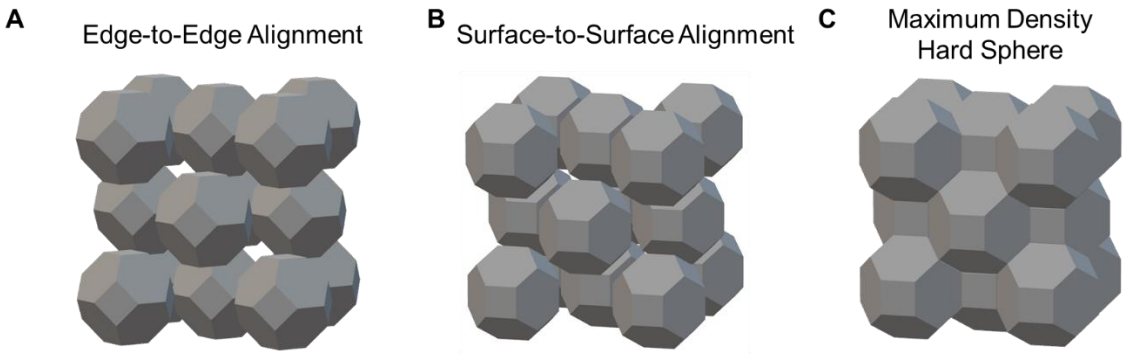

Figure 3-25: PbS NC orientations in atomically aligned supercrystals.

Schematic diagrams of PbS NC packing in an fcc unit cell with (**A**) edge-to-edge and (**B**) surface-to-surface alignment interparticle space pictured due to surface ligand contributions. PbS NCs self-assemble into edge-to-edge structures due to the additional interstitial space to accommodate charged surface ligands. (**C**) The maximum density packing for truncated octahedral shapes in the hard sphere limit with total space filling.

3.8. Gallery of TEM images showcasing additional self-assembly of semiconductor nanocrystals

Additional examples of charged semiconductor NC self-assembly in polar solvents. Descriptions of the NC surface chemistry, size, and flocculation are contained in figure captions below.

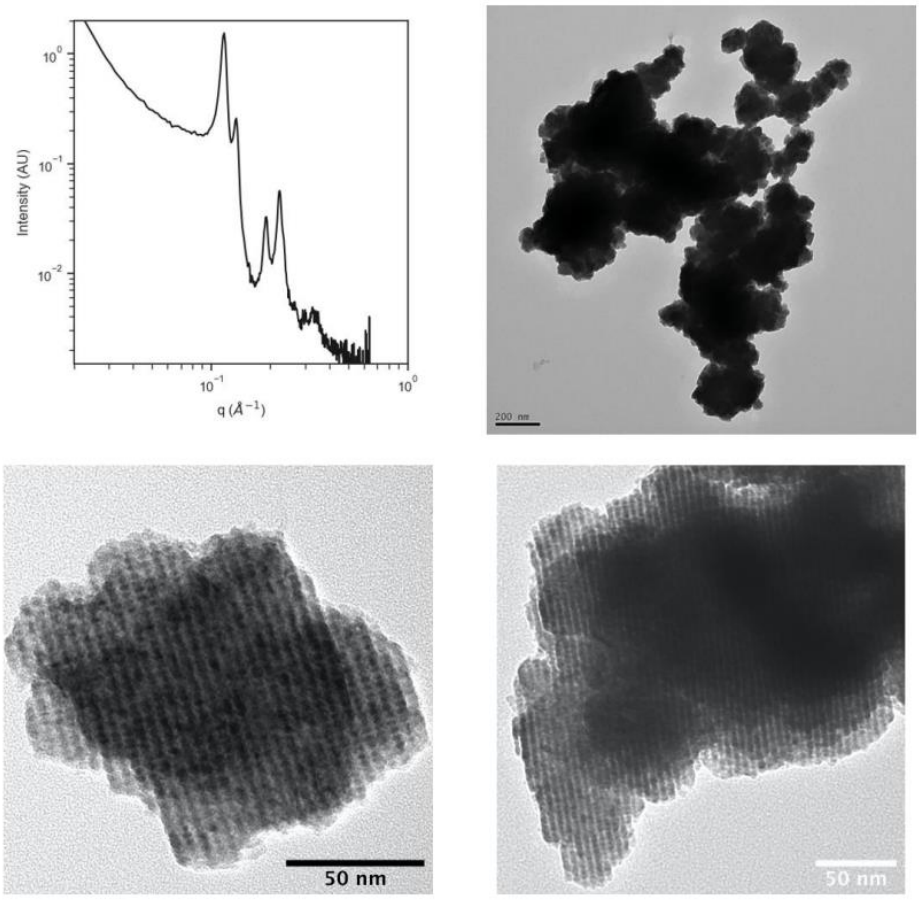

Figure 3-26: Rapid flocculation and assembly of PbS NCs.

Assembly results for 5 nm PbS-Sn_2S_6 NCs flocculated with K_3AsS_4 followed by fast addition of ACN.

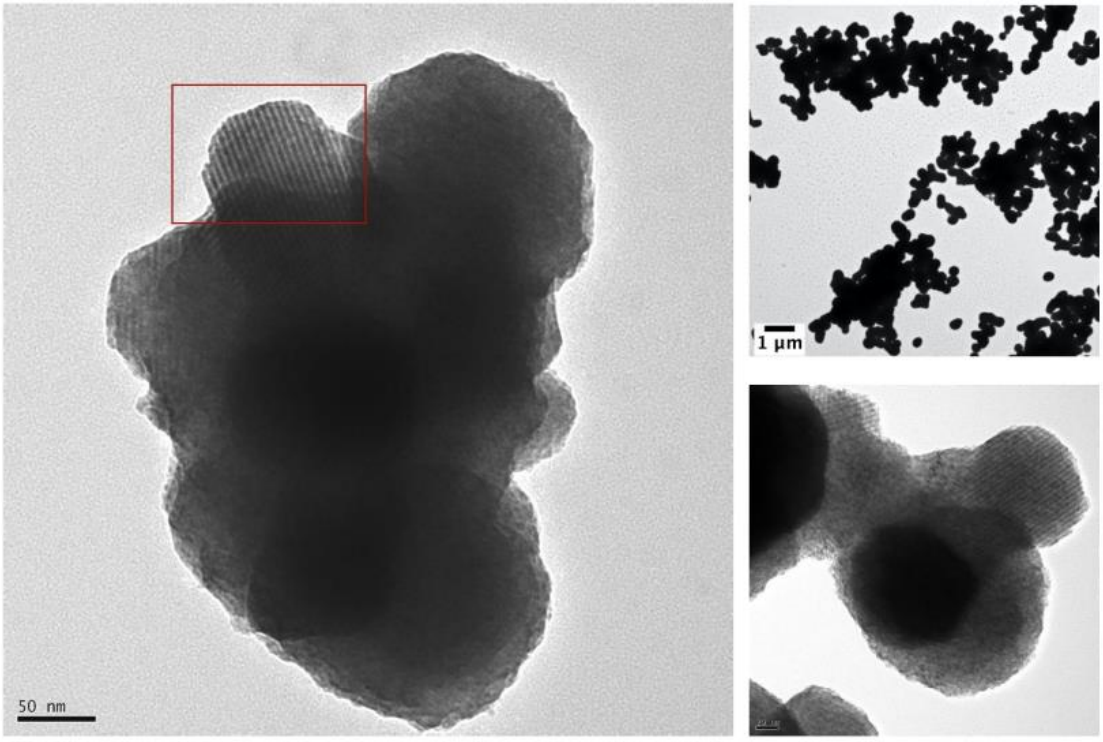

Figure 3-27: Slow flocculation and assembly of PbS NCs.

TEM images at various magnifications of assembly results for 4.5 nm PbS-Sn_2S_6 NCs flocculated with K_3AsS_4 in NMF followed by slow addition of ACN. Crystalline regions are seen emerging from clumps of amorphous dense aggregates.

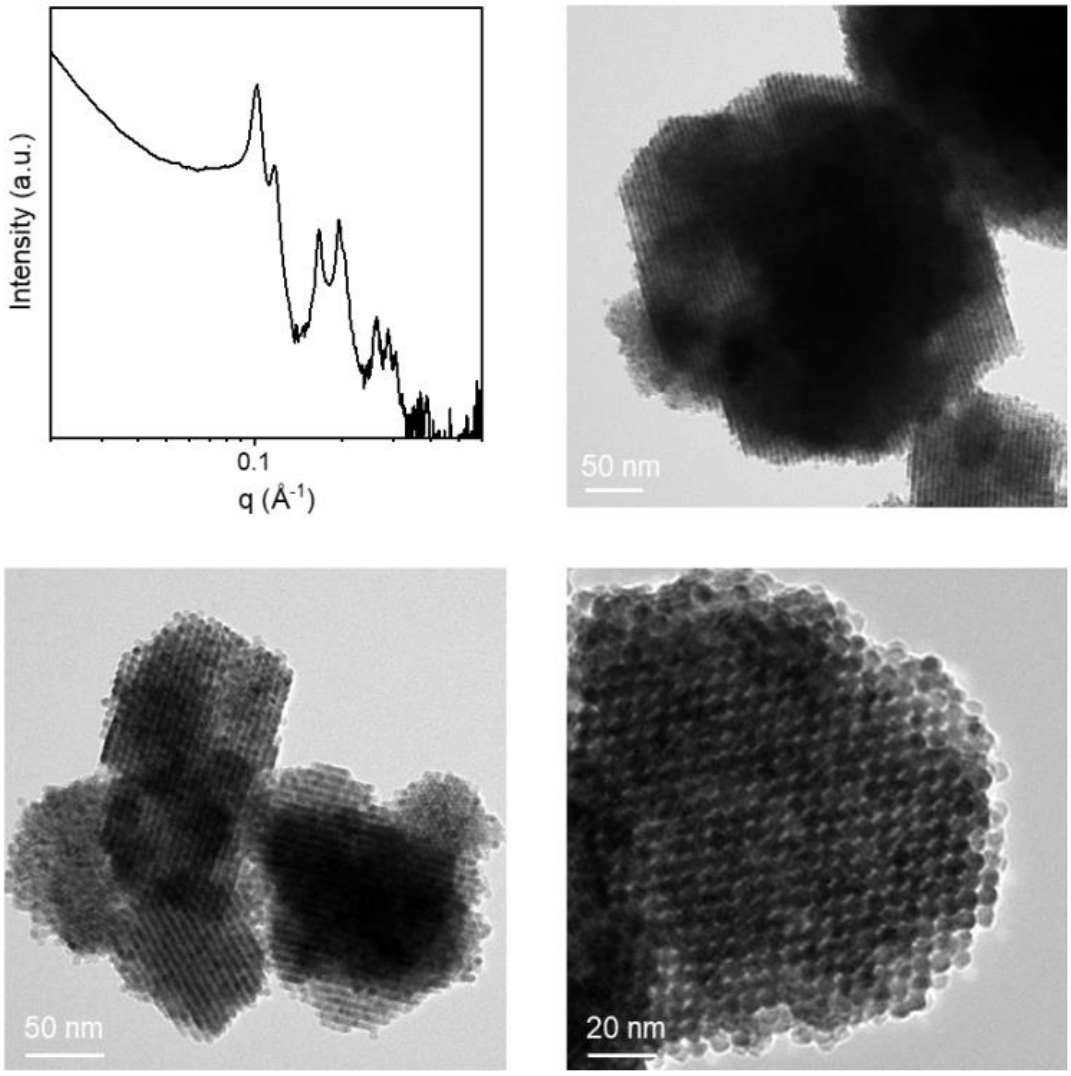

Figure 3-28: Self-assembly of MCC capped PbSe NCs.

Assembly results for 6 nm PbSe NCs stabilized by $K_4Sn_2S_6$ ligands in N-methylformamide. The colloid was first brought to a ligand concentration of 200 mM K_3AsS_4 followed by addition of acetonitrile to fully flocculate the sample.

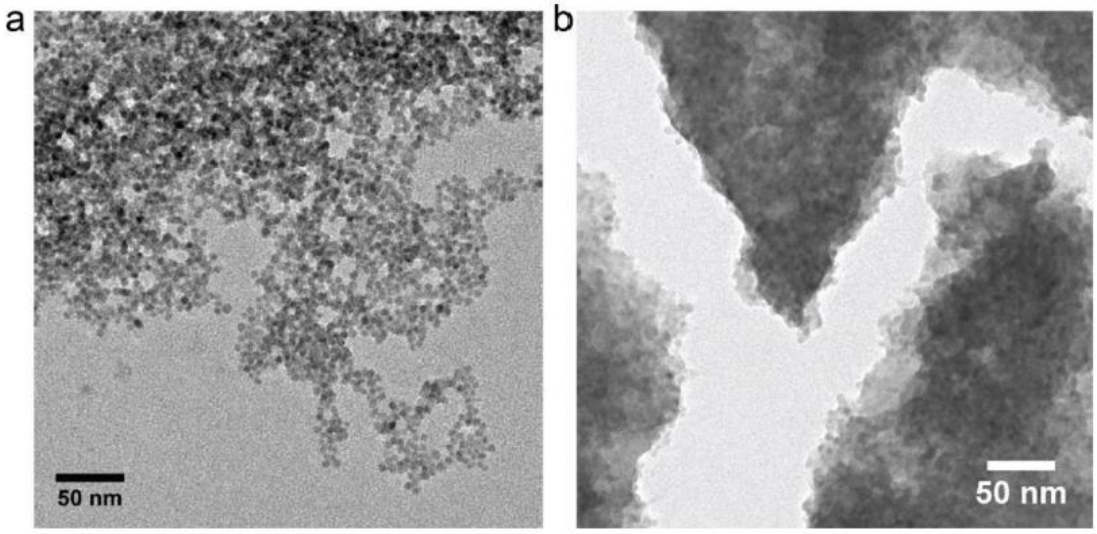

Figure 3-29: Flocculation of CdSe NCs from polar solvents.

Assembly results for 5 nm CdSe NCs in hydrazine flocculated with (**a**) ACN resulting in a low-density fractal aggregate and (**b**) additional $(N_2H_5)_4Sn_2S_6$ and ACN resulting in compact aggregates with no long-range order.

3.9. Experimental Methods

Chemicals:

Potassium sulfide (95% anhydrous), alladium(II) acetylacetonate, (99%), Nickel(II) acetylacetonate, (anhydrous, min. 95%), and Tri-n-octylphosphine (97%) were purchased from Strem Chemicals.

Gold(III) chloride trihydrate (≥99.9% trace metals basis), Borane tert-butylamine complex (powder, 97%), Oleylamine (70%, tech.), Cadmium oxide (99.99% Cd), Lead(II) Oxide (99.999%), Oleic acid (90%), 1,2,3,4-Tetrahydronaphthalene (ReagentPlus, 99%), hexamethyldisilathiane (synthesis grade), selenium (99.99% pellets), tellurium (99.999%), Arsenic powder (≥99.997% trace metals basis), 1-octadecene (90%), Oleic acid (90%), 1-

Dodecanethiol (≥98%), Hydrazine (anhydrous, 98%), N-Methylformamide (99%), Hexane (99%), and Toluene (99.8%) were purchased from Millipore Sigma.

N-Methylformamide (99%), Sulfur (99.999%), Arsenic(III) sulfide (Powder, 99.99%), Copper(I) sulfide, (99.5%), Tin powder, (325 mesh, 99.8%, metals basis) and Indium(III) selenide (99.99% metals basis) were obtained from Alfa Aesar.

Arsenic(V) sulfide was purchased from Santa Cruz Biotechnology.

Tetradecylphosphonic acid was purchased from PCI.

N-methylformamide was purified by standard vacuum distillation techniques and stored in a nitrogen glovebox with molecular sieves. All other chemicals were used without purification.

Nanocrystal Synthesis:

All nanocrystals were synthesized according to previously reported methods with details provided in the supplementary information.

Au: Au nanocrystals were synthesized by previously reported methods.[46,47]

Pd: Pd nanoparticles were prepared via decomposition of a Pd-TOP complex in the presence of oleic acid.[48]

Ni: Ni nanoparticles were prepared by decomposition of nickel acetylacetonate in a mixture of tri-n-octylphosphine and oleylamine according to ref [49].

CdSe: Phosphonate capped wurtzite [50] and carboxylate capped zincblende CdSe [51] particles were prepared by literature methods.

PbS: PbS nanocrystals were synthesized according to previously reported methods [52,53].

PbSe: PbSe nanocrystals were synthesized according to a previously detailed method [54].

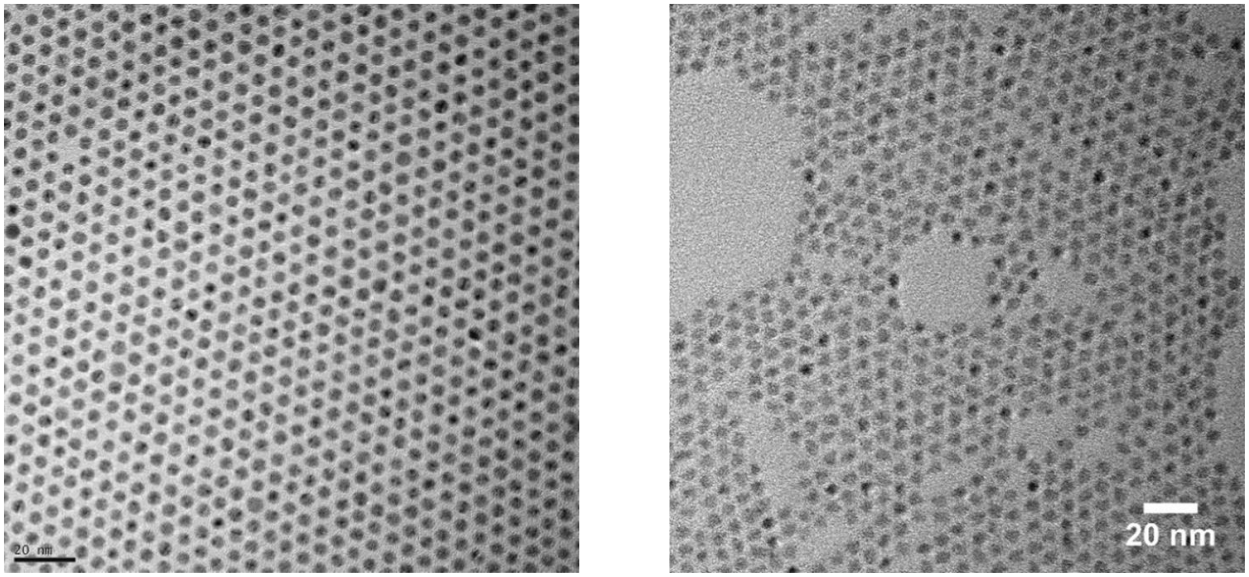

Figure 3-30: Representative NC populations.

TEM micrograph of (left) 4.5 nm Au nanocrystals and (right) 4.6 nm PbS nanocrystals.

MCC Ligand Synthesis:

All methods were performed in a nitrogen glovebox unless otherwise stated. Preparation of the MCC ligands was based on previously reported methods.[55,56] In general, MCCs were prepared as 0.25 M or 0.5 M stock solutions in either hydrazine or N-methylformamide (NMF) by reacting metal chalcogenides with excess chalcogen in the desired stoichiometry. For hydrazinium ($N_2H_5^+$) based species, hydrazine can act as both solvent and redox mediator allowing synthesis directly from elements. For MCCs with other cations in non-hydrazine solvent, metal chalcogenides were reacted with the appropriate alkali metal chalcogenide (e.g. K_2S). *Caution: Special care should be taken when using hydrazine in exothermic reactions which can release hazardous, flammable vapors with a risk of detonation if heated in sealed containers.*

$(N_2H_5)_4Sn_2S_6$, $(N_2H_5)_4Sn_2Se_6$, and $(N_2H_5)_3AsS_4$: Synthesized as 0.25 or 0.5 M solutions in hydrazine with stoichiometric ratios of the appropriate elements and stirring for >24 hours. For

example, a 0.25 M solution of $(N_2H_5)_4Sn_2S_6$ was prepared by adding Sn powder (2 mmol, 0.237 g), sulfur (6 mmol, 0.192 g), and 4 mL anhydrous hydrazine a 20 mL glass vial with a Teflon coated stirbar. The solution was stirred at room temperature for 48 hours to form a transparent colorless solution. A small amount of excess sulfur may be required for full dissolution of Sn.

$(N_2H_5)_2In_2Se_4$ and $(N_2H_5)_2Cu_4S_6$: Synthesized as 0.25 M solutions in hydrazine by reacting an appropriate metal chalcogenide with elemental chalcogen. For $(N_2H_5)_2In_2Se_4$, In_2Se_3 (1 mmol, 0.467g), Se powder (1 mmol, 0.079 g), and 4 mL of hydrazine were added to a 20 mL glass vial and stirred for 48 hours.

K_3AsS_3: A 0.25 M solution was prepared by adding As_2S_3 (0.5 mmol, 0.123 g), K_2S (1.5 mmol, 0.165 g), and 4 mL distilled NMF for 96 hours. Small amounts of residual solids were removed by filtration through a 0.2 μm PVDF membrane.

K_3AsS_4: A 0.5 M solution was prepared by adding As_2S_5 (1.0 mmol, 0.310 g) and K_2S (3.0 mmol, 0.331 g) were stirred in 4 mL distilled NMF for 96 hours. Small amounts of residual solids were removed by filtration through a 0.2 μm PVDF membrane.

$K_4Sn_2S_6$: SnS_2 was prepared from previously reported methods [56]. A 0.25 M solution of $K_4Sn_2S_6$ was prepared by dissolving SnS_2 (2.5 mmol, 0.457 g) and K_2S (2.5 mmol, 0.276 g) in 5 mL of distilled NMF and stirring for 96 hours. Residual solids were first removed by centrifugation then filtration through a 0.44 μm PVDF membrane.

Exchange of Nanocrystal Surface Ligands:

NCs were washed three times after synthesis using standard solvent/non-solvent combinations (e.g. toluene/ethanol). All steps for air sensitive particles including HgTe, Ni, and PbS were performed in a nitrogen glovebox. Au and Pd NCs were initially washed in air, then transferred into a nitrogen glovebox for storage. For metal particles, a pre-exchange thiol treatment

was applied by adding ~10% v/v dodecanethiol to a solution of NCs to replace the native amine ligands. After 5 minutes of stirring, NCs were flocculated with ethanol and redispersed in hexane or toluene for subsequent two-phase ligand exchange. DDT capped metal particles phase transfer into MCC solutions in hydrazine or NMF slowly and are much more resistant to irreversible aggregation during phase transfer compared to NCs capped with the native ligands. PbS, CdSe, and HgTe were exchanged using native ligands.

For two-phase ligand exchange into polar solvents, NCs in either hexane or toluene were added to a bottom phase consisting of a 25 mM MCC ligand in polar solvent. Note that for exchange into NMF, hexane must be used as the non-polar phase as toluene is miscible with NMF. In a typical procedure, 100 mg of DDT capped Au NCs in 12 mL of toluene along with 4 mL of a 25 mM hydrazine solution of $(N_2H_5)_4Sn_2S_6$ were placed in a 20 mL vial with a Teflon coated stirbar. After ~12 hours of stirring, phase transfer completed and the clear non-polar top phase was discarded and washed with fresh toluene two times. The colloidal NCs in the hydrazine phase were then flocculated by addition of 1.5 mL of acetonitrile (ACN), recovered by centrifugation, and redispersed in 4 mL of hydrazine. The ligand concentration was then increased to 25 mM and stirred for an additional 12 hours with 8 mL of fresh toluene. The clear top phase was replaced with fresh toluene an additional two times. The NCs in hydrazine were then precipitated with a minimal amount of ACN three times (adding ~10 mM of MCC ligand during each washing cycle) and stored as a concentrated (~100 mg/mL) solution in hydrazine. Ligand exchange into NMF was performed similarly but precipitation of NCs required the use of ~1:2:1 NMF:ACN:toluene non-solvent mixtures.

Assembly of Inorganically Capped Nanocrystals:

Au and Pd NCs were assembled in hydrazine by flocculation via addition of MCC ligand solution. In a typical procedure, ~1-20 μL of 0.5 M MCC ligand solution was added to a 40 μL aliquot of 100 mg/mL NC stock solution to a set final MCC ligand concentration between 10 and 150 mM. Above a critical concentration, a qualitative change in the appearance of the NC solution was observed within seconds as colloidal stability was lost and particles began to agglomerate into supercrystals. The critical flocculation concentration for a given sample varied with the MCC ligand used due to changes in anion valency (i.e., ionic strength).

Ni NCs with AsS_3^{3-} surface ligands were assembled in NMF by adding an excess of K_3AsS_3 ligands to induce flocculation. Due to the high dielectric constant of NMF, a large excess (>150 mM) of MCC ligand is required to induce assembly which is assisted by the relatively large hard sphere diameter (9 nm) of the NCs with relatively large vdW attractive potentials.

PbS and PbSe NCs with $Sn_2S_6^{4-}$ surface ligands were assembled in NMF by addition of excess K_3AsS_4 ligand solution and ACN. Using additional ligand concentration alone does not lead to SC formation and cannot easily fully flocculate NCs with small (<6 nm) diameters. PbS NC solutions were increased to 200 mM K_3AsS_4 in NMF and within minutes, additional amounts of ACN were added to either partially or fully flocculate the sample. In typical experiments, 20 μL of 0.4 M K_3AsS_4 solution was added to 20 uL of NC stock solution. The addition of >17 μL ACN (>30% v/v) lead to the complete precipitation of NCs into SCs over a period of seconds to minutes. Intermediate volumes of ACN (20-30% v/v) induced a phase separation into dilute fluid, dense fluid, and solid layers visible by eye. Solutions with <20% ACN remained colloidally stable for days in sealed capillaries with no visible aggregation.

CdSe NCs were flocculated in both hydrazine and NMF using an excess of MCC ligand

concentration and ACN. In all cases, no SCs were observed over a wide variety of ligand concentrations, capping ligands, or NMF/ACN solvent mixtures.

UV-VIS-NIR Absorption:

Steady-state optical absorption measurements were collected on a Varian Cary 500 UV-Vis-NIR spectrophotometer.

DLS:

Dynamic light scattering data were collected using a Malvern Instruments Nano-ZS zetasizer.

PXRD:

Wide-angle powder x-ray diffraction (PXRD) data was acquired on a Bruker D8 diffractometer using a 1.541 Å Cu K-α source and a Vantec 2000 array detector.

ICP-OES:

Elemental analysis of nanocrystal samples was carried out by inductively coupled plasma optical emission spectroscopy on an Agilent 700 Series instrument. Nanocrystal samples were digested using trace metal grade nitric acid, hydrochloric acid, and 30% hydrogen peroxide and were diluted using ultrapure deionized water.

TEM:

Transmission electron micrographs were acquired using a Tecnai F30 microscope at 300 kV accelerating voltage. Samples were imaged on 400 mesh copper grids with amorphous carbon support (Ted Pella). Local chemical characterization by electron energy loss spectroscopy (EELS) was conducted using an FEI Titan 3 microscope equipped with a GatanTridiem 863ER detector.

SEM:

Scanning electron micrographs were obtained on a Zeiss Merlin scanning electron microscope with 5 kV accelerating voltage.

SAXS:

Small-angle X-ray scattering data was measured on a SAXSLAB Ganesha instrument with a Cu K alpha source. Colloidal and supercrystal samples in hydrazine were measured either as powders sandwiched between two layers of adhesive backed polyimide film or in glass capillaries sealed first with paraffin wax, removed from the glovebox, then further sealed with epoxy. Note that hydrazine vapors will slowly degrade epoxy upon extended exposure. Samples in NMF were removed from the glovebox and either measured in flame sealed capillaries or sandwiched between polyimide film layers.

In situ SAXS:

In situ SAXS data were collected at the Stanford Synchrotron Radiation Lightsource (SSRL) at beamline 1-5 with a photon energy of 15 keV and beam size of 600x600 μm. In a nitrogen filled glovebox, a solution of 4.6 nm Au with $(N_2H_5)_4Sn_2S_6$ ligands in hydrazine was loaded into a 2 mm path length quartz cuvette with custom 200 μm thick windows. The cuvette was sealed using a rubber septum and parafilm, and a syringe preloaded with a solution of 0.5 M $(N_2H_5)_4Sn_2S_6$ in hydrazine was attached to the cuvette via Teflon tubing through the septum. The gas-tight apparatus was carefully moved into the beam path, and data was collected continuously while stirring the solution. The ionic strength was increased to 125 mM by slow addition of the ligand solution in 5 μL increments via syringe pump over a period of 2 hours.

Preparation of SAXS Samples:

Assemblies of NCs could be measured either in raw solutions or as powders. For solution measurements in hydrazine, NC solutions were transferred to 1.1 mm OD glass capillaries (100 μm thickness) in the glovebox and sealed with melted paraffin wax. The capillaries were then removed from the glovebox and further sealed with epoxy. Note that hydrazine vapors will slowly degrade epoxy if placed in direct contact. Solutions in NMF were transferred outside of the glovebox and flame sealed in glass capillaries. Powdered samples were sandwiched between two layers of polyimide tape. Samples in hydrazine were first washed three times with pure ACN. The resulting clean pellet of SCs can then be ground into a powder by mechanical agitation with a plastic pipette tip and transferred to a polyimide film. Note that hydrazine is incompatible with polyimide-based materials and pure ACN should be used as a transfer agent.

3.10. Chapter 3 bibliography

1. Vanmaekelbergh, D. Self-Assembly of Colloidal Nanocrystals as Route to Novel Classes of Nanostructured Materials. *Nano Today* **2011**, *6* (4), 419–437.
2. Boles, M. A.; Engel, M.; Talapin, D. V. Self-Assembly of Colloidal Nanocrystals: From Intricate Structures to Functional Materials. *Chemical Reviews* **2016**, *116* (18), 11220–11289.
3. Murray, C. B.; Kagan, C. R.; Bawendi, M. G. Synthesis and Characterization of Monodisperse Nanocrystals and Close-Packed Nanocrystal Assemblies. *Annual Review of Materials Science* **2000**, *30* (1), 545–610.
4. Fortini, A.; Sanz, E.; Dijkstra, M. Crystallization and Gelation in Colloidal Systems with Short-Ranged Attractive Interactions. *Physical Review E* **2008**, *78* (4), 41402.
5. Shevchenko, E. V; Talapin, D. V; Kotov, N. A.; O'Brien, S.; Murray, C. B. Structural Diversity in Binary Nanoparticle Superlattices. *Nature* **2006**, *439*, 55.
6. Boles, M. A.; Talapin, D. V. Many-Body Effects in Nanocrystal Superlattices: Departure from Sphere Packing Explains Stability of Binary Phases. *Journal of the American Chemical Society* **2015**, *137* (13), 4494–4502.
7. Paik, T.; Diroll, B. T.; Kagan, C. R.; Murray, C. B. Binary and Ternary Superlattices Self-Assembled from Colloidal Nanodisks and Nanorods. *Journal of the American Chemical Society* **2015**, *137* (20), 6662–6669.
8. Macfarlane, R. J.; Lee, B.; Jones, M. R.; Harris, N.; Schatz, G. C.; Mirkin, C. A. Nanoparticle Superlattice Engineering with DNA. *Science* **2011**, *334* (6053), 204–208.

9. Talapin, D. V; Shevchenko, E. V; Bodnarchuk, M. I.; Ye, X.; Chen, J.; Murray, C. B. Quasicrystalline Order in Self-Assembled Binary Nanoparticle Superlattices. *Nature* **2009**, *461* (7266), 964–967.
10. Ye, X.; Chen, J.; Eric Irrgang, M.; Engel, M.; Dong, A.; Glotzer, S. C.; Murray, C. B. Quasicrystalline Nanocrystal Superlattice with Partial Matching Rules. *Nature Materials* **2017**, *16* (2), 214–219.
11. Mueller, N. S.; Okamura, Y.; Vieira, B. G. M.; Juergensen, S.; Lange, H.; Barros, E. B.; Schulz, F.; Reich, S. Deep Strong Light–Matter Coupling in Plasmonic Nanoparticle Crystals. *Nature* **2020**, *583* (7818), 780–784.
12. Chen, J.; Dong, A.; Cai, J.; Ye, X.; Kang, Y.; Kikkawa, J. M.; Murray, C. B. Collective Dipolar Interactions in Self-Assembled Magnetic Binary Nanocrystal Superlattice Membranes. *Nano Letters* **2010**, *10* (12), 5103–5108.
13. Lee, J.-S.; Kovalenko, M. V; Huang, J.; Chung, D. S.; Talapin, D. V. Band-like Transport, High Electron Mobility and High Photoconductivity in All-Inorganic Nanocrystal Arrays. *Nature Nanotechnology* **2011**, *6*, 348.
14. Lin, M. Y.; Lindsay, H. M.; Weitz, D. A.; Ball, R. C.; Klein, R.; Meakin, P. Universality in Colloid Aggregation. *Nature* **1989**, *339* (6223), 360–362.
15. Carey, G. H.; Chou, K. W.; Yan, B.; Kirmani, A. R.; Amassian, A.; Sargent, E. H. Materials Processing Strategies for Colloidal Quantum Dot Solar Cells: Advances, Present-Day Limitations, and Pathways to Improvement. *MRS Communications* **2013**, *3* (2), 83–90.
16. Boneschanscher, M. P.; Evers, W. H.; Geuchies, J. J.; Altantzis, T.; Goris, B.; Rabouw, F. T.; Van Rossum, S. A. P.; Van Der Zant, H. S. J.; Siebbeles, L. D. A.; Van Tendeloo, G.; Swart, I.; Hilhorst, J.; Petukhov, A. V; Bals, S.; Vanmaekelbergh, D. Long-Range

Orientation and Atomic Attachment of Nanocrystals in 2D Honeycomb Superlattices. *Science* **2014**, *344* (6190), 1377–1380.

17. Abelson, A.; Qian, C.; Salk, T.; Luan, Z.; Fu, K.; Zheng, J. G.; Wardini, J. L.; Law, M. Collective Topo-Epitaxy in the Self-Assembly of a 3D Quantum Dot Superlattice. *Nature Materials* **2020**, *19* (1), 49–55.
18. Whitham, K.; Yang, J.; Savitzky, B. H.; Kourkoutis, L. F.; Wise, F.; Hanrath, T. Charge Transport and Localization in Atomically Coherent Quantum Dot Solids. *Nature Materials* **2016**, *15* (5), 557–563.
19. Balazs, D. M.; Dirin, D. N.; Fang, H.-H.; Protesescu, L.; ten Brink, G. H.; Kooi, B. J.; Kovalenko, M. V; Loi, M. A. Counterion-Mediated Ligand Exchange for PbS Colloidal Quantum Dot Superlattices. *ACS Nano* **2015**, *9* (12), 11951–11959.
20. Weidman, M. C.; Yager, K. G.; Tisdale, W. A. Interparticle Spacing and Structural Ordering in Superlattice PbS Nanocrystal Solids Undergoing Ligand Exchange. *Chemistry of Materials* **2015**, *27* (2), 474–482.
21. Yu, Y.; Yu, D.; Sadigh, B.; Orme, C. A. Space- and Time-Resolved Small Angle X-Ray Scattering to Probe Assembly of Silver Nanocrystal Superlattices. *Nat Commun* **2018**, *9* (1), 4211.
22. Lan, X.; Chen, M.; Hudson, M. H.; Kamysbayev, V.; Wang, Y.; Guyot-Sionnest, P.; Talapin, D. V. Quantum Dot Solids Showing State-Resolved Band-like Transport. *Nat. Mater.* **2020**, *19* (3), 323–329.
23. Choi, H.; Ko, J.-H.; Kim, Y.-H.; Jeong, S. Steric-Hindrance-Driven Shape Transition in PbS Quantum Dots: Understanding Size-Dependent Stability. *J. Am. Chem. Soc.* **2013**, *135* (14), 5278–5281.

24. Lee, S.; Bluemle, M. J.; Bates, F. S. Discovery of a Frank-Kasper σ Phase in Sphere-Forming Block Copolymer Melts. *Science* **2010**, *330* (6002), 349–353.
25. Sanchez-Burgos, I.; Sanz, E.; Vega, C.; Espinosa, J. R. Fcc *vs.* Hcp Competition in Colloidal Hard-Sphere Nucleation: On Their Relative Stability, Interfacial Free Energy and Nucleation Rate. *Phys. Chem. Chem. Phys.* **2021**, *23* (35), 19611–19626.
26. Burstein, E.; Perkowitz, S.; Brodsky, M. H. The Dielectric Properties of the Cubic IV-VI Compund Semiconductors. *J. Phys. Colloques* **1968**, *29* (C4), C4-78-C4-83.
27. Barros, K.; Luijten, E. Dielectric Effects in the Self-Assembly of Binary Colloidal Aggregates. *Phys. Rev. Lett.* **2014**, *113* (1), 017801.
28. Guerrero García, G. I.; Olvera de la Cruz, M. Polarization Effects of Dielectric Nanoparticles in Aqueous Charge-Asymmetric Electrolytes. *J. Phys. Chem. B* **2014**, *118* (29), 8854–8862.
29. Saunders, A. E.; Korgel, B. A. Second Virial Coefficient Measurements of Dilute Gold Nanocrystal Dispersions Using Small-Angle X-Ray Scattering. *The Journal of Physical Chemistry B* **2004**, *108* (43), 16732–16738.
30. Silvera Batista, C. A.; Larson, R. G.; Kotov, N. A. Nonadditivity of Nanoparticle Interactions. *Science* **2015**, *350* (6257), 1242477.
31. Haxton, T. K.; Hedges, L. O.; Whitelam, S. Crystallization and Arrest Mechanisms of Model Colloids. *Soft Matter* **2015**, *11* (48), 9307–9320.
32. Liu, H.; Garde, S.; Kumar, S. Direct Determination of Phase Behavior of Square-Well Fluids. *The Journal of Chemical Physics* **2005**, *123* (17), 174505.
33. Noro, M. G.; Frenkel, D. Extended Corresponding-States Behavior for Particles with Variable Range Attractions. *The Journal of Chemical Physics* **2000**, *113* (8), 2941–2944.

34. Ten Wolde, P. R.; Frenkel, D. Enhancement of Protein Crystal Nucleation by Critical Density Fluctuations. *Science* **1997**, *277* (5334), 1975–1978.

35. Poon, W. C. K.; Renth, F.; Evans, R. M. L.; Fairhurst, D. J.; Cates, M. E.; Pusey, P. N. Colloid-Polymer Mixtures at Triple Coexistence: Kinetic Maps from Free-Energy Landscapes. *Phys. Rev. Lett.* **1999**, *83* (6), 1239–1242.

36. Muschol, M.; Rosenberger, F. Liquid–Liquid Phase Separation in Supersaturated Lysozyme Solutions and Associated Precipitate Formation/Crystallization. *The Journal of Chemical Physics* **1997**, *107* (6), 1953–1962.

37. Gliko, O.; Neumaier, N.; Pan, W.; Haase, I.; Fischer, M.; Bacher, A.; Weinkauf, S.; Vekilov, P. G. A Metastable Prerequisite for the Growth of Lumazine Synthase Crystals. *J. Am. Chem. Soc.* **2005**, *127* (10), 3433–3438.

38. Sauter, A.; Roosen-Runge, F.; Zhang, F.; Lotze, G.; Feoktystov, A.; Jacobs, R. M. J.; Schreiber, F. On the Question of Two-Step Nucleation in Protein Crystallization. *Faraday Discuss.* **2015**, *179*, 41–58.

39. Sengwa, R. J.; Khatri, V.; Sankhla, S. Static Dielectric Constants and Kirkwood Correlation Factor of the Binary Mixtures of N-Methylformamide with Formamide, N,N-Dimethylformamide and N,N-Dimethylacetamide. *J Solution Chem* **2009**, *38* (6), 763–769.

40. Li, T.; Senesi, A. J.; Lee, B. Small Angle X-Ray Scattering for Nanoparticle Research. *Chemical Reviews* **2016**, *116* (18), 11128–11180.

41. Frenkel, D.; Vos, R. J.; de Kruif, C. G.; Vrij, A. Structure Factors of Polydisperse Systems of Hard Spheres: A Comparison of Monte Carlo Simulations and Percus–Yevick Theory. *The Journal of Chemical Physics* **1986**, *84* (8), 4625–4630.

42. Choi, J. J.; Bealing, C. R.; Bian, K.; Hughes, K. J.; Zhang, W.; Smilgies, D.-M.; Hennig, R. G.; Engstrom, J. R.; Hanrath, T. Controlling Nanocrystal Superlattice Symmetry and Shape-Anisotropic Interactions through Variable Ligand Surface Coverage. *J. Am. Chem. Soc.* **2011**, *133* (9), 3131–3138.
43. Boles, M. A.; Talapin, D. V. Binary Assembly of PbS and Au Nanocrystals: Patchy PbS Surface Ligand Coverage Stabilizes the CuAu Superlattice. *ACS Nano* **2019**, *13* (5), 5375–5384.
44. Anderson, N. C.; Hendricks, M. P.; Choi, J. J.; Owen, J. S. Ligand Exchange and the Stoichiometry of Metal Chalcogenide Nanocrystals: Spectroscopic Observation of Facile Metal-Carboxylate Displacement and Binding. *Journal of the American Chemical Society* **2013**, *135* (49), 18536–18548.
45. Weidman, M. C.; Smilgies, D.-M.; Tisdale, W. A. Kinetics of the Self-Assembly of Nanocrystal Superlattices Measured by Real-Time in Situ X-Ray Scattering. *Nature Materials* **2016**, *15* (7), 775–781.
46. Peng, S.; Lee, Y.; Wang, C.; Yin, H.; Dai, S.; Sun, S. A Facile Synthesis of Monodisperse Au Nanoparticles and Their Catalysis of CO Oxidation. *Nano Research* **2008**, *1* (3), 229–234.
47. Wang, P.; Qiao, Q.; Zhu, Y.; Ouyang, M. Colloidal Binary Supracrystals with Tunable Structural Lattices. *Journal of the American Chemical Society* **2018**, *140* (29), 9095–9098.
48. Wu, L.; Willis, J. J.; McKay, I. S.; Diroll, B. T.; Qin, J.; Cargnello, M.; Tassone, C. J. High-Temperature Crystallization of Nanocrystals into Three-Dimensional Superlattices. *Nature* **2017**, *548* (7666), 197–201.

49. Cargnello, M.; Doan-Nguyen, V. V. T.; Gordon, T. R.; Diaz, R. E.; Stach, E. A.; Gorte, R. J.; Fornasiero, P.; Murray, C. B. Control of Metal Nanocrystal Size Reveals Metal-Support Interface Role for Ceria Catalysts. *Science* **2013**, *341* (6147), 771–773.
50. Talapin, D. V; Nelson, J. H.; Shevchenko, E. V; Aloni, S.; Sadtler, B.; Alivisatos, A. P. Seeded Growth of Highly Luminescent CdSe/CdS Nanoheterostructures with Rod and Tetrapod Morphologies. *Nano Letters* **2007**, *7* (10), 2951–2959.
51. Chen, O.; Chen, X.; Yang, Y.; Lynch, J.; Wu, H.; Zhuang, J.; Cao, Y. C. Synthesis of Metal–Selenide Nanocrystals Using Selenium Dioxide as the Selenium Precursor. *Angewandte Chemie International Edition* **2008**, *47* (45), 8638–8641.
52. Zhang, J.; Crisp, R. W.; Gao, J.; Kroupa, D. M.; Beard, M. C.; Luther, J. M. Synthetic Conditions for High-Accuracy Size Control of PbS Quantum Dots. *The Journal of Physical Chemistry Letters* **2015**, *6* (10), 1830–1833.
53. Hendricks, M. P.; Campos, M. P.; Cleveland, G. T.; Jen-La Plante, I.; Owen, J. S. A Tunable Library of Substituted Thiourea Precursors to Metal Sulfide Nanocrystals. *Science* **2015**, *348* (6240), 1226–1230.
54. Quan, Z.; Wu, D.; Zhu, J.; Evers, W. H.; Boncella, J. M.; Siebbeles, L. D. A.; Wang, Z.; Navrotsky, A.; Xu, H. Energy Landscape of Self-Assembled Superlattices of PbSe Nanocrystals. *Proceedings of the National Academy of Sciences* **2014**, *111* (25), 9054–9057.
55. Kovalenko, M. V; Scheele, M.; Talapin, D. V. Colloidal Nanocrystals with Molecular Metal Chalcogenide Surface Ligands. *Science* **2009**, *324* (5933), 1417–1420.
56. Kovalenko, M. V; Bodnarchuk, M. I.; Zaumseil, J.; Lee, J.-S.; Talapin, D. V. Expanding the Chemical Versatility of Colloidal Nanocrystals Capped with Molecular Metal

Chalcogenide Ligands. *Journal of the American Chemical Society* **2010**, *132* (29), 10085–10092.